

**DESIGN AND SYNTHESIS OF GREEN NANOSTRUCTURES AND THEIR  
APPLICATIONS**

by

Milad Torabfam

Submitted to the Graduate School of Engineering and Natural Sciences  
in partial fulfillment of the requirements for the degree of  
Doctor of Philosophy

Sabancı University

July 2023

© Milad Torabfam 2023

All Rights Reserved

# DESIGN AND SYNTHESIS OF GREEN NANOSTRUCTURES AND THEIR APPLICATIONS

Milad Torabfam

Materials Science and Nano Engineering, Doctor of Philosophy, 2023

Thesis Supervisor: Assoc. Prof. Dr. Meral Yüce

Thesis Co-advisor: Assoc. Prof. Dr. Mustafa Kemal Bayazit

Keywords: Green synthesis, Fluidic system, Microwave irradiation, Polymeric nanocomposite, Silver nanoparticle, Copper nanoparticle, Polymer, Algae, Optimization, Antimicrobial activity

## ABSTRACT

Advances in nanoscience have paved the way for new research fields in green chemistry. Nanostructures with various sizes, shapes, and modifications have considerable potential in many sensing, antimicrobial and plasmonic applications due to their superior mechanical and antimicrobial properties. In recent years, effective manufacturing of pure nanocrystals with a narrow size distribution in a matrix has been very challenging. Also, it is highly crucial to get their full potential for advanced applications. This thesis mainly focuses on the design and synthesis of nanostructures and the evaluation of their applications. In this thesis, nanostructures with narrowly distributed nanoparticles having antimicrobial features were synthesized using various synthesis methods. The practical synthesis of silver nanoparticles was achieved through the reduction of silver nitrate solution using an algal source, *Chlorella vulgaris*, as the reducing as well as the stabilizing agent. The energy required for this synthesis was supplied by microwave radiation. The silver nanoparticles with high stability (a zeta potential of  $-17\text{mV}$ ), a hydrodynamic size distribution of 1–50 nm, and a mostly spherical shape were obtained through a 10-min process. Antibacterial features of the produced silver nanoparticles were verified against those of *Salmonella enterica* subsp. *enterica* serovar *typhimurium* and *Staphylococcus aureus*. Also, A long-lasting nanocomposite manufacturing challenge was, for the first time, overcome by our microwave-powered fluidic system. The effect of microwave power, flow rate, and concentration of the reagents were systematically studied. The nylon-6 nanocomposite bearing evenly distributed silver nanoparticles with a mean size of  $\sim 2.59 \pm 0.639$  nm were manufactured continuously in  $\sim 2$  min at  $\sim 50\text{--}55^\circ\text{C}$  using

a green solvent, formic acid. Given the small-sized silver nanoparticles in the microwave fluidic-manufactured nanocomposites, the antibacterial activity tests with *Escherichia coli*, *Staphylococcus aureus*, and *Pseudomonas aeruginosa* show superior activity compared to that of the large silver nanoparticle-bearing (~50 nm) nanocomposites produced in a fluidic system which has convectional heating. Furthermore, a microwave-promoted flow system was successfully employed for in-situ, continuous manufacturing of polyamide 11 and cellulose acetate nanocomposites having copper/copper oxide nanoparticles with a mean diameter of less than 10 nm and narrow size distribution. No copper/copper oxide nanoparticle formation occurred under almost identical experimental conditions in the microwave-batch system. The experimental parameters, including microwave power, polymer concentration, metal salt concentration, and flow rate, were fully optimized, and reproducibility was tested. These experiments proved that the above-mentioned green nanostructures which have been synthesized using environmentally friendly, time-saving, and scalable techniques have the potential to exhibit high efficiency for antimicrobial applications.

# YEŞİL NANO YAPILARIN TASARIMI VE SENTEZİ VE UYGULAMALARI

Milad Torabfam

Malzeme Bilimi ve Nano Mühendislik, Doktora Tezi, 2023

Tez Danışmanı: Doç. Dr. Meral Yüce

Tez Eş Danışmanı: Doç. Dr. Mustafa Kemal Bayazit

Anahtar kelimeler: Yeşil sentez, Akışkan sistem, Mikrodalga ışınlama, Polimerik nanokompozit, Gümüş nanoparçacık, Bakır nanoparçacık, Polimer, Algler, Optimizasyon, Antimikrobiyal aktivite

## ÖZET

Nanobilimdeki gelişmeler yeşil kimyada yeni araştırma alanlarının yolunu açmıştır. Çeşitli boyut, şekil ve modifikasyonlara sahip nanoyapılar, üstün mekanik ve antimikrobiyal özelliklerinden dolayı birçok algılama, antimikrobiyal ve plazmonik uygulamada önemli bir potansiyele sahiptir. Son yıllarda, bir matris içinde dar bir boyut dağılımına sahip saf nanokristallerin etkin üretimi çok zor olmuştur. Ayrıca, gelişmiş uygulamalar için tam potansiyellerini elde etmek son derece önemlidir. Bu tez esas olarak nanoyapıların tasarımı ve sentezi ile uygulamalarının değerlendirilmesine odaklanmaktadır. Bu tez çalışmasında, çeşitli sentez yöntemleri kullanılarak antimikrobiyal özelliklere sahip dar dağılımlı nanopartiküllere sahip nanoyapılar sentezlendi. Gümüş nanopartiküllerin pratik sentezi, hem indirgeyici hem de stabilize edici madde olarak bir alg kaynağı olan *Chlorella vulgaris* kullanılarak gümüş nitrat çözeltisinin indirgenmesi yoluyla elde edildi. Bu sentez için gereken enerji mikrodalga radyasyonu ile sağlandı. Yüksek kararlılığa (-17mV'lik bir zeta potansiyeli), 1-50 nm'lik hidrodinamik boyut dağılımına ve yoğunlukla küresel şekle sahip gümüş nanopartiküller, 10 dakikalık bir işlemle elde edildi. Üretilen gümüş nanopartiküllerin antibakteriyel özellikleri, *Salmonella enterica subsp. enterica serovar typhimurium* ve *Staphylococcus aureus'a* karşı

doğrulandı. Ayrıca, uzun süredir devam eden bir nanokompozit üretim zorluğunun üstesinden ilk kez mikrodalga gücüyle çalışan akışkan sistemimiz geldi. Reaktiflerin konsantrasyonunun etkisi, mikrodalga gücü, ve akış hızı sistematik olarak incelenmiştir. Ortalama boyutu  $\sim 2,59 \pm 0,639$  nm olan eşit dağılmış gümüş nanoparçacıkları taşıyan naylon-6 nanokompozit, yeşil bir solvent olan formik asit kullanılarak  $\sim 50\text{--}55$  °C'de ~2 dakika içinde sürekli olarak üretildi. MWF tarafından üretilen nanokompozit'lerdeki küçük boyutlu gümüş nanopartiküller göz önüne alındığında, *Escherichia coli*, *Staphylococcus aureus* ve *Pseudomonas aeruginosa* ile yapılan antibakteriyel aktivite testleri, konveksiyonel ısıtmaya sahip olan akışkan bir sistemde üretilen büyük gümüş nanopartikül taşıyan ( $\sim 50$  nm) nanokompozit'lerinkine kıyasla üstün aktivite gösterir. Ayrıca, mikrodalga destekli bir akış sistemi, ortalama çapı 10 nm'den küçük ve dar boyut dağılımına sahip bakır nanoparçacıklara sahip poliamid 11 ve selüloz asetat nanokompozit'lerin sürekli üretimi için başarıyla kullanıldı. Mikrodalga destekli batch sisteminde hemen hemen aynı deneysel koşullar altında hiçbir gümüş nanoparçacık oluşumu meydana gelmedi. Mikrodalga gücü, polimer konsantrasyonu, metal tuzu konsantrasyonu ve akış hızı gibi deneysel parametreler tamamen optimize edildi ve tekrar üretilebilirlik test edildi.

## **ACKNOWLEDGEMENTS**

I would like to express my sincere gratitude to my advisor Assoc. Prof. Dr. Meral Yüce for her unwavering support in all the time of my Ph.D. She was always there whenever I encountered a problem and guided me with a wide variety of solutions.

I extend my sincere thanks to my co-advisor, Assoc. Prof. Dr. Mustafa Kemal Bayazit for his endless guidance in my research. I would not go that further without his invaluable insight into nanotechnology and polymer science.

I would like to thank my committee members, Assoc. Prof. Dr. Ali Zarrabi, Assoc. Prof. Dr. Hasan Kurt, Asst. Prof. Dr. Yilmaz Şimşek, and Asst. Prof. Dr. Mehmet Kocatürk for their precious time, guidance, and insightful feedback.

I must thank the faculty members of the Department of Materials Science and Nanoengineering for their valuable and educative lectures throughout my Ph.D. which help me shape my profession in materials science. I thank Prof. Dr. Mehmet Ali Gülgün, Prof. Dr. İbrahim Burç Mısırlıoğlu, and Daniel Lee Calvey for their guidance.

I would like to acknowledge TÜBİTAK (Scientific and Technological Research Institution of Turkey) for providing financial support for this study under the 2232 International Fellowship for Outstanding Researchers Program of (Project: 118C316). The funder had no role in the study design, data collection, analysis, the decision to publish, or the preparation of this thesis

I'm deeply indebted to my friends Can Egil, Dr. Adnan Tasdemir, and Sina Khalilvandi Behrouzyar for providing the unlimited support and friendship that I required. I learned so many helpful things from them. I know that when we are old, they will still be there as supportive and caring friends.

I feel very lucky to know my lab mates Tuçe Fidan, Beyzanur Günaydin, Dr. Refik Arat, Dr. Oğuz Bayindir, Qandeel Saleem, Eda Çapkin, Begüm Balkan, and Semih Pehlivan for being the best teammates.

I must deliver my regards to our lab specialists Ali Osman Çetinkaya, Serkan Bostan, Nursel Karakaya, Bülent Köroğlu, Selim Tanrısever, and Onur Serbest for their technical support and constructive feedback.

I will always remember the time I spent with my best flatmates Seyedpayam Seyedkazemi, Ali Hosseinpour Shafaghi, and Sivakumar Malliappan in the dorm.

Thanks to all my friends in MAT grads and undergrads.

I would like to express my most special thanks to my wife Gizem Çelebi Torabfam. Without her great understanding, heartening, and also delicious cooking in the past years, it would be impossible for me to complete my Ph.D. I am so lucky to have her in my life.

Last but not least, I would like to thank my mother Lili Sahandi, my father Javad Torabfam, and my aunt Lida Sahandi for their unconditional support. None of this could have happened without their trust and love. I am so thankful to have a wonderful family like them.

I feel very lucky to have my dog Teddy as emotional support in my life. Without Teddy, life wouldn't be so bearable and enjoyable.

## TABLE OF CONTENTS

ABSTRACT .....	ii
ÖZET .....	iv
ACKNOWLEDGEMENTS .....	vi
TABLE OF CONTENTS.....	viii
LIST OF FIGURES .....	x
LIST OF TABLES .....	xiii
LIST OF SYMBOLS AND ABBREVIATIONS .....	xiv
Chapter 1: INTRODUCTION .....	1
1.1    The Motivations of This Thesis .....	1
1.2    Algae - Derived Silver Nanoparticles .....	1
1.3    Polyamide Nanocomposites with Evenly Distributed Silver Nanoparticles .....	2
1.4    Copper/Copper Oxide - (Polyamide/Cellulose acetate) Nanocomposites .....	2
Chapter 2: MICROWAVE - ASSISTED GREEN SYNTHESIS OF SILVER NANOPARTICLES USING DRIED EXTRACTS OF <i>CHLORELLA VULGARIS</i> AND ANTIBACTERIAL ACTIVITY STUDIES .....	4
2.1    Introduction .....	4
2.2    Materials and Methods .....	12
2.2.1    Materials .....	12
2.2.2    Methods.....	12
2.3    Results and Discussion.....	15
2.3.1    Characterization of NP formation.....	15
2.3.2    Antibacterial activity of the AgNPs .....	20
2.4    Conclusion.....	21

Chapter 3: A MICROWAVE-POWERED CONTINUOUS FLUIDIC SYSTEM FOR POLYMERIC NANOCOMPOSITE MANUFACTURING: A PROOF-OF-CONCEPT STUDY.....	23
3.1    Introduction .....	23
3.2    Materials And Methods .....	24
3.2.1    Materials .....	24
3.2.2    Methods.....	24
3.3    Results and Discussion.....	28
3.3.1    Experimental Procedure.....	28
3.3.2    Effect of MWP and FR ratio .....	32
3.3.3    Effect of Reagent (PA6, AgNO <sub>3</sub> , and NaBH <sub>4</sub> ) Concentration and FR Ratio.....	42
3.3.4    The microwave-fluidic (MWF) system versus the conventional heating-fluidic (CHF) system.....	44
3.4    Conclusion.....	51
Chapter 4: MICROWAVE-PROMOTED CONTINUOUS FLOW SYNTHESIS OF NYLON11 / CELLULOSE ACETATE-COPPER-BASED NANOCOMPOSITES .....	53
4.1    Introduction .....	53
4.2    Materials and Methods .....	54
4.2.1    Materials .....	54
4.2.2    Methods.....	54
4.3    Results and Discussion.....	58
4.3.1    Preparation of the Cu-O <sub>x</sub> NP/PA11 NC.....	58
4.3.2    Preparation of the Cu-O <sub>x</sub> NP/CA NC .....	65
4.4    Conclusion.....	74
Chapter 5: CONCLUSION.....	76
REFERENCES .....	78

## LIST OF FIGURES

Figure 2-1: This figure represents the main methods of NP synthesis as well as subdivisions of green synthesis along with a schematic demonstration of the current AgNP formation.....	12
Figure 2-2: Various stages of AgNP formation after 2 (A), 4 (B), 6 (C), 8 (D), and 10 (E) min of MW radiation.....	15
Figure 2-3: Recorded UV-Vis spectra of the provided AgNPs according to the MW exposure time. ....	16
Figure 2-4: FT-IR spectra of <i>Chlorella vulgaris</i> and prepared AgNPs.....	16
Figure 2-5: The hydrodynamic size distribution of the synthesized AgNPs after 2, 4, 6, 8, and 10 min of being exposed to MW radiation. ....	18
Figure 2-6: Zeta potential of the synthesized AgNPs after two, four, six, eight, and ten-minute exposure to MW radiation. ....	19
Figure 2-7: SEM images related to the produced AgNPs in various scale bars. ....	20
Figure 2-8: TEM images related to the produced AgNPs.....	20
Figure 2-9: Growth of <i>S. aureus</i> (A) and <i>S. typhimurium</i> (B) on NA plates containing 0 (1) 30 (2), 60 (3), 100 (4), and 300 (5) $\mu$ L of AgNP solution. ....	21
Figure 3-1: Graphical illustration of method applied on PA6 and NC coated glasses for evaluation of their antibacterial efficiency. ....	26
Figure 3-2: Graphical illustration of the MWFS for the continuous preparation of AgNP/PA6 NCs. ....	28
Figure 3-3: The MW power-dependent heating profile of the reaction fluid (PA6, AgNO <sub>3</sub> , and NaBH <sub>4</sub> solution in FA) in the MWFS under 20 psi constant pressure at the MWP of 10, 20, 30, 40, and 50 W. The temperature of the mixture was measured for 5 minutes at time intervals of 30 seconds.....	31
Figure 3-4: Color of the prepared AgNP/PA6 NC <sub>MWFS</sub> using MWPs of a) 10W, b) 20W, c) 30W, and d) 40W.....	32
Figure 3-5: UV-Vis spectra of NCs prepared at MWPs of 10, 20, 30, and 40 W using the FR ratios (NaBH <sub>4</sub> :PA6/AgNO <sub>3</sub> ) of a) 3:1, b) 3:0.5, c) 3:0.25, and d) 3:0.1. The insets of the figures show the FWHM versus MWP graphs. ....	33
Figure 3-6: UV-vis spectra of NC <sub>MWF1-16</sub> . ....	34
Figure 3-7: UV-vis spectra of NC <sub>MWF17-32</sub> . ....	35
Figure 3-8: UV-vis spectra of NC <sub>MWF33-48</sub> . ....	35

Figure 3-9: UV-vis spectra of NC <sub>MWF49-64</sub> .....	36
Figure 3-10: Hydrodynamic size distribution of the prepared NCs. a) NC <sub>MWF52</sub> , b) NC <sub>MWF56</sub> , c) NC <sub>MWF60</sub> , d) NC <sub>MWF64</sub> , and NC <sub>CHF2</sub> .....	37
Figure 3-11: Hydrodynamic size distribution of NC <sub>MWF1-16</sub> .....	38
Figure 3-12: Hydrodynamic size distribution of NC <sub>MWF17</sub> 32 .....	38
Figure 3-13: Hydrodynamic size distribution of NC <sub>MWF33-45</sub> and NC <sub>MWF48</sub> .....	39
Figure 3-14: Hydrodynamic size distribution of NC <sub>MWF49-64</sub> .....	40
Figure 3-15: a) UV-vis spectrum and b) hydrodynamic size distribution of AgNP/PA6 NC prepared using a 5-fold excess of PA6 under the same experimental conditions of NC <sub>MWF64</sub> ..	41
Figure 3-16: Reagent (PA6, AgNO <sub>3</sub> , and NaBH <sub>4</sub> ) concentration-dependent change in the $\lambda_{\max}$ values of the prepared NCs at 40 W and varying FR ratios (3:1, 3:0.5, 3:0.25, and 3:0.1) The arrow shows the change in the particle size .....	42
Figure 3-17: a) TEM image of the AgNPs in NC <sub>MWF64</sub> . Inset shows the mean particle size distribution of the AgNPs. b) The enlarged TEM image of the AgNPs. c) HRTEM image of the spherical AgNPs in NC <sub>MWF64</sub> . Two parallel red lines show the lattice fringes of AgNPs. Inset shows the expanded image of AgNP having [220] lattice plane.....	43
Figure 3-18: a) TEM image of the prepared NC <sub>MWF32</sub> . a) HRTEM image of AgNPs embedded in the matrix of PA6. Red parallel lines exhibit the lattice fringe of AgNPs. The measured distance of 0.22 nm corresponds to [111] lattice plane c) The particle size distribution related to produced AgNPs .....	43
Figure 3-19: UV-Vis spectra of the prepared NCs using the NaBH <sub>4</sub> :PA6/AgNO <sub>3</sub> FR ratios of 3:1 in the CHFS at 50 °C (NC <sub>CHF1</sub> ) and 55 °C (NC <sub>CHF2</sub> ). ....	44
Figure 3-20: TEM image of the AgNPs in NC <sub>CHF2</sub> .....	44
Figure 3-21: a) XRD patterns and b) FTIR spectra of the as-received PA6, NC <sub>MWF60</sub> , NC <sub>MWF64</sub> , and NC <sub>CHF2</sub> .....	46
Figure 3-22: Colony forming units (CFU) of <i>Escherichia coli</i> , <i>Staphylococcus aureus</i> , and <i>Pseudomonas aeruginosa</i> after being exposed to the uncoated glass and the films of the PA6, NC <sub>CHF2</sub> , and NC <sub>MWF64</sub> .....	48
Figure 3-23: SEM images (a and c) and EXD mapping (b and d) of the NC <sub>MWF64</sub> and NC <sub>CHF2</sub> films, respectively.....	49

Figure 3-24: SEM images (a and c) and EDX mapping analysis (b and d) of the prepared NC <sub>MWF64</sub> and NC <sub>CHF2</sub> films, respectively. The spot analysis was performed using ImageJ software. The threshold used was 6-255 for both images.....	50
Figure 4-1: Graphical illustration of the MWFS for the continuous synthesis of Cu-O <sub>x</sub> NPs in the polymer matrix.....	58
Figure 4-2: UV-Vis spectra of samples produced using a) MW-batch and, b) MW-continuous system .....	59
Figure 4-3: a) Color change and b) UV-Vis spectra of samples produced using MW-batch system.....	60
Figure 4-4: a) Color change and b) UV-Vis spectra of samples produced using MW-batch system .....	63
Figure 4-5: a) UV-Vis spectra of NC <sub>7</sub> after being left at RT and b) its color change .....	63
Figure 4-6: a) color of copper (II) sulfate pentahydrate in DMF, b) color change of synthesized CuNP, and c) it's UV-Vis spectrum .....	64
Figure 4-7: Images of (a),(b) blockage, happened, (c) precipitation formed.....	65
Figure 4-8: Color change of a) sample 7, b) sample 8, c) sample 9, and also d) their UV-Vis spectra.....	66
Figure 4-9: Color change of a) sample 10, b) sample 11, and d) their UV-Vis spectra.....	67
Figure 4-10 : Color change of a) NC <sub>11</sub> , b) NC <sub>12</sub> , and d) their UV-Vis spectra.....	68
Figure 4-11 : Color change of a) NC <sub>13</sub> , b) NC <sub>14</sub> , and d) their UV-Vis spectra.....	69
Figure 4-12: a) UV-Vis spectra, and b) color of NC <sub>15</sub> .....	70
Figure 4-13: Color change of a) NC <sub>16</sub> , b) NC <sub>17</sub> , c) NC <sub>18</sub> , d) their UV-Vis spectra, and e) DLS results .....	71
Figure 4-14: XRD patterns of the as-received CA, and NC <sub>17</sub> .....	72
Figure 4-15: FTIR spectrum of CA film and NC <sub>17</sub> film.....	73

## **LIST OF TABLES**

Table 2-1: Green synthesis of AgNPs using plants and microorganisms.....	4
Table 3-1: The list of NCs produced (66 samples) at various experimental conditions (e.g. reagent concentration, MWP, and FR ratio) and their UV-vis $\lambda_{\text{max}}$ and $I_{\text{abs}}$ values .....	29
Table 3-2: The estimated fluid temperatures outside the MW heating zone .....	30
Table 3-3: Antibacterial rate of PA6, NC <sub>CHF2</sub> , and NC <sub>MWF64</sub> films against <i>Escherichia coli</i> , <i>Pseudomonas aeruginosa</i> , and <i>Staphylococcus aureus</i> .....	47
Table 4-1: FRs and MW were examined for the possible synthesis of Cu-based NPs.....	59
Table 4-2: The volume of DMF and time of MW exposure for the possible synthesis of Cu-O <sub>x</sub> /PA11 NC .....	60
Table 4-3: Input concentrations, time, and temperature were examined for the possible synthesis of Cu-O <sub>x</sub> NC .....	61
Table 4-4: The solubility (mg/ml) of CAs in various solvents.....	65

## LIST OF SYMBOLS AND ABBREVIATIONS

CHF	Conventional heating-fluidic
CHFS	Conventional heating fluidic system
DMF	<i>N,N</i> -dimethylformamide
DMSO	Dimethyl sulfoxide
EDS	Energy-dispersive
EDX	Energy dispersive X-ray analysis
FR	Flow rate
FA	Formic acid
FTIR	Fourier transform infrared spectroscopy
FWHM	Full width at half maximum
HRTEM	High-resolution transmission electron microscopy
ICP-OES	Inductively coupled plasma optical emission spectroscopy
MW	Microwave
MWF	Microwave-fluidic
MI	Microwave irradiation
MWP	Microwave power
MWFS	Microwave-powered fluidic system
NC	Nanocomposite
PTFE	Poly(tetrafluoroethylene)
PBS	Phosphate-buffered saline
PA	Polyamide

PA6	Polyamide 6
PA11	Polyamide 11
RA	Reducing agent
RT	Room temperature
SEM	Scanning Electron Microscopy
Au	Gold
Ag	Silver
AgNP	Silver nanoparticle
$\text{AgNO}_3$	Silver nitrate
$\text{NaBH}_4$	Sodium borohydride
TEM	Transmission electron microscopy
UV-vis	Ultraviolet-visible absorption spectroscopy
XRD	X-ray diffraction
PDI	Polydispersity index
Cu	Copper
CuNPs	Copper nanoparticles
$\text{Cu-O}_x\text{NP}$	Copper/copper oxide nanoparticle
$\text{Cu-O}_x$	Copper/copper oxide
MNP	Metal nanoparticle
CA_Butyrate	Cellulose acetate butyrate
CA_Pr	Cellulose acetate propionate
CA	Cellulose acetate
NS	Nanostructure

NM	Nanomaterial
CFU	Colony forming units
$I_{abs}$	Absorbance intensity
$\lambda_{max}$	wavelength maxima

# **Chapter 1: INTRODUCTION**

## **1.1 The Motivations of This Thesis**

The main aim of this dissertation is to design and develop eco-friendly, time-saving, energy-effective, and potentially scalable techniques to manufacture NMs with controllable particle size, distribution, and morphology in a matrix. Based on this motivation, I performed a MW-assisted facile and green synthesis of AgNPs along with an evaluation of their characteristics such as antibacterial features. For this purpose, I synthesized AgNPs derived from *Chlorella vulgaris* and performed several characterizations (Chapter 2). Furthermore, I have been running a project on MW-powered continuous fluidic manufacturing of PA NCs with evenly distributed AgNPs. The long-lasting scientific challenge of continuously preparing a polymeric matrix NC containing 5 nm NPs with a narrow particle size distribution has been overcome by our MW-powered continuous fluidic manufacturing system. I used analyses and methods for the characterization and evaluation of produced NCs (Chapter 3). In addition, I achieved an *in-situ*, and continuous synthesis of Cu/CA-PA11 NCs using MWFS. The main goals of this chapter were to produce a polymeric NC including homogeneously distributed Cu-O<sub>x</sub>NPs in PA11 and CA matrix at low temperatures and residence time. The effect of important parameters on the final product has also been thoroughly studied and optimized (Chapter 4).

## **1.2 Algae - Derived Silver Nanoparticles**

Nanoscience stands out among the futuristic fields of research. Within this field, the synthesis of workable MNPs using biological procedures has attracted significant attention worldwide <sup>1,2</sup>. MNPs present striking physicochemical features when compared to individual molecules and macro metals as a result of high surface area to volume ratios <sup>3</sup>. In the case of AgNPs, based on their sizes and shapes, their fundamental properties such as electrical and thermal conductivity, catalytic activity, solubility, and sensitivity enable widespread employment of them in food packaging, water treatment tasks, and drug delivery applications <sup>4-6</sup>. With a history of approximately 3.4 billion years, microalgae possess a distinct characteristic of high biodiversity. Among various microalgae, eukaryotic green microalgae *Chlorella vulgaris* from the genus *Chlorella* has been present on earth since the Precambrian era <sup>7</sup>. *Chlorella vulgaris* is a ball-shaped atomic type of cell with a diameter ranging from 2 to 10  $\mu\text{m}$  and contains numerous constituents, including cell wall and cytoplasm with mitochondrion and chloroplast organelles. The primary components of *Chlorella vulgaris* are proteins, lipids, carbohydrates,

pigments, minerals, and vitamins. Proteins are incredibly significant in the algal structure and constitute half of the dry weight of the fully grown *Chlorella vulgaris* cell. Besides proteins, lipids are made up of various ingredients, such as glycolipids and hydrocarbons. Carbohydrates such as starch and cellulose are examples of polysaccharides that existed in *Chlorella vulgaris*<sup>7,8</sup>. Also, polysaccharides extracted from algae have a dual impact due to their ability to reduce Ag ions and stabilize the formed AgNPs<sup>9</sup>.

### **1.3 Polyamide Nanocomposites with Evenly Distributed Silver Nanoparticles**

Over the last few decades, metal/metal oxide NPs benefiting from high surface-to-volume ratios have become a center of attention owing to their superior physicochemical and biological properties. Thus, significant effort has been devoted to synthesizing these NSs with narrow size distribution and stabilization<sup>10–15</sup>. Polymers, particularly bearing functional groups, can act as stabilizers while preparing NP/polymer NCs<sup>16</sup>. However, the immobilization of pre-synthesized NPs in a polymer matrix while using traditional mechanical mixing usually results in poor dispersibility or agglomeration<sup>17–19</sup>. In situ batch approaches have improved the dispersion quality and distribution of the NPs in polymer matrices<sup>16,17,20</sup>. In these approaches, specialized polymers and NPs are preferred for the target applications. For example, the biocidal features of Ag make it a great candidate for antimicrobial activities, and it is used as an additive in industries such as wood preservation and antibacterial textiles due to its higher stability in industrial conditions in comparison with other antimicrobial agents<sup>21</sup>. PA6/Ag NC can be prepared by processing silver acetate with the PA6 pellets. The produced NCs show enhanced antimicrobial efficacy compared to the NC prepared using commercially available Ag powder, signifying the importance of the high surface-to-bulk ratio of the AgNPs<sup>22</sup>.

### **1.4 Copper/Copper Oxide - (Polyamide/Cellulose acetate) Nanocomposites**

Polymeric NCs in nanoscience are extremely significant and useful thanks to their extensive applications in various fields, such as medical devices<sup>23</sup>, and coatings<sup>24,25</sup>. Polymers stand out among the stabilizing agents for the synthesis of NPs, since they can supply long stability for NPs and thus can be utilized for even distribution of NPs<sup>26</sup>. There are lots of investigations proving the advantages of polymeric NCs such as design flexibility, and biocompatibility in comparison with polymers<sup>27–31</sup>. Since the physicochemical features of polymeric NCs depend on their size, shape, and surface morphology of NPs, these NSs can exhibit unique antimicrobial, optical, and mechanical characteristics. The in-situ polymerization of a monomer with the simultaneous synthesis of MNPs and the in-situ reduction of metal precursors in the dissolved polymer are two

techniques utilized for the formation of polymeric NCs with distributed MNPs<sup>32,33</sup>. Among biopolymers, nylon 11 is a bioplastic that is provided by the polymerization of 11-aminoundecanoic acid. Although it is applicable in many areas including coating and textile<sup>34</sup>, some disadvantages such as low solubility in organic solvents cannot be neglected. Thus, CA which constitutes a remarkable group of natural polymers can be a suitable alternative to PA11. The reaction between cellulose pulp and acetic anhydride results in CA polymer. This polymer has some excellent features such as biodegradability, low cost, and non-toxicity. However, their poor mechanical features lead to the reduced service life of this polymer. To overcome this, CA is well-complemented by Copper-based NPs<sup>32,35,36</sup>. Considering the antibacterial efficiency of Cu, it shows considerably higher efficiency in NP form in comparison with the bulk form thanks to the greatly higher surface-area-to-volume ratio. The Cu<sup>+</sup> ions released from the surface of NPs penetrate the bacteria and destroy them by hindering their capability of growing<sup>37</sup>. These assays deduced that produced NSs have the potential to exhibit excellent antimicrobial characteristics and can be preferred in various applications.

## **Chapter 2: MICROWAVE - ASSISTED GREEN SYNTHESIS OF SILVER NANOPARTICLES USING DRIED EXTRACTS OF *CHLORELLA VULGARIS* AND ANTIBACTERIAL ACTIVITY STUDIES**

### **2.1 Introduction**

Green synthesis of MNPs is acquiring considerable significance due to their environmental and economic superiorities over other methods. A variety of methods ranging from sono-electrochemical methods and chemical reduction to ultraviolet (UV) irradiation can be implemented for the synthesis of AgNPs<sup>38-40</sup>. The fact that applying some of these synthesis methods results in purified AgNPs cannot be neglected. In contrast, however, the synthesis cost must be considered a fundamental factor in a formation procedure. Furthermore, using hazardous chemical materials as agents during synthesis raises serious questions about environmental toxicity and safety issues in the fabrication process. Consequently, the request has been rising for green methods which are more secure, practical, and environmentally friendly than current physical and chemical methods<sup>41</sup>. The plants along with products of plants and microorganisms (e.g., algae, yeast, fungi, and bacteria) have been used as natural alternatives to other chemicals during synthesis leading to the formation of MNPs. Compared with other conventional methods, NPs formed by biosynthesis contain non-toxic by-products that improve NP biocompatibility in various applications<sup>42</sup>. Being nature-friendly<sup>2</sup>, affordable<sup>43</sup>, maintainable<sup>44</sup>, and free from chemical pollution<sup>45</sup>, biological agents have become excellent candidates for the production of NPs. Furthermore, the green synthesis of NPs using microorganisms has become the center of attention over the past few years due to remarkable properties, such as lower synthesis time<sup>46</sup>, and it is a low-priced, safe, reliable<sup>47</sup>, and single-step<sup>45</sup> procedure. Due to the capping feature of components in microorganisms, the addition of extra stabilizers is not required<sup>42</sup>.

It is also known that MNPs, as an alternative to antibiotics, exhibit outstanding antibacterial properties<sup>46</sup>. Besides this, their antifungal activity is considerable<sup>48</sup>. Among several noble MNPs, AgNPs have been reported to have the most impressive antimicrobial features against various kinds of microorganisms, as summarized in **Table 2-1**.

**Table 2-1:** Green synthesis of AgNPs using plants and microorganisms.

<b>Reducing or stabilizing agent</b>	<b>Size (nm)</b>	<b>Antimicrobial activity</b>	<b>Ref</b>
Turmeric powder	18±0.5	<i>Escherichia coli</i> , <i>Listeria monocytogenes</i>	<sup>49</sup>
<i>Thymbra spicata</i>	7	NA	<sup>50</sup>
<i>Calliandra haematocephala</i> leaf	70	<i>Escherichia coli</i>	<sup>51</sup>
<i>Gracilaria birdiae</i>	20.2-94.9	<i>Escherichia coli</i> , <i>Staphylococcus aureus</i>	<sup>52</sup>
<i>Crocus sativus</i> L.	12–20	<i>Escherichia coli</i> , <i>Pseudomonas aeruginosa</i> , <i>Klebsiella pneumonia</i> , <i>Shigella flexneri</i> , <i>Bacillus subtilis</i>	<sup>53</sup>
<i>Rheum palmatum</i> root	121±2	<i>Staphylococcus aureus</i> , <i>Pseudomonas aeruginosa</i>	<sup>54</sup>
<i>Alysicarpus monilifer</i> leaf	15±2	MRSA and CoNS	<sup>55</sup>
<i>elephantopus scaber</i>	37.86	<i>Bacillus subtilis</i> , <i>Lactococcus lactis</i> , <i>Pseudomonas fluorescens</i> , <i>Pseudomonas aeruginosa</i> , <i>Aspergillus flavus</i> , <i>Aspergillus penicillioides</i>	<sup>56</sup>
<i>Eriobotrya japonica</i>	20	<i>Escherichia coli</i> , <i>Staphylococcus aureus</i>	<sup>57</sup>
<i>Cladosporium Cladosporioides</i>	<100	<i>Escherichia coli</i> ,	<sup>1</sup>

(Fungi)		<i>Staphylococcus aureus,</i> <i>Bacillus subtilis,</i> <i>Staphylococcus epidermidis,</i> <i>Candida albicans</i>	
<i>Botryosphaeria rhodian</i> (Fungi)	2-50	NA	58
<i>Ganoderma sessiliforme</i> (Fungi)	45.26	<i>Escherichia coli,</i> <i>Bacillus subtilis,</i> <i>Streptococcus faecalis,</i> <i>Listeria innocua,</i> <i>Micrococcus luteus</i>	47
<i>Padina pavonica</i> (Algae)	49.6-86.4	NA	41
<i>Bacillus amyloliquefaciens,</i> <i>Bacillus subtilis</i> (Bacteria)	<100	<i>Staphylococcus aureus,</i> <i>Escherichia coli,</i> <i>Pseudomonas aeruginosa,</i> <i>Streptococcus pyogenes,</i> <i>Candida albicans</i>	59
<i>Gelidium amansii</i> (Algae)	27-54	<i>Staphylococcus aureus,</i> <i>Bacillus pumilus,</i> <i>Escherichia coli,</i> <i>Pseudomonas aeruginosa,</i> <i>Vibrio parahaemolyticus,</i> <i>Aeromonas hydrophila</i>	2

<i>Bacillus brevis</i> (Bacteria)	41-68	<i>Salmonella typhi,</i> <i>Staphylococcus aureus</i>	60
<i>Laminaria japonica</i> (Algae)	20-31	NA	45
<i>Streptomyces</i> species (Bacteria)	8.4	<i>Bacillus subtilis,</i> <i>Staphylococcus aureus,</i> <i>Klebsiella pneumoniae,</i> <i>Pseudomonas aeruginosa,</i> <i>Escherichia coli,</i> <i>Proteus mirabilis,</i> <i>Salmonella infantis</i>	61
<i>Rhizopus stolonifera</i> (Fungi)	9.46±2.64	NA	62
<i>Enteromorpha compressa</i> (Algae)	4-24	<i>Escherichia coli,</i> <i>Klebsiella pneumoniae,</i> <i>Pseudomonas aeruginosa,</i> <i>Staphylococcus aureus,</i> <i>Salmonella paratyphoid,</i> <i>Aspergillus niger,</i> <i>Aspergillus flavus,</i> <i>Aspergillus ochraceus,</i> <i>Fusarium moniliforme,</i> <i>Aspergillus terreus</i>	6
<i>Duddingtonia flagrans</i>	11-38	NA	44

(Fungi)			
<i>Pleurotus ostreatus</i> (Fungi)	<40	<i>Bacillus subtilis,</i> <i>Bacillus cereus,</i> <i>Staphylococcus aureus,</i> <i>Escherichia coli,</i> <i>Pseudomonas aeruginosa</i>	<sup>43</sup>
<i>Bacillus methylotrophicus</i> (Bacteria)	10-30	<i>Candida albicans,</i> <i>Salmonella enterica,</i> <i>Escherichia coli,</i> <i>Vibrio parahaemolyticus,</i> <i>Candida albicans,</i>	<sup>63</sup>
<i>Pseudomonas deceptionensis</i> (Bacteria)	10-30	<i>Staphylococcus aureus,</i> <i>Salmonella enterica,</i> <i>Vibrio parahaemolyticus,</i> <i>Candida albicans,</i> <i>Bacillus anthracis</i>	<sup>64</sup>
<i>Weissella oryzae</i> (Bacteria)	10-30	<i>Vibrio parahaemolyticus,</i> <i>Bacillus cereus,</i> <i>Bacillus anthracis,</i> <i>Staphylococcus aureus,</i> <i>Escherichia coli,</i> <i>Candida albicans,</i>	<sup>65</sup>
<i>Arthroderma fulvum</i> (Fungi)	15.5±2.5	<i>Candida albicans,</i> <i>Candida parapsilosis,</i>	<sup>66</sup>

		<i>Candida krusei,</i> <i>Candida tropicalis,</i> <i>Aspergillus fumigatus,</i> <i>Aspergillus flavus,</i> <i>Aspergillus terrrus,</i> <i>Fusarium solani,</i> <i>Fusarium moniliforme,</i> <i>Fusarium oxysporum</i>	
<i>Bhargavaea indica</i>  (Bacteria)	30-100	<i>Vibrio parahaemolyticus,</i> <i>Salmonella enterica,</i> <i>Staphylococcus aureus,</i> <i>Bacillus anthracis,</i> <i>Bacillus cereus,</i> <i>Escherichia coli,</i> <i>Candida albicans</i>	<sup>67</sup>
<i>Bacillus pumilus,</i>  <i>Bacillus persicus,</i>  <i>Bacillus licheniformis</i>  (Bacteria)	77-92	<i>Escherichia coli,</i> <i>Shigella sonnei,</i> <i>Pseudomonas aeruginosa,</i> <i>Klebsiella pneumonia,</i> <i>Streptococcus bovis,</i> <i>Staphylococcus epidermidis,</i> <i>Staphylococcus aureus,</i> <i>Aspergillus flavus,</i> <i>Candida albicans,</i>	<sup>68</sup>

<i>Listeria monocytogenes</i> , <i>Bacillus subtilis</i> , <i>Streptomyces anulatus</i> (Bacteria)	Various shapes and sizes	<i>Chrysosporium keratinophilum</i>	<sup>69</sup>
<i>Candida utilis</i> (Fungi)	20-80	<i>Pseudomonas aeruginosa</i> , <i>Staphylococcus aureus</i> , <i>Escherichia coli</i>	<sup>70</sup>
<i>Caulerpa racemose</i> (Algae)	5-25	<i>Staphylococcus aureus</i> , <i>Proteus mirabilis</i>	<sup>71</sup>
<i>Chlorella vulgaris</i> (Algae)	40-90	NA	<sup>72</sup>
<i>Chlorella vulgaris</i> (Algae)	24	<i>Salmonella enterica</i> subsp. <i>enterica</i> serovar <i>typhimurium</i> , <i>Staphylococcus aureus</i>	Current study

Being capable of stabilizing AgNPs, proteins and sugars of biological molecules used as reducing and stabilizing agents during synthesis are salient biotic components contributing to NP interactions with other organisms as well as microorganisms, which results in enhanced antimicrobial properties of the formed NPs. By making contact with the cell membrane and without penetrating it, AgNPs can apply the antibacterial effect and cause the death of microorganisms. AgNPs benefit from extremely high antimicrobial effects thanks to the high concentration of silver ions, and effects of particles on cell membranes which still could be effected by factors such as light conditions, utilized media and the size of particles. Also, they possess higher durability as antimicrobial coating agent compared with  $\text{AgNO}_3$ <sup>73,74</sup>. In the case of the energy needed for the synthesis, although numerous well-established techniques are available, the synthesis method must contain simplified and cost-effective procedures and be capable of increasing the reaction rate by orders of magnitude. Moreover, short reaction periods and higher efficiency to produce pure NPs are significant factors to be considered when

choosing a method to synthesize NPs. Fulfilling the abovementioned criteria, MI as a desirable and primary heating method surpasses conventional heating methods<sup>75,76</sup>. In 2,000, the required energy for the synthesis of PbTiO<sub>3</sub> NPs using ethylene glycol as a RA was provided by MW. This new method of supplying energy was investigated by Palchik et al.<sup>77</sup>. Due to striking features, including being fast, straightforward, and energy-saving, the Palchik group made use of this method for the acceleration and stabilization of the reactions. The average diameter of the NPs obtained through this method was around 15 nm, and only 1 min of MW heating was applied in order to supply the energy required for the reaction. The MW-assisted synthesis method produces NPs with lower dispersion, which is arranged in a more regular pattern. It is noteworthy that the shape and morphology of the formed NSs can be controlled in this procedure. The mono mode (also known as single mode) and multimode reactors are the two categories into which MW instruments may be categorized. Only one reactor vessel may be irradiated at a time in mono-mode reactors; while many vessels can be irradiated simultaneously in multimode reactors. Instead of using heat transfer like traditional heating, MW radiation uses an energy transformation from electromagnetic to thermal energy. The substance receives MW energy effectively thanks to molecular interactions with electromagnetic radiation. The two primary ways for transmitting energy from MW technologies to the material being heated are dipole rotation (The polar molecules rotation for becoming aligned with the electrical field to which it is exposed), and ionic conduction (The back and forth moving of the ions under the effect of changing electric field). The MW-based heating occurs when electromagnetic field interacts with molecules' dipole moments, however with MW techniques, dipole moments rotate to line up with the alternating electric field. Therefore, it is thought that the ideal solvents to be used in MW-based syntheses are water or ionic liquids having a large dipole moment. For those solutions which have ions when temperature rises, the ionic conduction increases as well. As a result, dipole rotation contributes most to the process' initial heating in the case of MW usage as a heating source. However, when the temperature rises, ionic conduction takes control of the heating process.<sup>75</sup>.

**Figure 2-1** summarizes the main methods of synthesis along with subdivisions of green synthesis. The schematic illustration of AgNPs in this report is also presented.

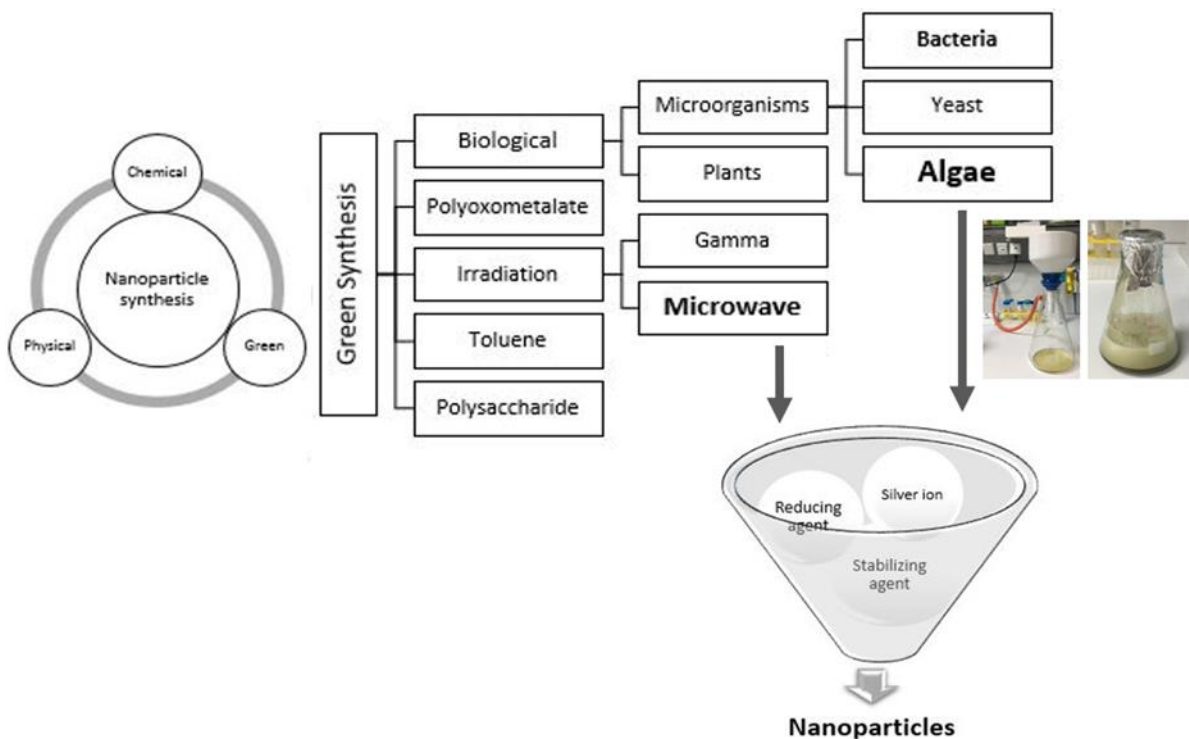


**Figure 2-1:** This figure represents the main methods of NP synthesis as well as subdivisions of green synthesis along with a schematic demonstration of the current AgNP formation.

In this study, the dried biomass of *Chlorella vulgaris* algae was used for the first time in the MW-assisted green synthesis of AgNPs. As presented in **Table 2-1**, only a few studies have been conducted so far with algae for NP synthesis, and only a limited number of tests regarding antibacterial activity have been investigated. Here, we also report the antibacterial activity of the formed AgNPs against well-known foodborne pathogens, including *Salmonella enterica* subsp. *enterica* serovar *typhimurium* (Gram-) and *Staphylococcus aureus* (Gram+).

## 2.2 Materials and Methods

### 2.2.1 Materials

$\text{AgNO}_3$  with a purity of 99.9% as an Ag ion precursor was provided by Merck (Germany). Foodborne pathogens, *Salmonella enterica* subsp. *Enterica* serovar *typhimurium* (ATCC® 14028™) and *Staphylococcus aureus* (ATCC® 29213™), were acquired from American Type Culture Collection (ATCC, USA). Nutrient agar (NA) and nutrient broth (NB) as a cultivation medium were bought from Oxoid Ltd (Hampshire, England).

### 2.2.2 Methods

#### Algae Preparation

**Surfactant** The cultivation of microorganisms in the BG11 medium was done by the flask-shake method<sup>70</sup>. *Chlorella vulgaris* cells were collected through centrifugation at 10,000 rpm for 15min. Then, the supernatant was separated, and the pellet was cleaned using sterile water. The glass plates were used for heat drying of algal biomass at 55°C for 24 h. As a final step, dried biomass was removed from the plates and powdered using a mortar. The heat-dead biomass used in this assay can be handled and stored easily without any need for nutrient supply. Finally, biomass powder (1.6 g) was mixed with 100mL of deionized water in an Erlenmeyer flask with a magnet inside it, kept on stirring at 50°C for 3 h and at 10°C for 21 h to be well dispersed. Then the solution was filtered using filter paper and a vacuum filtration unit. The supernatant was kept in the fridge for further reaction and analysis.

### **NP synthesis**

For the synthesis of AgNPs, 10 mL of *Chlorella vulgaris* was mixed with 90 mL of an aqueous solution of AgNO<sub>3</sub> (1 mM solution) and heated by MW at the power of 180W for various time intervals. In order to take the sample from the solution during the heating process and prevent overheating, MW radiation was applied for 2 min by 15 s delay for a total heating time of 10 min. The bioreduction of Ag<sup>+</sup> ions in the solution was checked by regular sampling (2 mL) of the suspension, then the UV-visible spectra of the taken sample were measured. The synthesis reaction was monitored by the UV-visible spectra, as well as by monitoring the color change in the reaction solution. Gradually, the original light-green color of the solution changed to red-brown color, indicating the formation of AgNPs. In all steps, the synthesized AgNPs were sonicated and filtered.

### **Characterization of NPs**

The change in the color of the mixture containing the AgNO<sub>3</sub> solution and *Chlorella vulgaris* was monitored by visual observation. In order to confirm the formation of AgNPs, the reaction mixture was sampled at constant intervals of time. Following this, the  $\lambda_{\text{max}}$  was measured at 350–800 nm using a spectrophotometer (Cary 5000 UV-Vis-NIR, USA), which works based on surface plasmon resonance (SPR). In the aforementioned range, the excitation of surface plasmon vibration bands leads to a considerable alteration in the solution color. Due to the relationship between the absorbance of the produced AgNPs and their concentration, the synthesized AgNP concentration can be easily determined by UV-Vis spectroscopy in a 10mm optical path quartz cuvette containing 1 mL of the target sample<sup>73</sup>. The FTIR analysis of AgNPs, including *Chlorella vulgaris* and unmixed *Chlorella vulgaris*, was done to determine

the functional groups of *Chlorella vulgaris* and estimate their role as reducing or stabilizing agents in AgNP synthesis using an FT-IR spectrophotometer with a deuterated triglycine sulfate detector (Thermo Scientific Nicolet iS10, USA). The range used to record the FT-IR spectra was 4,000–400 cm<sup>-1</sup>. The mean hydrodynamic size of the synthesized AgNPs was evaluated using a dynamic light scattering (DLS) analyzer (Zetasizer Nano ZS, Malvern, UK) with a 10mm optical path quartz cuvette containing 1mL of the target sample. Brownian motion, as a principle used in this device, causes scattered light intensity fluctuations, which are measured by the DLS analyzer <sup>44</sup>. This measurement leads to the determination of the number of particles as well as their hydrodynamic size in a solution. In the case of the size distribution of the particles, the PDI of NP, as a value varying from zero to one, can be computed using this device. In order to detect and calculate the surface charge of the synthesized AgNPs, their value of zeta potential, as a demonstration of their stability, can be provided at 25°C by the DLS analyzer <sup>44</sup>. Further insight into the morphology of the formed AgNPs, comprising size as well as shape, was provided using a scanning electron microscope (SEM) with a focused electron beam (Zeiss Leo Supra 35 VP, Germany) along with a transmission electron microscope (TEM; CM120, Philips, Amsterdam, The Netherlands) with an acceleration voltage of 120 kV. In order to provide a sample for both SEM and TEM analyses, 5 µL of the targeted solution was dropped on a silicon wafer and left to dry at RT for a couple of hours.

### **Antibacterial activity**

Antibacterial effects of the green-synthesized NPs were tested using liquid and solid nutrient media on the agar plates. For each bacterium, the suspension provided by mixing 500 µL of NB with 50 µL of target bacterium was vortexed well as a first step, and five small test tubes were taken and 5mL of NB was added in each tube. Then, 100 µL of the suspension containing NB and the bacterium was added to each test tube. Following this, 30, 60, 90, and 300 µL of the formed AgNPs was added to the second, third, fourth, and fifth tubes, respectively, to monitor the effect of AgNPs on bacterium growth. The AgNP solution was not added to the first tube, which was used as a control culture. Finally, all five tubes were incubated for 24 h at 37°C. Then, 200 µL of the bacterial suspensions prepared in each of the five tubes were inoculated into plates containing culture media of NA. Finally, the plates were placed in an incubator at 37°C for 24 h.

## 2.3 Results and Discussion

### 2.3.1 Characterization of NP formation

As presented in **Figure 2-2**, the specific color change in the solution containing  $\text{AgNO}_3$  and *Chlorella vulgaris* from pale green to reddish brown was the initial demonstration of the AgNP formation, and this color change is because of the excitation of vibration bands related to SPR<sup>6</sup>.

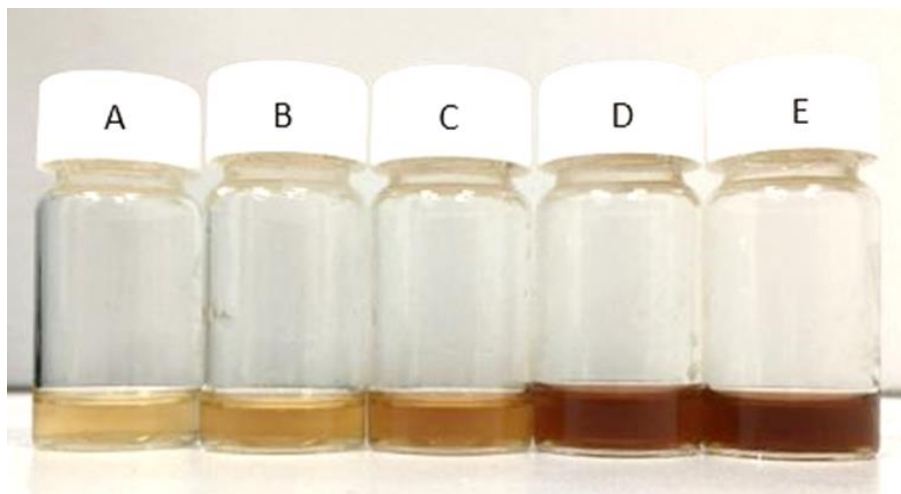


**Figure 2-2:** Various stages of AgNP formation after 2 (A), 4 (B), 6 (C), 8 (D), and 10 (E) min of MW radiation.

The synthesis of AgNPs was verified by broad  $\lambda_{\max}$  at wavelengths ranging from 380 to 450 nm. Owing to the SPR of AgNPs, the bands outlined above are ordinary absorption bands of these NPs. Noteworthy is the fact that the absorption of AgNPs was also reported between 410 and 440 nm in other research studies<sup>2,47</sup>.

**Figure 2-3** reveals that  $\lambda_{\max}$  of the synthesized AgNPs was obtained at 431 nm with a concentration of 59.22 ppm, an indication of the successfully formed AgNPs, which was in the desirable range for AgNPs. In the first 4min, no peak was noticed, confirming that no target product was formed. After 6min of being exposed to MI, the SPR band for NPs was obtained. A consistent growth was noticed in the intensity of synthesis with an increase in irradiation time without any considerable change in the peak position. Thus, the synthesized NP with higher intensity was achieved at 10 min. It is worth mentioning that the irradiation time of more than 10 min led to the evaporation of all remaining solutions.

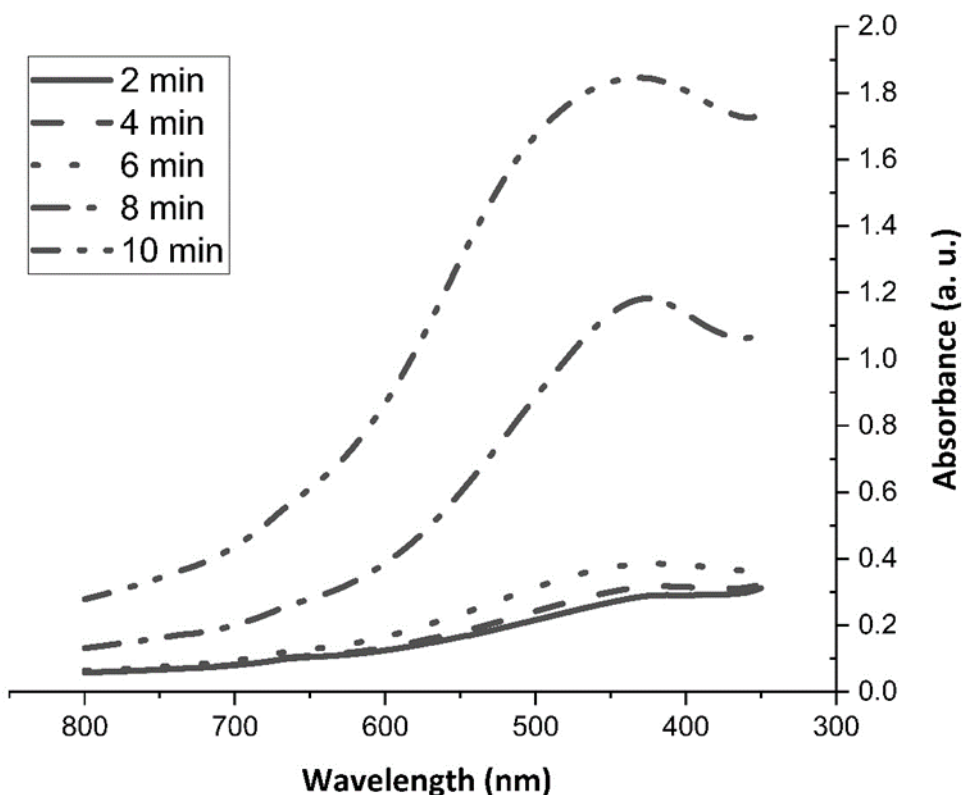


**Figure 2-3:** Recorded UV-Vis spectra of the provided AgNPs according to the MW exposure time.

The FT-IR spectra related to unmixed algae, as well as AgNP solutions, were analyzed to determine the various functional groups related to *Chlorella vulgaris*, which are responsible for the reduction of the  $\text{Ag}^+$ . Furthermore, the intensity of several regions can be noticed using this spectrum. As noted in **Figure 2-4**, two sharp absorption peaks exist at 3262.98 and 1635  $\text{cm}^{-1}$ . The peak with the shape of U at around 3,200–3,300  $\text{cm}^{-1}$  contains both O–H hydroxyl and N–H amine groups. Moreover, a broad peak between 1,621 and 1,645  $\text{cm}^{-1}$  is related to the amide I band due to the carbonyl bond. A weak peak at around 2151.54  $\text{cm}^{-1}$  corresponds to the N–C compounds. Also, the –NH<sub>2</sub> bond of the protein or polysaccharide in *Chlorella vulgaris* appears as a peak at the wavelength of 1,155  $\text{cm}^{-1}$ . Following this, the absorption bands at 1,081  $\text{cm}^{-1}$  and 1,036  $\text{cm}^{-1}$  can be attributed to the v(C–O–C) bond of polysaccharides that existed in *Chlorella vulgaris*. Between 1,036 and 3262.98  $\text{cm}^{-1}$ , the abovementioned peaks can also be noticed in the infrared band of *Chlorella vulgaris*, including NPs. A considerable shift in some of these peaks indicates the possible involvement of the carbonyl group and peptides of proteins related to algae in the synthesis of target NPs. *Chlorella vulgaris* is rich in proteins and carbohydrates, providing a group of polysaccharides, which are of great importance in the composition of this alga. The results obtained are consistent with those of the study by Duygu et al.<sup>78</sup>. The FT-IR spectrum of *Chlorella vulgaris*, obtained by their group,

was a confirmation of the presence of proteins, groups of carbonyls, as well as polysaccharides involved in the reduction of  $\text{Ag}^+$  along with stabilization of AgNPs.

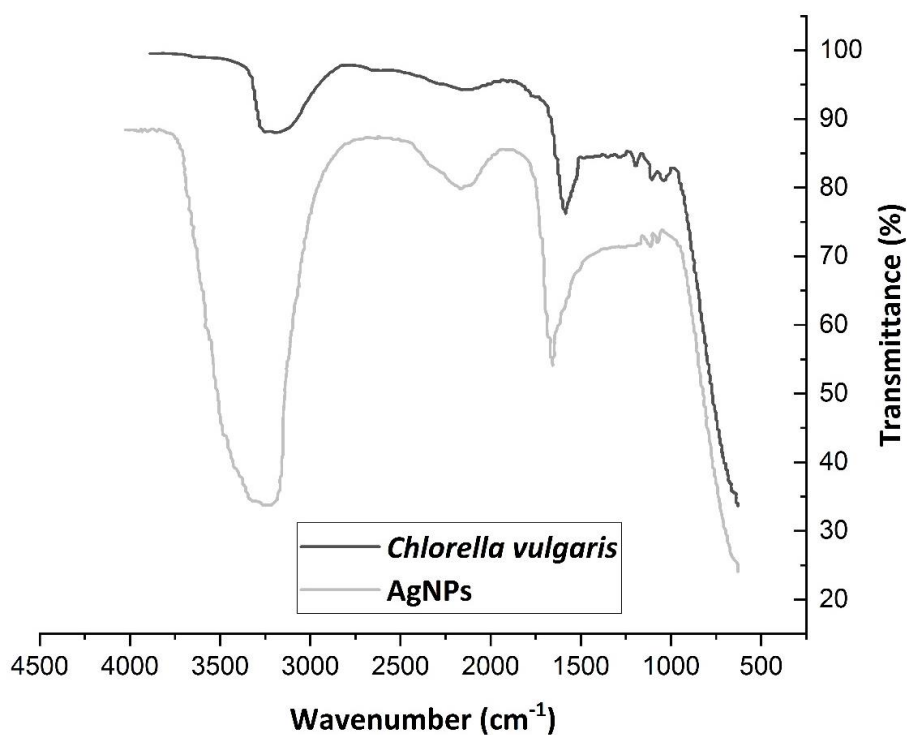


**Figure 2-4:** FT-IR spectra of *Chlorella vulgaris* and prepared AgNPs.

**Figures 2-5 and 2-6** show the mean hydrodynamic size, PDI, and zeta potential of the formed NPs, which are 24.79 nm, 0.252, and  $-17\text{ mV}$ , respectively. With regard to the hydrodynamic size distribution pattern, particles with a size smaller than 100 nm are more noticeable after applying 2 min of MI and increasing the MW exposure time up to 10 min results in NPs with smaller hydrodynamic size. Finally, particles in the interval of 10-40 nm are obtained after 10 min of exposure to MI (**Figure 2-5**). The AgNPs with lower PDI are more acceptable, and the PDI value of 0.252 in the current assay indicates the excellent distribution of particles in the target solution. A zeta potential of  $-17\text{ mV}$ , as an indicator of the electrical cloud around the NPs, reveals the high stability of the synthesized NPs. Due to the electric repulsion between particles, higher surface charge results in more stable suspension. It is worth mentioning that by periodic sampling of the suspension during 10 min of MW exposure, the zeta potential values of the particles after 2, 4, 6, 8, and 10 min were measured and provided in **Figure 2-6**. The value of zeta potential related to the formed NPs was somewhere in the vicinity of  $-17\text{ mV}$  during this 10 min of reaction time. The results reported in this experiment are consistent with those of the previous experiments of Składanowski et al. and Elbeshehy et al.<sup>61,68</sup>. Składanowski and coworkers found the zeta potential of the formed AgNPs using *Streptomyces*

sp. to be  $-19.4$  mV. In the assay carried out by Elbeshehy et al., AgNPs formed by *Bacillus* spp. had a zeta potential of  $-18.5$  mV.

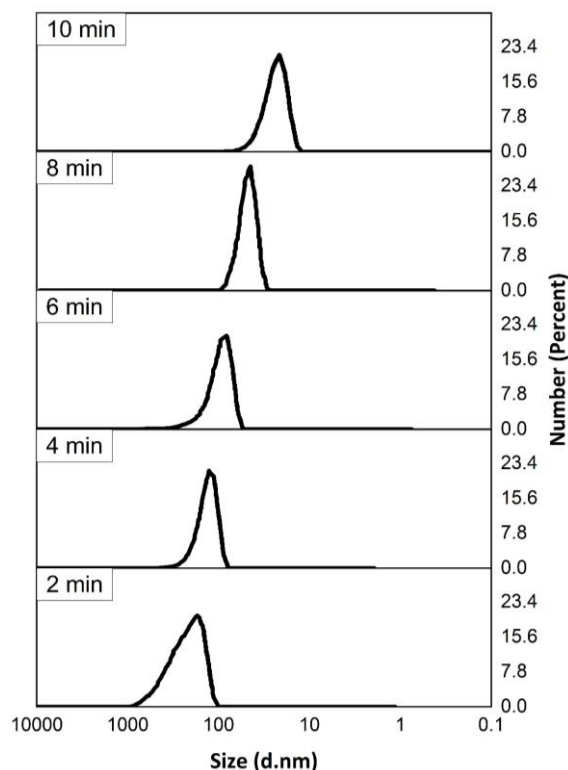


**Figure 2-5:** The hydrodynamic size distribution of the synthesized AgNPs after 2, 4, 6, 8, and 10 min of being exposed to MW radiation.

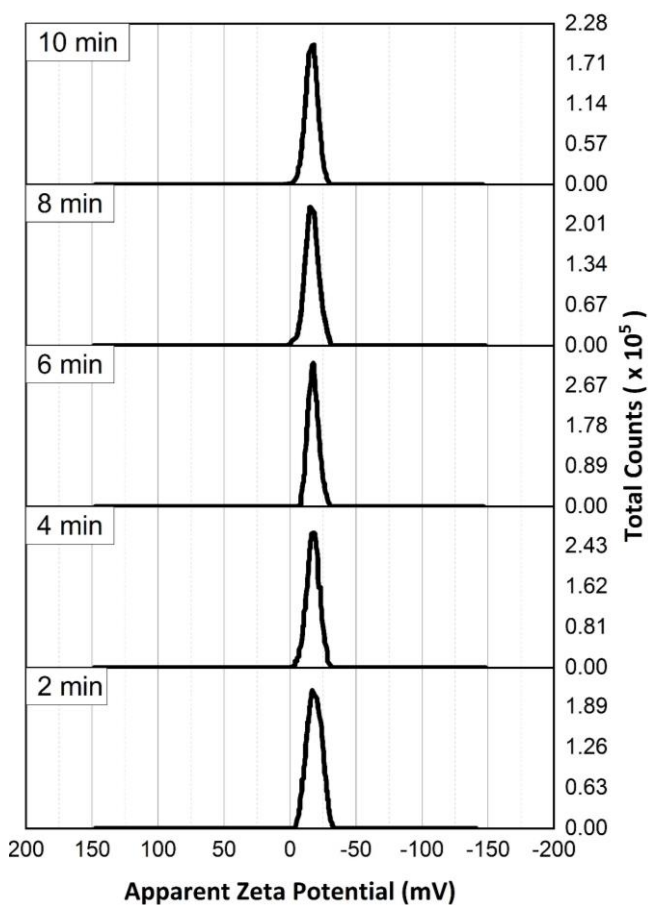


**Figure 2-6:** Zeta potential of the synthesized AgNPs after two, four, six, eight, and ten-minute exposure to MW radiation.

As represented in **Figures 2-7 and 2-8**, TEM and SEM analyses clarify the size as well as the morphology of the synthesized NPs. **Figures 2-7 and 2-8**, respectively, indicate that most of the AgNPs synthesized by *Chlorella vulgaris* are spherical and quasi-spherical with flat edges. Following this, NPs with allotropic structures that have asymmetrical curves can be detected. Also, some of them are rectangular spheres, decahedral, and polygonal in shape. Being well dispersed with no aggregation, AgNPs have a size between 1 and 50 nm with an average size of 24.79 nm. Noteworthy is the fact that the difference in the size distribution of NPs can be related to the contribution of various molecules and functional groups to the reduction of silver ions and stabilization of AgNPs<sup>43</sup>. The formed AgNPs are surrounded by a thin capping layer of material obtained from the aqueous extract of *Chlorella vulgaris*, which can be spotted in these images. The capping agent substantially prevents the AgNP aggregation and consequently leads to the formation of NPs with higher stability<sup>50</sup>. The shape of particles has a significant role to play in the stability of NPs, and spherical NPs are highly stable in comparison with other shapes of NPs<sup>73</sup>. Also, a zeta potential value of -17 mV of the formed NPs is an excellent demonstration of the high stability of particles in the nanoscale.

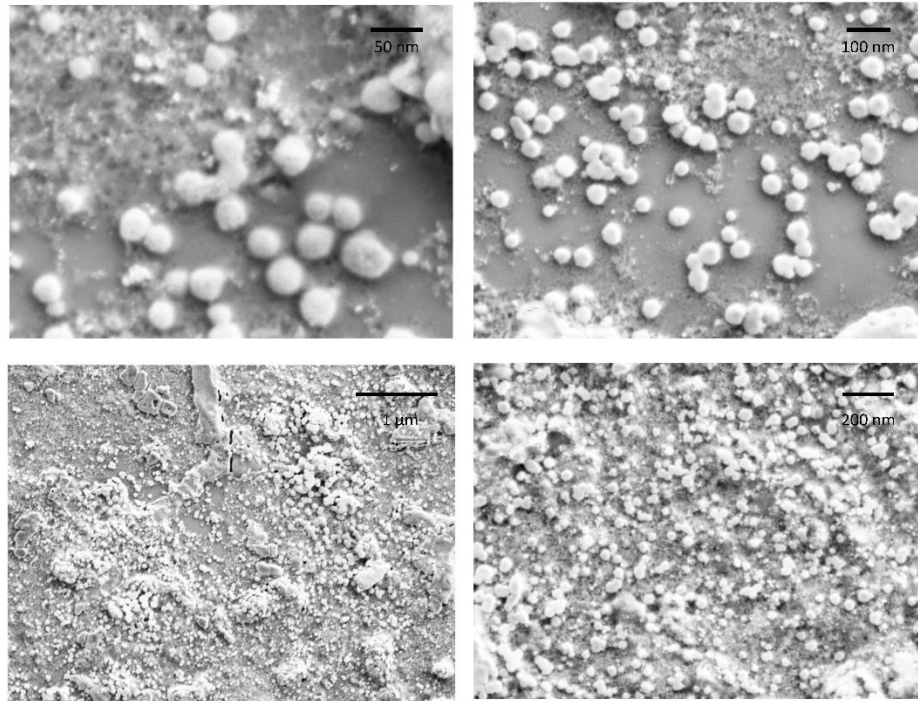


**Figure 2-7:** SEM images related to the produced AgNPs in various scale bars.

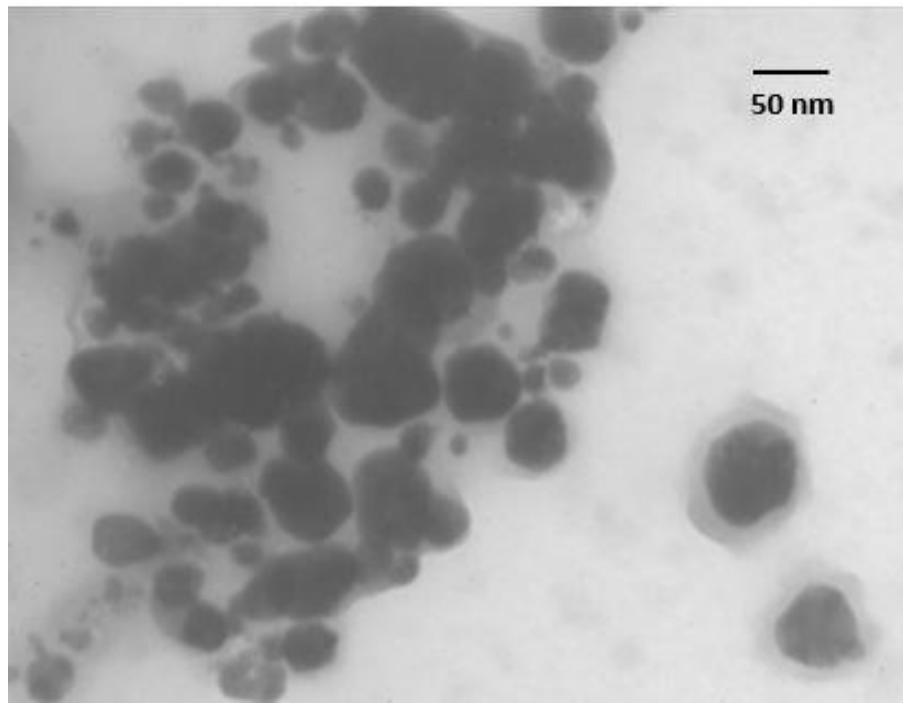


**Figure 2-8:** TEM images related to the produced AgNPs.

### 2.3.2 Antibacterial activity of the AgNPs

The antibacterial effect of AgNPs on *S. typhimurium*, as well as *Staphylococcus aureus* bacteria, as a function of the volume of the synthesized AgNPs, is shown in **Figure 2-9**. As revealed in this figure, increasing the volume of the AgNP solution has a considerable

detrimental effect on the bacterial growth rate for both bacteria. In the case of *Staphylococcus aureus*, a decrease in the number of colonies in the second, third, and fourth plates can be noticed, and the fifth tube (A5) is empty without any bacteria. In the case of *S. typhimurium*, the formed AgNPs have a more substantial antibacterial effect on this bacterium (Gram-) in comparison with the first one (Gram+), and the plates empty without any bacterium are shown in B3–B5 in **Figure 2-9**. The free positive ions of NPs stick to the negatively charged cell walls of both types of bacteria and apply their antibacterial effect on them. Studies in the past few years also confirmed higher resistance of Gram-positive bacteria against AgNPs in comparison with Gram-negative bacteria<sup>79</sup>, which can be justified by the difference in the structure of the cell walls. Being covered by a layer of lipopolysaccharides and peptidoglycans, the cell of Gram-negative *S. typhimurium* is more susceptible to the entrance of AgNP ions. In Gram-positive bacteria, such as *Staphylococcus aureus*, the peptidoglycan layer as a protective coating is thicker when compared with that of Gram-negative bacteria. Furthermore, lipopolysaccharide with a negative charge can be another remarkable reason. The Gram-negative bacteria are coated with this molecule, which has a considerable affinity for NP ions. As a result, the growing uptake of ions leads to intracellular destruction. The findings in this article are in line with those of Jo et al.<sup>64</sup> and Priyanka Singh et al.<sup>67</sup>, indicating that the synthesized AgNPs have a more destructive impact on Gram-negative than Gram-positive bacteria.

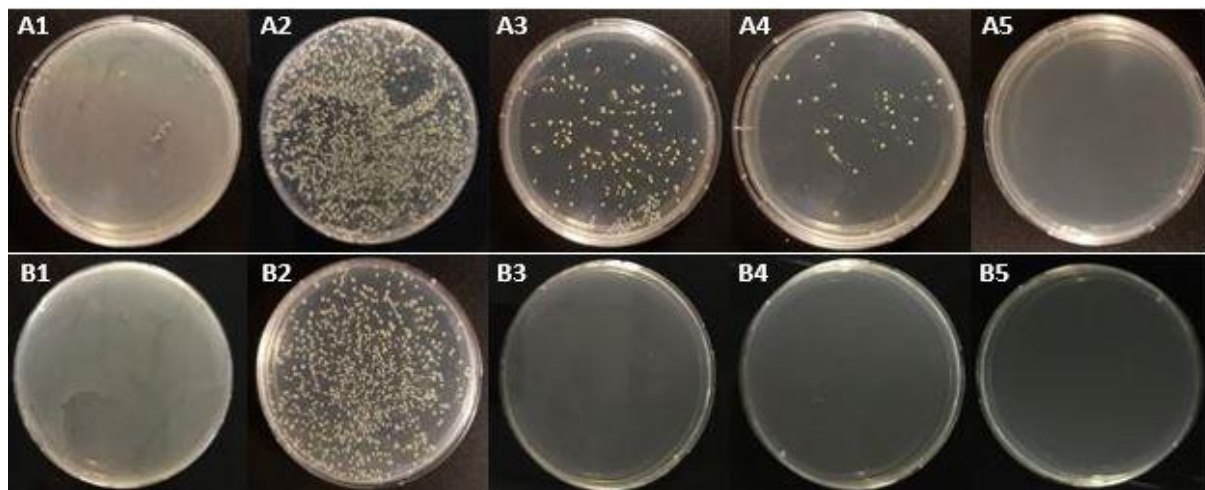


**Figure 2-9:** Growth of *Staphylococcus aureus* (A) and *S. typhimurium* (B) on NA plates containing 0 (1) 30 (2), 60 (3), 100 (4), and 300 (5)  $\mu\text{L}$  of AgNP solution.

## 2.4 Conclusion

This study demonstrated an unsophisticated green synthesis of AgNPs, as a feasible alternative to the chemical as well as physical methods, by effectual bioreduction of  $\text{Ag}^+$  using *Chlorella*

*vulgaris*, actively acting as reducing and stabilizing agents. With regard to the dried extract of *Chlorella vulgaris*, various functional groups that existed in this extract are responsible for the synthesis. Instead of other time-consuming energy supplies, MI was used as an abundant energy source. Mostly spherical NPs with sizes ranging from 1 to 50 nm and an average size of 24 nm could be monitored by SEM and TEM. Also, the distinctive inhibition effect of the formed NP against a variety of bacteria was represented. In future directions, another natural stabilizer besides *Chlorella vulgaris* can be used to obtain AgNPs with higher stability. Due to the potential of *Chlorella vulgaris* in being used as both a reducing and stabilizing agent, the synthesis of other MNPs can also be examined. There are other heating methods such as autoclaves that can be assessed as an alternative energy supply to MI to find out whether they work or not. Besides the considerable progress in nanobiotechnology, the more futuristic visions of nanoscience consist of the widespread use of NPs in biomedical and pharmaceutical applications.

## **Chapter 3: A MICROWAVE-POWERED CONTINUOUS FLUIDIC SYSTEM FOR POLYMERIC NANOCOMPOSITE MANUFACTURING: A PROOF-OF-CONCEPT STUDY**

### **3.1 Introduction**

Manufacturing pure nanocrystals with a narrow size distribution in a polymer matrix is very challenging, although it is highly crucial to get their full potential for advanced applications. In general, conventional or MW heat sources have been utilized to nucleate NPs. Still, the latter has recently become highly attractive due to its fast, sustainable, and homogeneous heating and energy efficiency<sup>12,80–82</sup>. The real-world applications in energy, environment, and healthcare usually require the stabilization<sup>83,84</sup>, and the large-scale synthesis<sup>85</sup> of small NPs with narrow size distribution, which are two critical factors to benefit from the fascinating properties. By traditional techniques (e.g. mechanical mixing), maintaining homogeneous and stable dispersions of NPs in matrices and the interaction of these particles with active sites (e.g. surface functional groups) of the matrix have always become significant bottlenecks and generally been restricted by agglomeration and poor solubility of mixing particles, resulting in a substantial decrease in the chemical and physical properties of the end composites<sup>86–90</sup>. To stabilize the NPs, post-synthetic- or in-situ-techniques such as ligand<sup>91</sup> and surfactant-assisted<sup>92</sup> methods have been employed<sup>93</sup>. In addition, the abovementioned heat sources have been combined with the fluidic reactors to partially overcome the issue of producing the NPs continuously<sup>94,95</sup>.

In our previous studies, the MW-powered fluidic system was shown to prepare AuNPs<sup>94</sup> (~4 nm) and hematite superstructures<sup>96</sup> (~200 nm) continuously. However, the HRTEM analysis indicated that the primary hematite NPs were 5–10 nm in size. Similarly, monodisperse bismuth NPs have recently been prepared under MWF conditions, and excess citrate ions and pH control acquired their stabilization<sup>97</sup>. These studies specified the importance of proper support while preparing a stable colloidal dispersion of NPs in the MWFS. Polymers, particularly bearing functional groups, can act as stabilizers while preparing NP/polymer NCs. However, the distribution of the NPs in polymer matrices is of great importance. Thus, particular polymers and NPs are desired for the target applications. A MW-assisted batch synthesis method for the preparation of metal NP/polyacrylamide NCs was developed in ethylene glycol. It was employed to prepare homogeneously dispersed Pt, Ag, or Cu NP-containing polyacrylamide

<sup>98</sup>. In this study, both the NPs and the polymer were synthesized in-situ using metal salt precursors and an acrylamide monomer. For the AgNPs, the smallest size synthesized at 125 °C was  $7.0 \pm 3.9$  nm. However, the reactor size, in other words, the production capacity was limited to the cavity of the MW synthesis system used. In a recent study <sup>99</sup>, the single-step solvent-free in-situ melt processing method effectively prepared AgNP-containing composites of PA6, polylactic acid, and polypropylene. The produced AgNPs in the PA6 matrix showed a broad size distribution ( $20 \pm 18$  nm) after 5 min processing at 240 °C. In contrast, larger NPs with a slightly narrow size distribution ( $26 \pm 9$  nm) were obtained after 10 min processing. The abovementioned studies prepared laboratory-scale polymer NCs containing AgNPs with varying sizes and distribution. However, there is still a real need to develop a universal, efficient, and potentially scalable method to manufacture NMs with controllable particle size, distribution, and morphology in a matrix.

Herein, a sustainable method of coupling MW heating with fluidic synthesis is introduced to continuously manufacture polymer NCs at low temperatures. The system is used for preparing nylon-6 NCs with homogeneously distributed sub-5 nm AgNPs. The reaction parameters such as FR, reagent concentration, and MWP are studied thoroughly to tune the size of the AgNPs in the polymer matrix. The optimized reaction conditions are equally tested in a CHFS. Under optimized experimental conditions, the MWFS yielded sub-5 nm AgNPs (~3 nm) in the nylon-6 matrix continuously and reproducibly. In contrast, the CHFS formed AgNPs ~35-100 nm in size, and a fast aggregation was observed in a MW batch system. The prepared AgNP/PA6 NCs were subjected to antimicrobial activity tests using *Escherichia coli*, *Staphylococcus aureus*, and *Pseudomonas aeruginosa*. Given the small size of the produced AgNPs in the PA6 matrix by the MWFS, the NC films (~120 nm in thickness) showed superior efficacy over the NC produced by the CHFS, directly confirming the NP size effect on the antimicrobial activity.

## 3.2 Materials And Methods

### 3.2.1 Materials

Silver nitrate ( $\text{AgNO}_3$ , ≥99.8%, ISOLAB), sodium borohydride ( $\text{NaBH}_4$ , >99%, Fluka), and polyamide 6 (PA6) ( $(\text{C}_6\text{H}_{11}\text{NO})_n$ , >99%) were used as received. Formic acid (FA, 98-100%, Fisher Chemical) and N, N-dimethylformamide (DMF, >99.8%, Merck) were used as the solvents.

### 3.2.2 Methods

#### The MWFS

The designed MWFS is composed of several components. The home-built fluidic reactor, Teflon-made tubing with a diameter of 1/8 inches and a total volume of 8 mL, is one of the main components. A single-mode MW system (Discover, CEM Microwave Technology Ltd) is used as the power source. The fluid temperature is monitored by a temperature display unit (OMEGA, HH801B) with a compact transition joint probe (OMEGA, WNW0187979) placed 11 cm away from the MW heating zone. The inside pressure of the system is regulated by a 20 psi pressure regulator (IDEX Health and Science). A dual infusion syringe pump (KD Scientific) with two 60 mL syringes (Luer-Lock) are used to feed the fluidic reactor, and two glass bottles are used to collect the product and waste separately.

### **Preparation of the AgNP/PA6 NC<sub>MWF</sub>**

As a first step of the AgNP/PA6 NC<sub>MWF</sub> synthesis, suitable solvents were chosen based on factors such as greenness, energy efficiency, and solubility of polymers in them. Small chain alcohols, dimethyl sulfoxide (DMSO), and nitrobenzene are high MW absorbers that heat up fast in the MW chamber due to their high dielectric losses. However, DMF, FA, butanols, acetonitrile, and water are typical organic solvents classified as medium MW absorbers. Also, FA is a versatile renewable reagent for green and sustainable chemical synthesis. The solubility of precursors (AgNO<sub>3</sub> and NaBH<sub>4</sub>) along with polymer (PA6) in suitable solvents (DMF and FA) was tested. FA was chosen as a solvent for the synthesis of the NCs since it yielded a relatively concentrated PA6 solution at RT and did not act as a RA.

In typical experiments, fresh solutions of PA6/AgNO<sub>3</sub> (0.8 g of PA6/0.001 M in 100 mL of FA) and NaBH<sub>4</sub> (0.002 M) were prepared. To initiate the experiment, one of the syringes was filled with freshly prepared NaBH<sub>4</sub> solution, and the PA6/ AgNO<sub>3</sub> solution was added to the second syringe. The infusions started immediately after the preparation step. Before applying MW irradiation, it was ensured that the fluidic reactor was filled with the reaction fluid. After that, the prepared solutions were infused independently at an FR ratio of 3: 1 (3 mL min<sup>-1</sup> for NaBH<sub>4</sub>: 1 mL min<sup>-1</sup> for PA6/AgNO<sub>3</sub>) under varying MWPs of 10, 20, 30, 40, and 50 W. The system pressure was set to 20 psi. Using the above MWPs, the AgNP/ PA6 NCs<sub>MWF</sub> were also manufactured at the FR ratios of 3: 0.5, 3: 0.25, and 3: 0.1. To evaluate the effect of PA6 concentration, in addition to 0.8 g PA6 in 100 mL of FA, three more concentrations (0.1, 0.2, and 0.4 g PA6 in 100 mL of FA) were also investigated using FR ratios of 3: 1, 3: 0.5, 3: 0.25, and 3: 0.1 at MWP of 40 W. The freshly prepared AgNP/PA6 NC<sub>MWF</sub> solution was used for UV-vis and DLS analysis. The freshly prepared solution of the AgNP/PA6 NCs<sub>MWF</sub> was added to distilled water dropwise under vigorous stirring to quench the reaction and remove the water-

soluble unreacted reagents. The formed precipitate was collected by filtering through a PTFE membrane (0.45 µm, ISOLAB) and washed with distilled water. After drying in an oven at 40 °C overnight, the resulting solid AgNP/ PA6 NC<sub>S<sub>MWF</sub></sub> was used for bulk analysis.

### Preparation of the AgNP/PA6 NC<sub>CHF</sub>

For comparison, the AgNP/PA6 NC<sub>CHF</sub> was prepared in the same fluidic reactor using an FR ratio of 3: 1 at 50 and 55 °C. In addition, an oil bath was used as a heating source instead of MW irradiation. The prepared NCs were analyzed and, after that, isolated as described in the above procedure.

### Antibacterial tests

Regarding the antibacterial activity of the synthesized polymeric NCs, the Japanese Industrial Standard (JIS) technique (JIS Z2801:2010) (JSA, 2000) was applied, whose graphical illustration is presented in **Figure 3-1**.

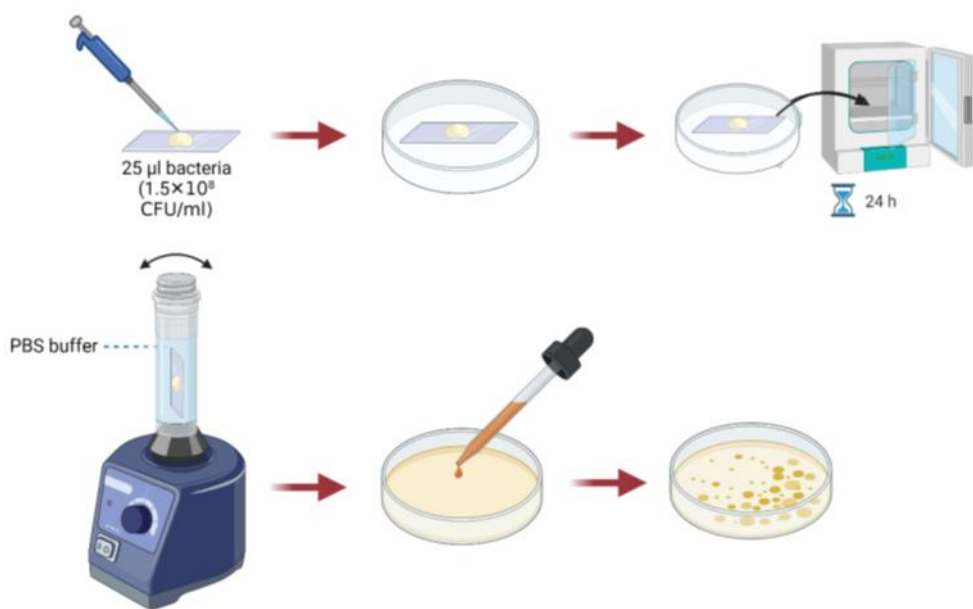


**Figure 3-1:** Graphical illustration of method applied on PA6 and NC coated glasses for evaluation of their antibacterial efficiency.

Considering commonly practiced bacteria with PA6, two Gram-negative bacteria, *Pseudomonas aeruginosa* and *Escherichia coli*, and a Gram-positive bacterium, *Staphylococcus aureus*, were chosen for antibacterial evaluation. A single colony of bacteria was inoculated in a 5 mL Lysogeny broth and incubated at 37 °C for 24 h. A dilution step followed this to adjust the number of bacteria to  $1.5 \times 10^8$  CFU per mL, and the diluted sample was utilized for further assessment. Following this, a 12 × 12 mm control (uncovered) and

AgNP/PA6 NC-covered films were prepared for each bacterium. In this step, the film was sterilized using ultraviolet irradiation in a laminar flow hood, and then 25 µL of culture medium containing bacteria was poured on it. Next, the film was put in a Petri dish with the lid closed. After incubating at 37 °C for 24 h, the sample was placed in 50 mL tubes and washed with 10 mL of PBS for 5 min. Following this, 1 mL of the solution was added to the next vessel with 9 mL of PBS, which was followed by a mixing step. The abovementioned dilution step was repeated to reach 6-fold serial dilutions. The last sequential steps were applied for both covered and uncovered films. Next, 1 mL taken from the final diluted solution was homogeneously spread in a Petri dish of nutrient broth and left in an incubator for 24 h – incubation at 37 °C. The equation presented below was utilised for the calculation of the antibacterial rate based on the JIS Z2801:2010 regulation <sup>100</sup>:

$$\text{Antibacterial rate (\%)} = (100) \times \frac{Nr - Nc}{Nr}$$

where  $N_r$  and  $N_c$  stand for the number of viable bacteria on free film and the number of viable bacteria on AgNP/PA6 films, respectively, after incubation for 24 h.

### **Sample characterization**

The absorption spectra of the prepared AgNP/PA6 NCs were recorded in FA immediately after their synthesis using a double-beam UV/Vis-NIR spectrophotometer (Varian Cary 5000 UV/Vis-NIR spectrometer). Quartz cuvettes were used for a precise UV-vis analysis in the range of 300 to 700 nm. DLS analysis was performed using a Malvern Zetasizer Nano ZS equipped with a vertically polarised He–Ne laser (633 nm) operating at 173° (Malvern Instruments, ZEN3600, UK). Before analysis, all samples were filtered immediately after their synthesis using 0.2 µm PTFE filters (ISOLAB), and glass cuvettes were utilized for accurate measurement. HRTEM was performed using a JEOL JEM-ARM200CFEG UHR-TEM equipped with an EDS detector. 2–3 drops of the freshly prepared NC solutions were used for the analysis. The Image J software was used to estimate the mean particle size. SEM analysis was performed using a Leo Supra 35VP, Germany, equipped with an EDS detector and operating at 10 kV. 2–3 drops of the freshly prepared NC solutions were cast on a piece of clean Si wafer for the analysis. The Image J software was used to estimate the distribution of AgNPs on the NC film surface. XRD was performed by a D2 Phaser diffractometer (Bruker, Billerica, Massachusetts, USA) using Cu K $\alpha$  radiation. The 2θ range and step size for this measurement were chosen as 5–90° and 0.01, respectively. The isolated NC powder after vacuum filtration was used for analysis. FTIR analysis of the samples was performed by a

Thermo Scientific Nicolet iS10, USA, equipped with a deuterated triglycine sulfate detector in the range of 4000–400 cm<sup>-1</sup>. The film of isolated NCs was prepared on cleaned glasses and used for FTIR measurement. The thicknesses of the films used for the antibacterial tests were measured by a J.A. Woollam Ellipsometer LAB. The solvent-casting technique was used to prepare films on 12 × 12 mm glass. In a typical procedure, 80 µL of NCs (2 mg mL<sup>-1</sup>) was loaded onto the glass substrate. Analysis was performed using an inductively coupled plasma optical emission spectrometer (ICP-OES, Varian, Australia). The AgNP/PA6 NC (10 mg) was heated in concentrated nitric acid (5 mL) using a single-mode MW system (Discover, CEM Microwave Technology Ltd) for 5 min at 200 °C. After complete dissolution, ultrapure deionized water was used to dilute it to 20 mL. Afterward, the prepared samples were filtered and used for analyses.

### 3.3 Results and Discussion

#### 3.3.1 Experimental Procedure

AgNP/PA6 NCs were prepared continuously using the MWFS described in **Figure 3-2**. The primary components of the MWFS are a MW heating source (2.45 GHz), a coiled-fluidic reactor (~8 mL), two infusion pumps, a thermocouple temperature probe, a pressurized gas source with a regulator (20 psi), a waste container, and a product container.

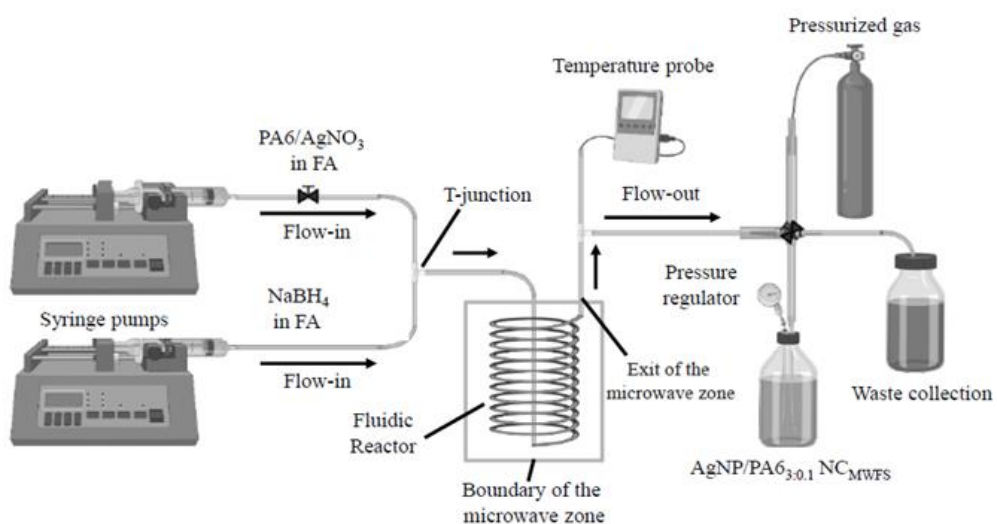


**Figure 3-2:** Graphical illustration of the MWFS for the continuous preparation of AgNP/PA6 NCs.

Selecting a suitable solvent is critically essential in the MWF manufacturing of AgNP/PA6 NCs. The primary criterion is that the solvent dissolves all of the precursors at RT. Amidic

solvents such as DMF are suitable for PA derivatives and AgNO<sub>3</sub>. In addition, these are medium MW absorbers; thus, the solvent temperature increase when exposed to MI is expected to be slow <sup>33</sup>. The solubility tests performed at RT for PA6 in DMF displayed low solubility (1.5 mg/mL). Time-dependent control experiments performed using a solution of AgNO<sub>3</sub> in DMF at RT revealed the formation of AgNPs with a UV-vis absorption band at 422 nm. This initial test indicated that DMF could act as nucleating/RAs to produce AgNPs. In contrast, the solubility of PA6 in FA, recognized as a green solvent <sup>17</sup>, at RT was 16 mg/mL, and no AgNP formation was observed in it at RT and its boiling point (100.8 °C). Therefore, a RA, NaBH<sub>4</sub>, was used to facilitate the nucleation of the NPs <sup>101–103</sup>. In typical experiments, the PA6/AgNO<sub>3</sub> (PA6= 0.8 g/AgNO<sub>3</sub>= 0.0005 M in 100 mL of FA) and RA (NaBH<sub>4</sub>=0.002 M in FA) solutions were prepared in different containers. Both solutions were infused independently, and they were mixed at the T-junction before reaching the MW zone. The resulting mixture (PA6, AgNO<sub>3</sub>, and NaBH<sub>4</sub>) was flown into the reactor at varying FRs and MWPs. Throughout the preparation of the AgNP/PA6 NCs, the optimized FR of 3 mL/min was kept constant for the NaBH<sub>4</sub> solution since precipitation occurred at the T-junction at higher FRs ( $\geq$ 4 mL/min). The NCs produced (66 samples) at various conditions (e.g. precursor concentration, MWP, and FR ratio) are given in **Table 3-1**.

**Table 3-1:** The list of NCs produced (66 samples) at various experimental conditions (e.g. reagent concentration, MWP, and FR ratio) and their UV-vis  $\lambda_{\text{max}}$ , and  $I_{\text{abs}}$  values.

NC	[PA6] in FA (g/100 mL)	MWP (W)	FR Ratio	$\lambda_{\max}$ (nm)	Labs	$\sim$ Size <sup>±</sup> (nm)	NC	[PA6] in FA (g/100 mL)	MWP (W)	FR Ratio	$\lambda_{\max}$ (nm)	Labs	$\sim$ Size <sup>±</sup> (nm)
MWF1	10	10	3:0.1	435	0.017	9.6	MWF34	0.8*	10	3:0.25	402	0.130	7.1
MWF2			3:0.25	422	0.031	6.5	MWF35			3:0.5	402	0.130	7.1
MWF3			3:0.5	418	0.058	2.5	MWF36			3:1	400	0.380	4.5
MWF4			3:1	409	0.120	1.8	MWF37			3:0.1	402	0.050	9.6
MWF5		20	3:0.1	403	0.029	4.1	MWF38			3:0.25	401	0.140	13.1
MWF6			3:0.25	403	0.061	7.1	MWF39			3:0.5	401	0.290	11.2
MWF7			3:0.5	402	0.064	5.9	MWF40			3:1	400	0.540	4.5
MWF8			3:1	400	0.150	3.9	MWF41			3:0.1	401	0.047	11.2
MWF9		30	3:0.1	404	0.029	67.8	MWF42			3:0.25	412	0.096	7.1
MWF10			3:0.25	402	0.155	69.1	MWF43			3:0.5	401	0.400	6.1
MWF11			3:0.5	402	0.280	58.9	MWF44			3:1	400	0.950	3.3
MWF12			3:1	400	0.570	51.1	MWF45			3:0.1	404	0.011	11.2
MWF13		40	3:0.1	404	0.230	50.9	MWF46			3:0.25	403	0.170	-
MWF14			3:0.25	403	0.450	50.9	MWF47			3:0.5	401	0.710	-
MWF15			3:0.5	402	0.490	37.4	MWF48			3:1	401	0.950	2.5
MWF16			3:1	402	0.790	37.4	MWF49			3:0.1	416	0.040	11.2
MWF17	10	10	3:0.1	403	0.039	9.6	MWF50	0.8*	10	3:0.25	401	0.070	9.6
MWF18			3:0.25	402	0.085	11.2	MWF51			3:0.5	401	0.150	8.3
MWF19			3:0.5	402	0.200	8.3	MWF52			3:1	398	0.350	9.6
MWF20			3:1	399	0.260	6.1	MWF53			3:0.1	404	0.130	8.3
MWF21		20	3:0.1	404	0.060	59.1	MWF54			3:0.25	402	0.270	6.1
MWF22			3:0.25	402	0.120	8.3	MWF55			3:0.5	401	0.490	4.5
MWF23			3:0.5	401	0.260	7.1	MWF56			3:1	398	0.570	2.5
MWF24			3:1	400	0.390	7.1	MWF57			3:0.1	417	0.030	7.1
MWF25		30	3:0.1	403	0.090	8.3	MWF58			3:0.25	403	0.110	8.3
MWF26			3:0.25	402	0.160	8.3	MWF59			3:0.5	402	0.580	9.6
MWF27			3:0.5	401	0.230	7.1	MWF60			3:1	399	0.800	8.3
MWF28			3:1	399	0.490	4.5	MWF61			3:0.1	412	0.097	20.5
MWF29		40	3:0.1	407	0.046	13.1	MWF62			3:0.25	403	0.200	9.6
MWF30			3:0.25	402	0.290	9.6	MWF63			3:0.5	402	0.590	6.1
MWF31			3:0.5	402	0.610	4.5	MWF64			3:1	400	0.970	2.8
MWF32			3:1	402	1.010	2.1	CHF1		50 °C	3:1	454	0.620	-
MWF33	0.4	10	3:0.1	403	0.110	7.1	CHF2		55 °C	3:1	460	0.580	45

The fluid temperature at the exit of the MW zone (~11 cm away from the MW zone) was recorded at 30 seconds intervals for 5 min. The temperature versus time graph given in **Figure 3-3** showed that the temperature of the reaction fluid exceeded the boiling point of FA (100.8 °C) at 50 W and reached *ca.*120 °C. Therefore, the MWP of 50 W was not used in the manufacturing process. In addition, at 40 W, the fluid temperature reached a plateau faster than that of 10, 20, and 30 W and remained unchanged. Thus, optimization experiments were carried out at 40 W.

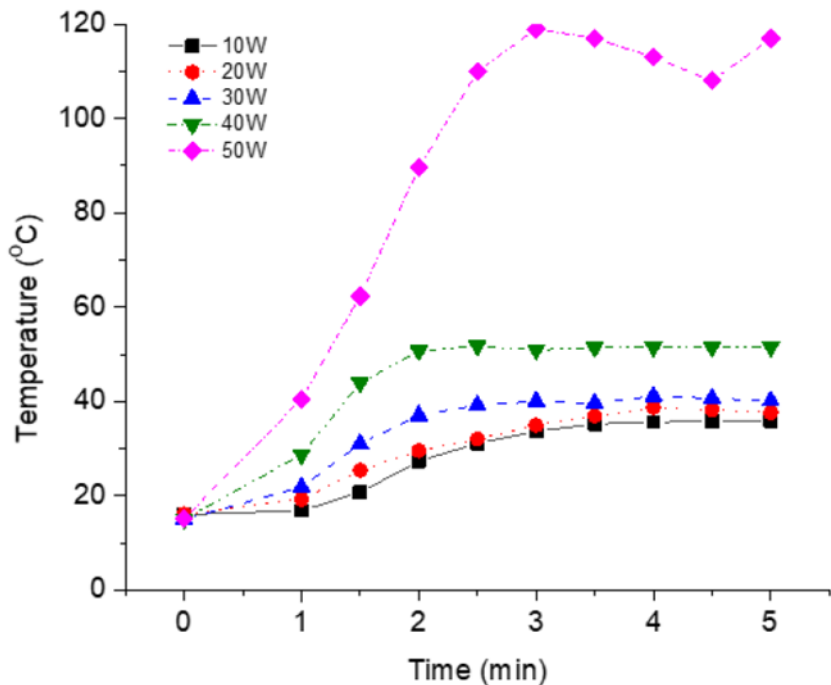


**Figure 3-3:** The MW power-dependent heating profile of the reaction fluid (PA6, AgNO<sub>3</sub>, and NaBH<sub>4</sub> solution in FA) in the MWFS under 20 psi constant pressure at the MWP of 10, 20, 30, 40, and 50 W. The temperature of the mixture was measured for 5 minutes at time intervals of 30 seconds.

It is also noteworthy that the measured temperature of the reaction fluid outside the MW zone (~11 cm) is expected to be lower than the fluid temperature at the exit of the MW zone due to the heat transfer to the surrounding area. The fluid temperature outside the MW heating zone can be estimated considering the forced convection heat transfer between the fluid inside the PTFE tubing and the surrounding air. The temperature values at the MW zone exit were calculated using Incropera and DeWitt's correlation<sup>104,105</sup>, and are given in the ESI **Table 3-2**. The overall calculations suggested that the exit temperature was ~4 °C higher than the measured temperatures.

**Table 3-2:** The estimated fluid temperatures outside the MW heating zone.

FR of NaBH <sub>4</sub> : FR of PA6/AgNO <sub>3</sub>	3:1					MW power=40 W		
MWP (W)	10	20	30	40	50	3:0.5	3:0.25	3:0.1
Measured temperature by	36	38	40	50	110	47	53	53

using a thermocouple (°C)								
Estimated exit temperature (°C)	39.87	41.87	43.87	53.87	113.87	50.87	56.87	56.87

### 3.3.2 Effect of MWP and FR ratio

The AgNP/PA6 NCs were produced at 10, 20, 30, and 40 W using the FR ratios ( $\text{NaBH}_4:\text{PA6}/\text{AgNO}_3$ ) of 3:1, 3:0.5, 3:0.25, and 3:0.1 (**Table 3-1**). It is noteworthy that decreasing FR of PA6/ $\text{AgNO}_3$  results in a decrease in the precursors' concentration in a unit volume under the flow conditions. The prepared NCs ( $\text{NC}_{\text{MWF}52}$ ,  $\text{NC}_{\text{MWF}56}$ ,  $\text{NC}_{\text{MWF}60}$ , and  $\text{NC}_{\text{MWF}64}$ ) were yellowish-to-orange in color (**Figure 3-4**).

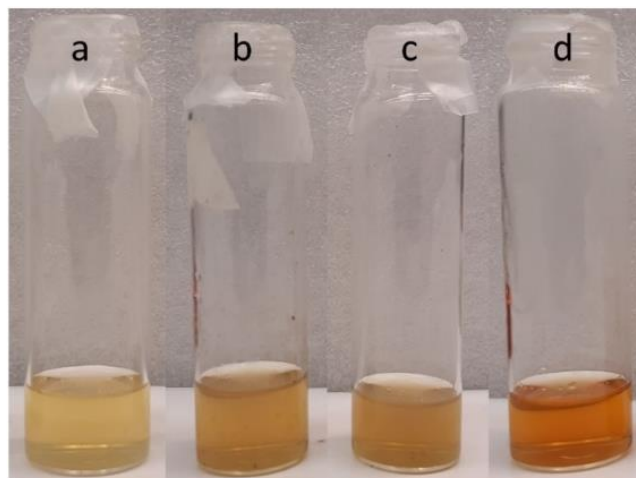


**Figure 3-4:** Color of the prepared AgNP/PA6 NC<sub>S<sub>MWF</sub></sub>s using MWPs of a) 10W, b) 20W, c) 30W, and d) 40W.

Freshly prepared NC solutions were characterized by UV-vis spectroscopy immediately after the synthesis (**Figure 3-5a-d** and **Figures 3-7, 3-8, and 3-9**). An absorption band at around 400 nm evidenced the formation of AgNPs in the PA6 matrix. The  $I_{\text{abs}}$  and the FWHM values were highly correlated with the applied MWP. An intense absorption band, attributable to the concentration of the formed AgNPs, was obtained at higher MWPs, and it was attributed to the MW-induced fast nucleation at higher MWP (**Figure 3-5a-b**). However, the same increasing trend in the  $I_{\text{abs}}$  was not observed at low FRs (0.25 and 0.1 mL/min for the PA6/ $\text{AgNO}_3$ ), probably due to the precursors' concentration in unit volume (**Figure 3-5c-d**). For a constant precursor concentration and FR ratio, the FWHM of  $\text{NC}_{\text{MWF}52}$  was significantly broader than that of  $\text{NC}_{\text{MWF}56}$ ,  $\text{NC}_{\text{MWF}60}$ , and  $\text{NC}_{\text{MWF}64}$ . Such broadenings are probably due to ineffective

particle nucleation at 10 W, and less intense absorption bands support it (**Figure 3-5, insets**). They are also characteristic of high-aspect-ratio particle formation<sup>106</sup>. The highest I<sub>abs</sub> with a moderately narrow FWHM is obtained for NC<sub>MWF64</sub> at 40W and FR ratio of 3:1 (**Figure 3-5a, inset**).

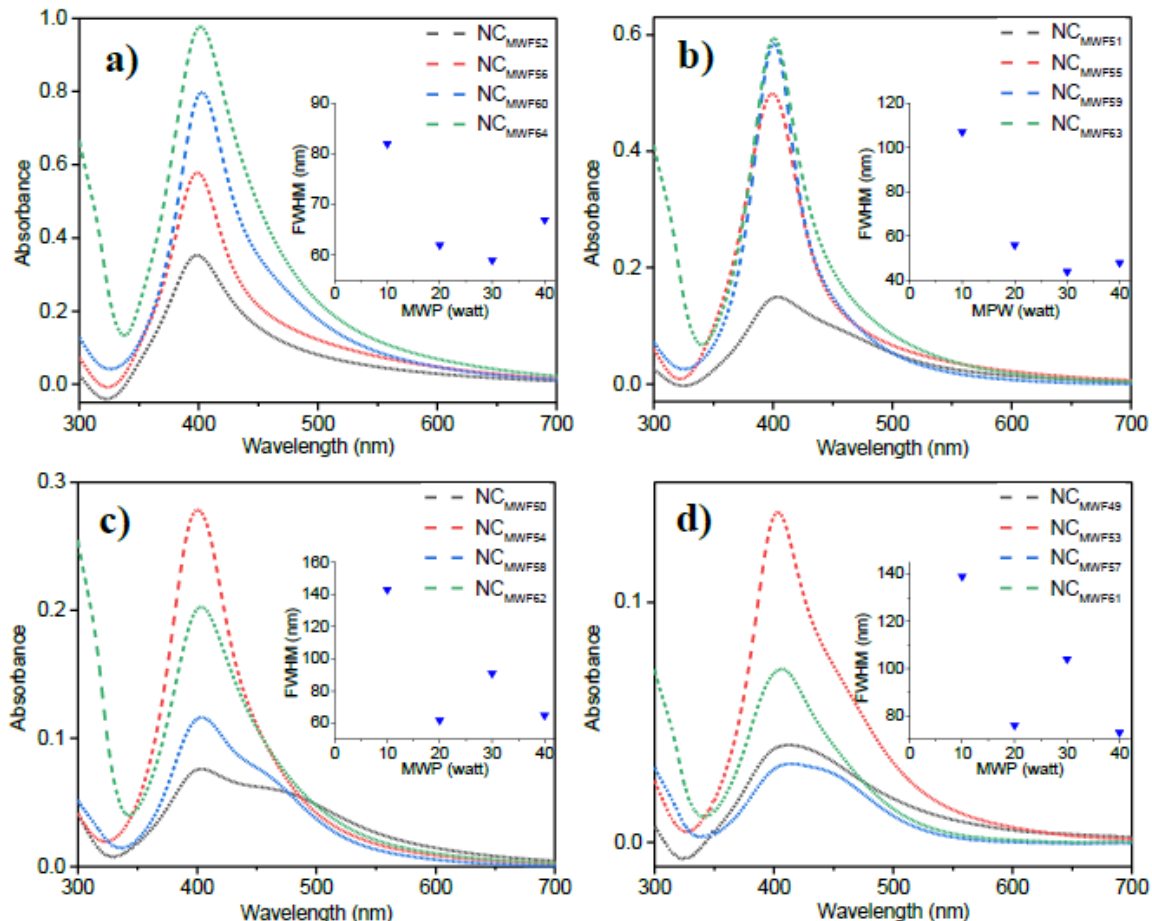


**Figure 3-5:** UV-Vis spectra of NCs prepared at MWPs of 10, 20, 30, and 40 W using the FR ratios (NaBH<sub>4</sub>:PA6/AgNO<sub>3</sub>) of a) 3:1, b) 3:0.5, c) 3:0.25, and d) 3:0.1. The insets of the figures show the FWHM versus MWP graphs.

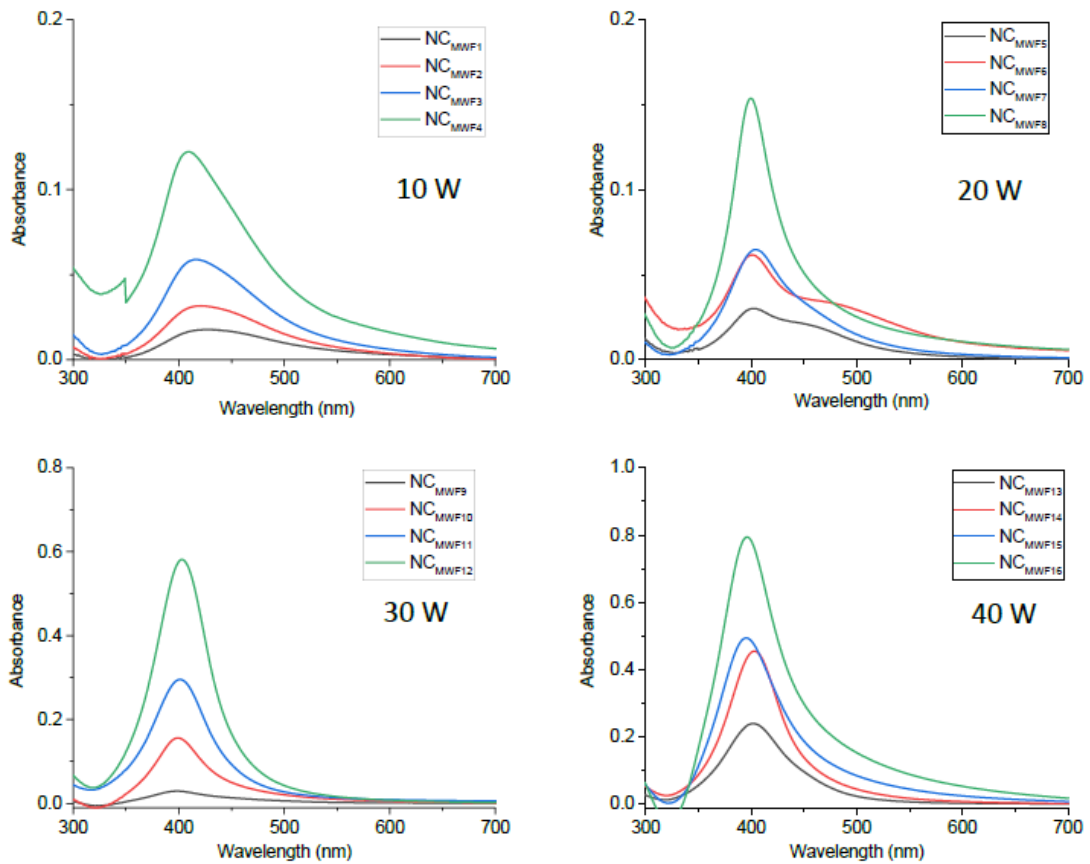


**Figure 3-6:** UV-vis spectra of NC<sub>MWF1-16</sub>.

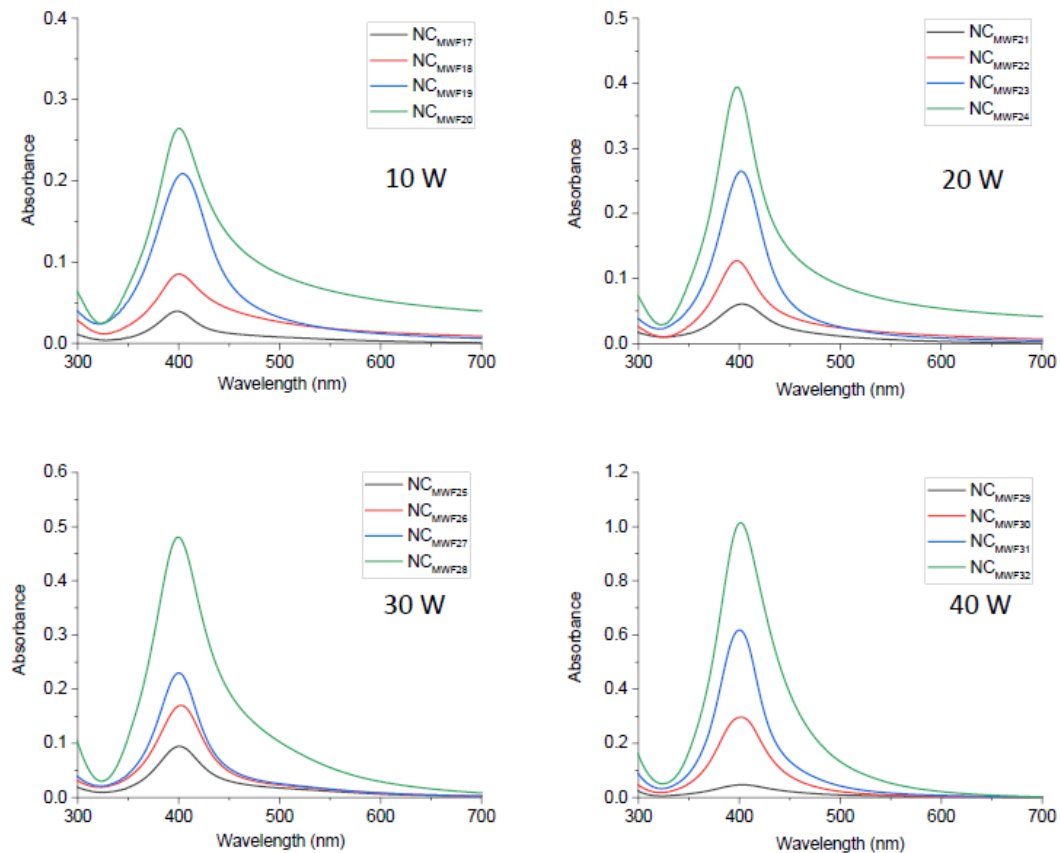


**Figure 3-7:** UV-vis spectra of NC<sub>MWF17-32</sub>.

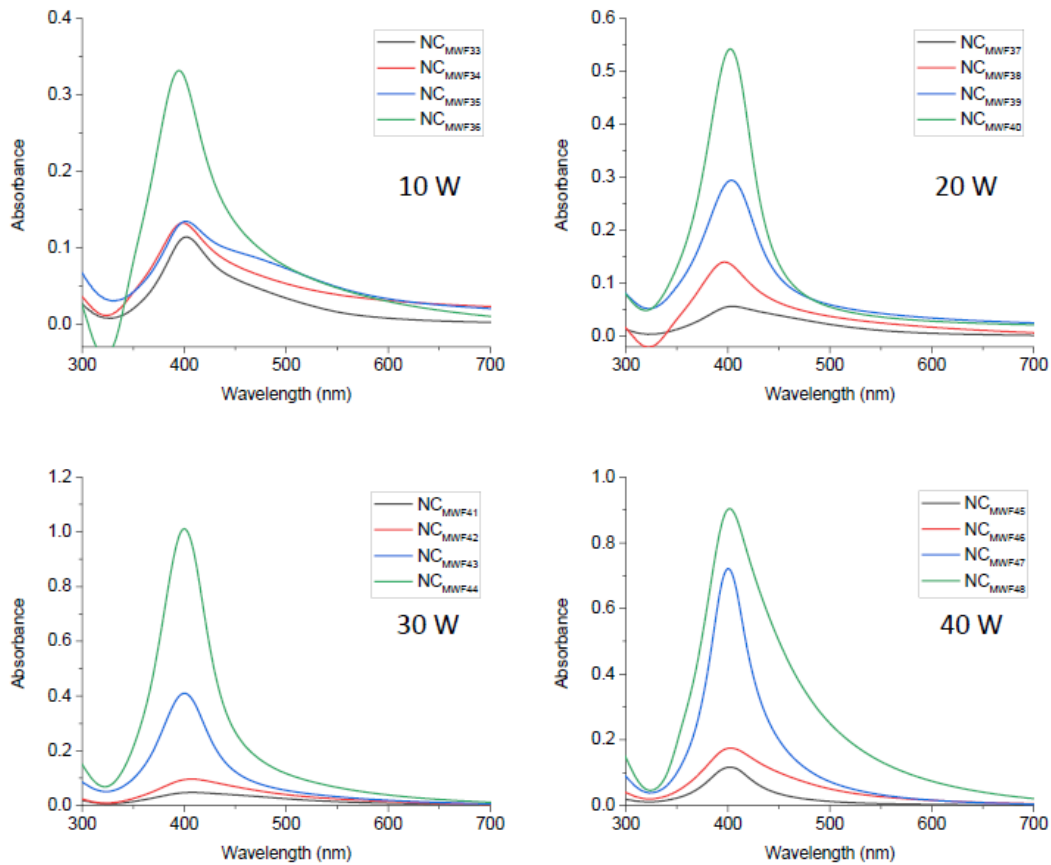


**Figure 3-8:** UV-vis spectra of NC<sub>MWF33-48</sub>.

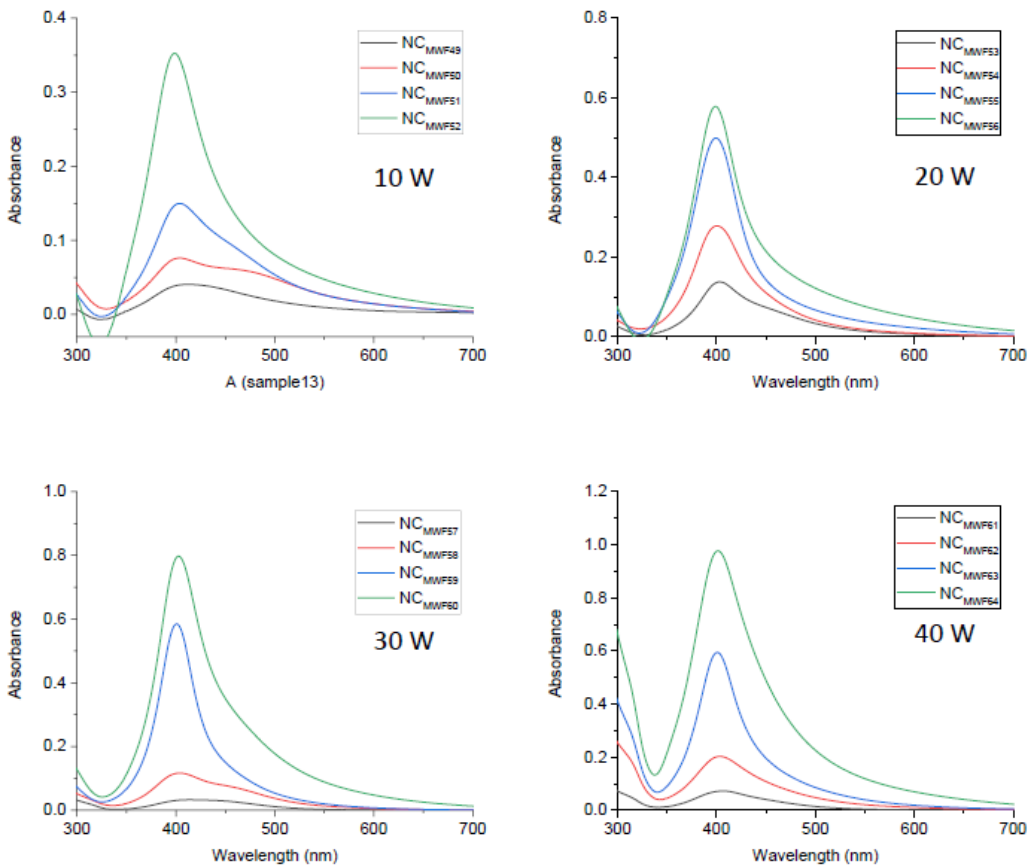


**Figure 3-9:** UV-vis spectra of NC<sub>MWF49-64</sub>.

Complementary to the UV-vis results, DLS, as an effective particle size determination method<sup>107,108</sup>, was employed to study the hydrodynamic size of the AgNPs in the PA6 matrix (**Figures 3-10, 3-11, 3-12, 3-13, and 3-14**). The hydrodynamic size of the AgNPs in NC<sub>MWF52</sub>, NC<sub>MWF56</sub>, and NC<sub>MWF60</sub> was ~10 nm, while the size in NC<sub>MWF64</sub> was ~3 nm. In contrast, the DLS analysis of the NCCHF<sub>2</sub> showed a hydrodynamic size of around 45 nm (**Figure 3-10**), indicating the advantage of the MWFS. In agreement with the previous studies, the observed superiority is believed to be due to the MW irradiation, which heats reagents fast and selectively and mitigates the temperature gradients<sup>109,110</sup>. Another essential phenomenon for MW heating is the rapid cooling of the synthesized products, which restricts further particle growth and aggregate formation<sup>110</sup>. In addition, more seed formation is expected at faster temperature ramping rates, facilitating nucleation instead of particle growth; thus, smaller particle formation could be achieved at high MWPs<sup>96</sup>. Therefore producing smaller AgNPs at 40 W compared to 10 W can be attributed to more effective seed formation. However, one should also take into account the effect of polymer. It is known that polymers act as stabilizers for MNPs and the number of functional groups is a dominating factor in stabilizing NPs<sup>111</sup>. For example, a previous study showed the formation of smaller AuNPs (~1.5 nm) at a high concentration of

thiol-terminated poly(ethylene glycol) monomethyl ethers compared to large NPs ( $\sim 3.19$  nm) at a low polymer concentration<sup>112</sup>. Similarly, in our experiments, small AgNP formation was observed when the concentration of PA6 increased. Therefore, the AgNP formation in the MWFS is probably MWP-dependent and PA6 concentration-dependent process, and the control of both parameters is highly crucial to produce AgNPs in the PA6 matrix with desired particle size and distribution. Furthermore, a scaling-up experiment performed using a 5-fold excess of PA6 under the same experimental conditions of NC<sub>MWF64</sub> produced  $\sim 5$  nm AgNPs displaying a  $\lambda_{\text{max}}$  at *ca.* 402 nm, suggesting possible process scalability (**Figure 3-15**).

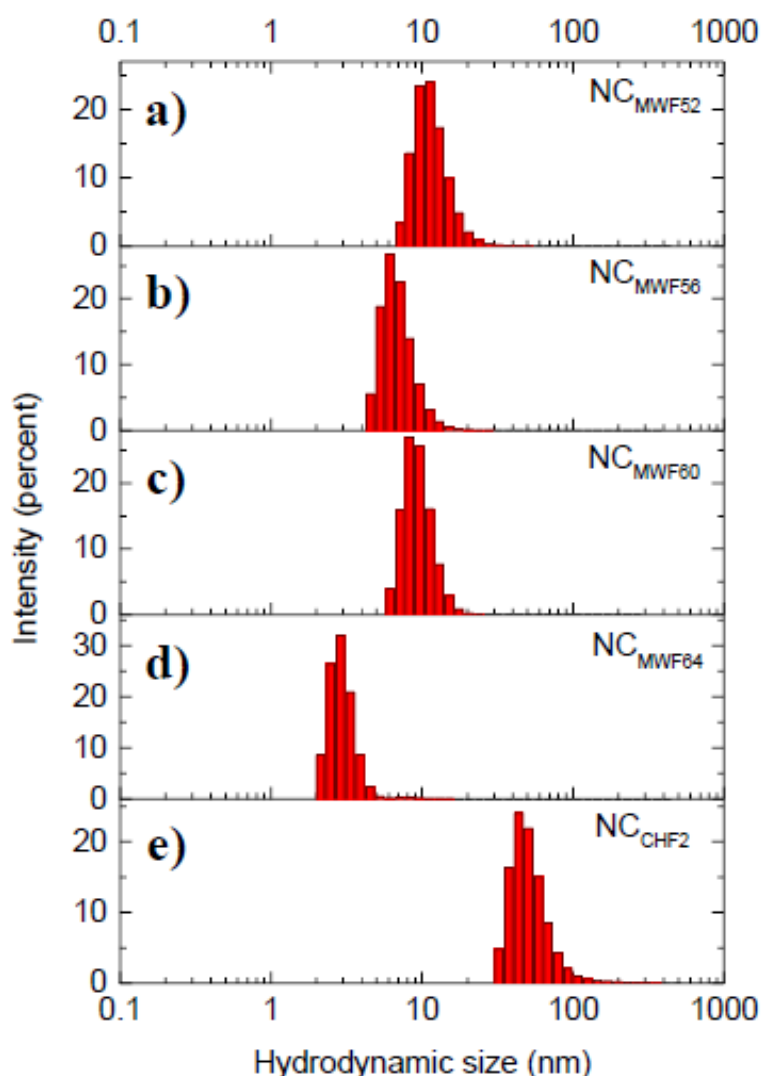


**Figure 3-10:** Hydrodynamic size distribution of the prepared NCs. a) NC<sub>MWF52</sub>, b) NC<sub>MWF56</sub>, c) NC<sub>MWF60</sub>, d) NC<sub>MWF64</sub>, and NC<sub>CHF2</sub>.

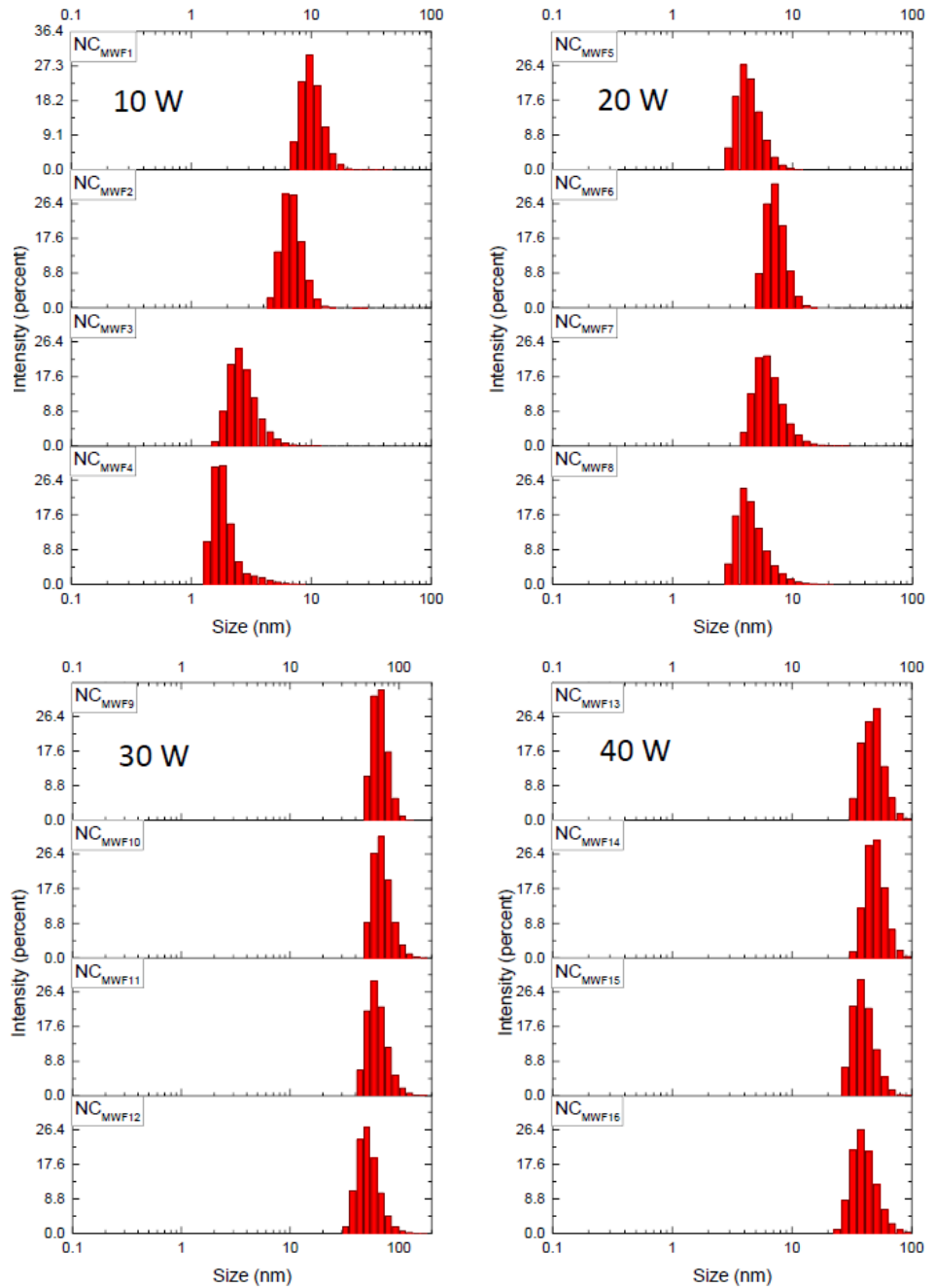


**Figure 3-11:** Hydrodynamic size distribution of NC<sub>MWF1-16</sub>.

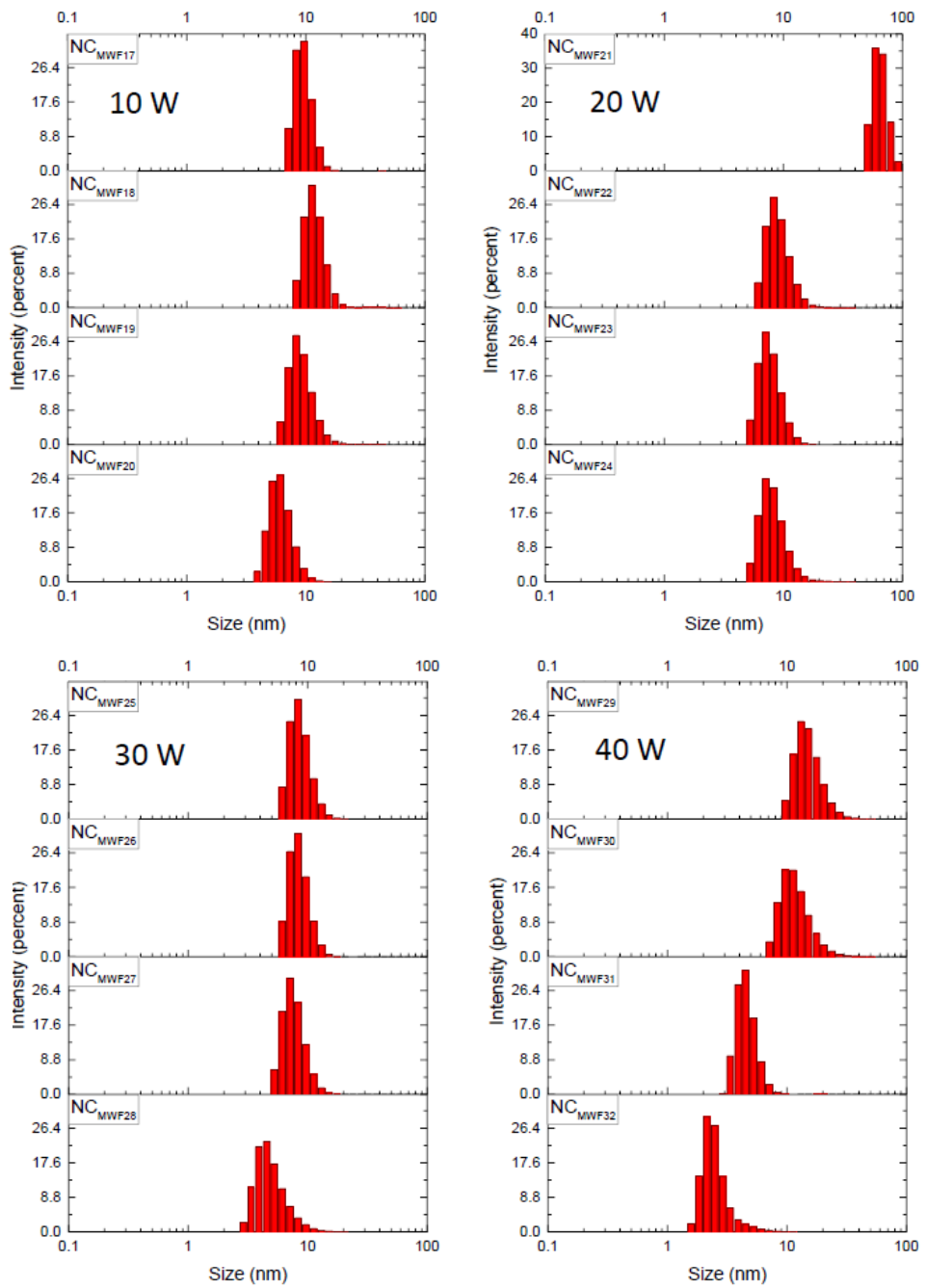


**Figure 3-12:** Hydrodynamic size distribution of NC<sub>MWF17-32</sub>.

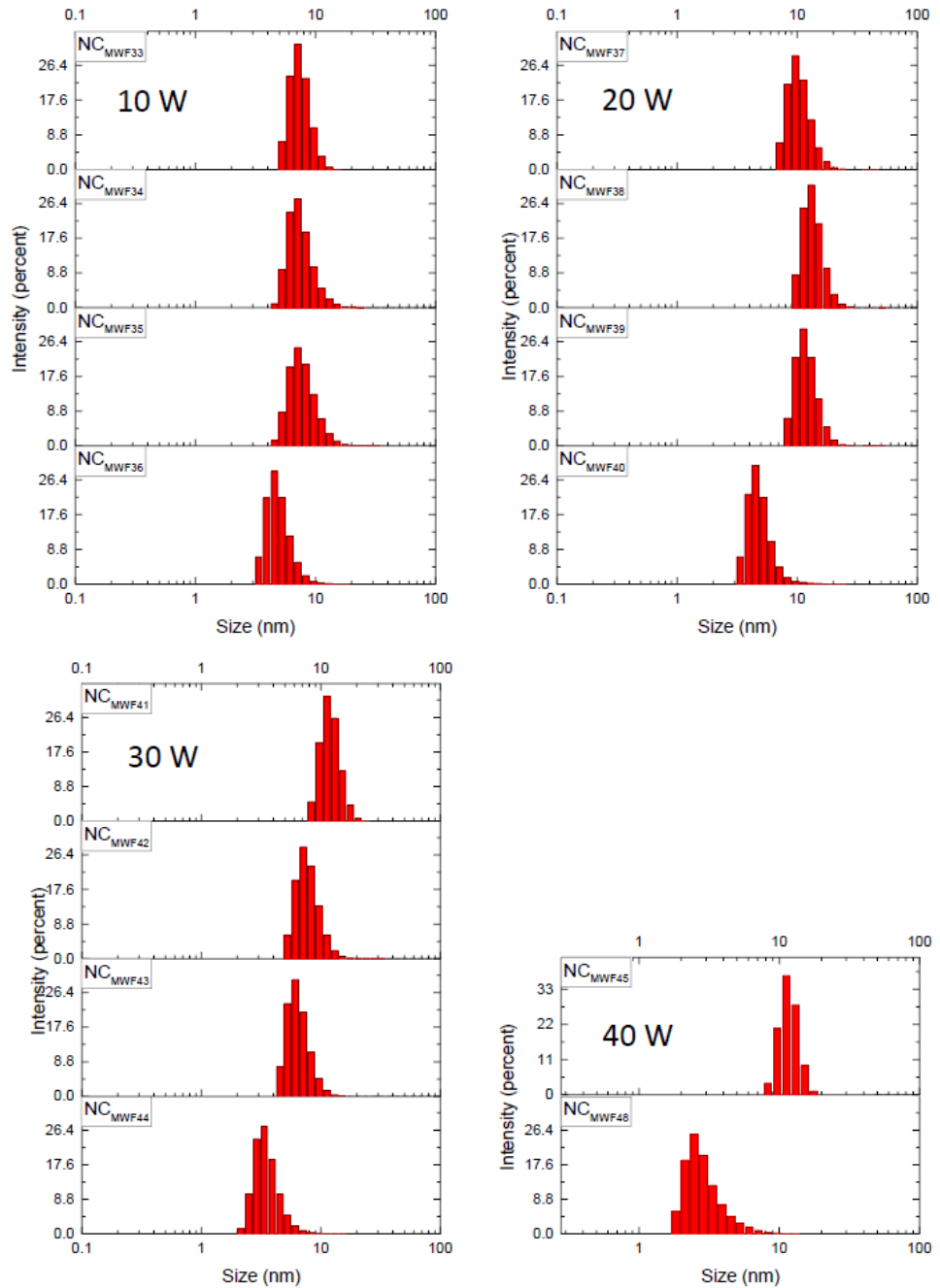


**Figure 3-13:** Hydrodynamic size distribution of NC<sub>MWF</sub>33-45 and NC<sub>MWF</sub>48.

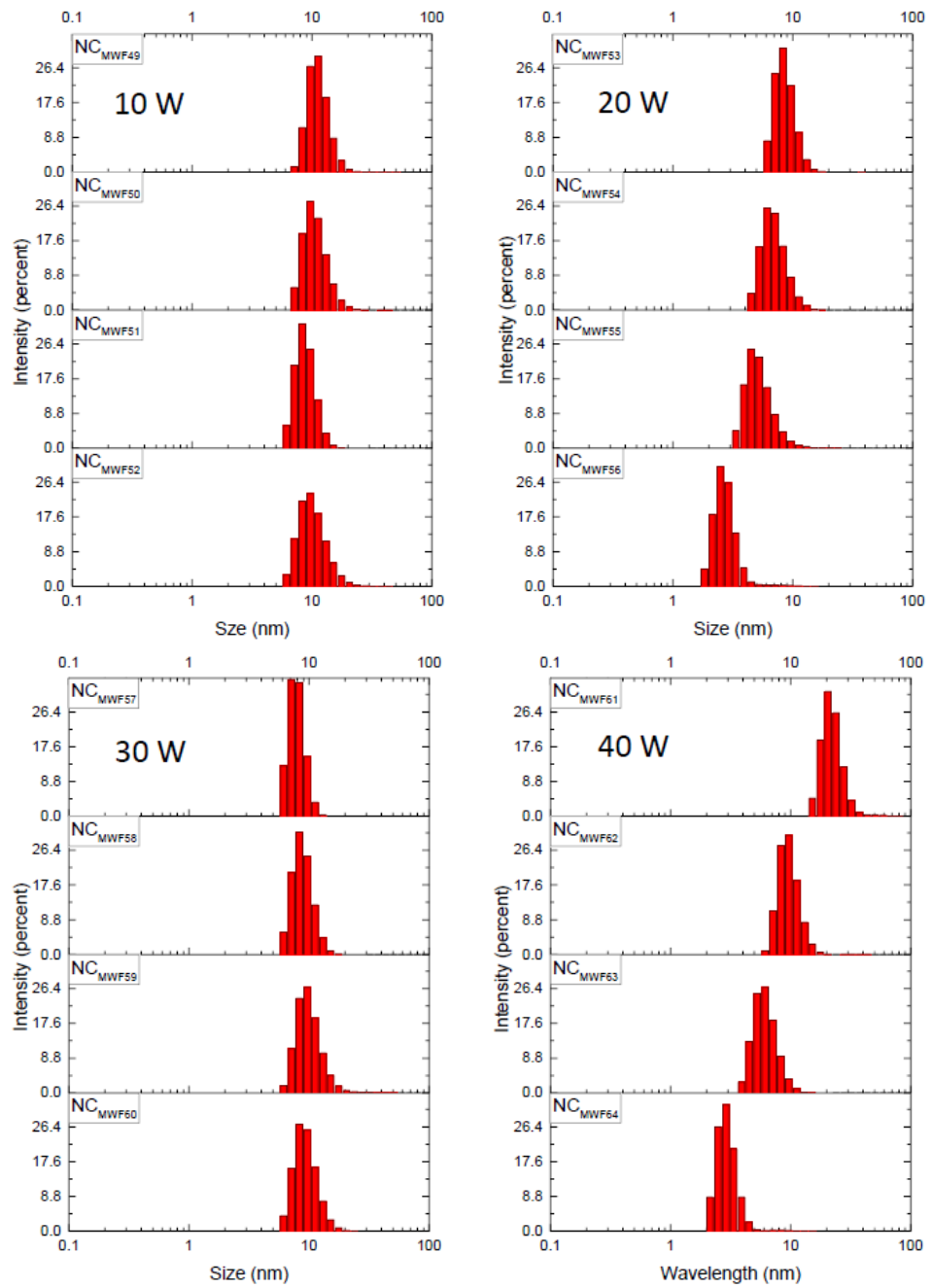


**Figure 3-14:** Hydrodynamic size distribution of NC<sub>MWF</sub>49-64.

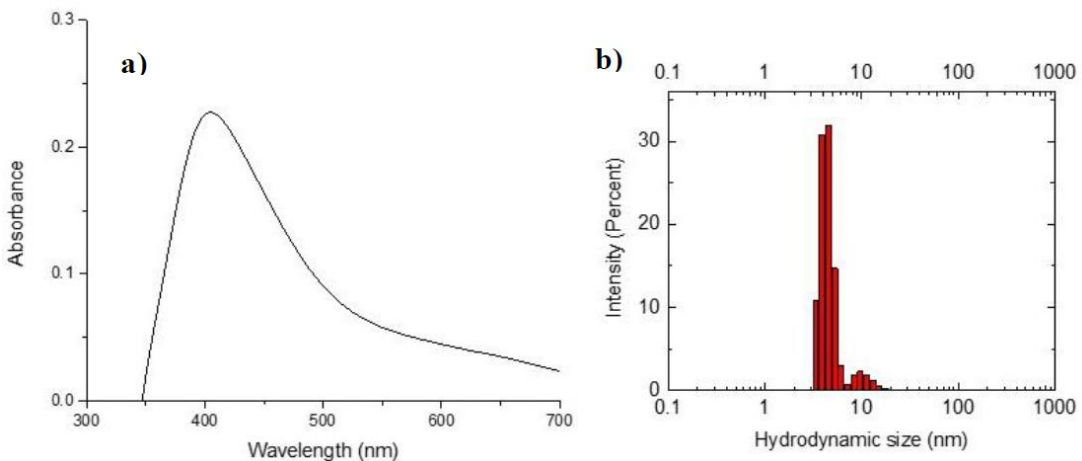


**Figure 3-15:** a) UV-vis spectrum and b) hydrodynamic size distribution of AgNP/PA6 NC prepared using a 5-fold excess of PA6 under the same experimental conditions of NC<sub>MWF64</sub>.

### 3.3.3 Effect of Reagent (PA6, AgNO<sub>3</sub>, and NaBH<sub>4</sub>) Concentration and FR Ratio.

The impact of reagent concentration and the FR ratio on the properties of the NCs was examined at 40 W. The UV-vis spectra of the NCs (NC<sub>MWF13-16</sub>, NC<sub>MWF29-32</sub>, NC<sub>MWF45-48</sub>, and NC<sub>MWF61-64</sub>) are given as **Figures 3-7, 3-8**, and **3-9**. For comparison, the final concentrations of PA6 at different FR ratios were plotted against the  $\lambda_{\text{max}}$  values corresponding to the final concentrations of AgNO<sub>3</sub> and NaBH<sub>4</sub> (**Figure 3-16**). It is worth noting that the final concentrations of the reagents are dependent on the change in the FR ratios. NC<sub>MWF64</sub> displayed the lowest  $\lambda_{\text{max}}$ , at ~400 nm, suggesting the formation of smaller NPs (~3 nm by DLS) at high polymer concentrations <sup>113,114</sup>. The hydrodynamic size of AgNPs for NC<sub>MWF61</sub> was ~20 nm (**Figure 3-14**). The results revealed the critical role of the polymer concentration while preparing the NCs in the MWFS. In addition, the  $\lambda_{\text{max}}$  values of NC<sub>MWF16</sub>, NC<sub>MWF32</sub>, and NC<sub>MWF48</sub> (402, 401, and 401 nm, respectively) were comparable with NC<sub>MWF64</sub> (**Figures 3-6, 3-7, and 3-8**). However, DLS results displayed ~2-3 nm AgNPs for NC<sub>MWF32</sub> and NC<sub>MWF48</sub>, and ~40 nm for NC<sub>MWF16</sub>, further suggesting the effect of PA6 concentration (**Table 3-1** and **Figures 3-11, 3-12, and 3-13**). Effectively manipulating the particle size was attributed to an efficient *in-situ* stabilization of the generated small AgNPs via the amide functional groups on PA6 chains. The full UV-vis spectra and DLS results for the prepared NCs are presented in **Figures 3-6, 3-7, 3-8, 3-9**, and **Figures 3-11, 3-12, 3-13**, and **3-14**, respectively. Optimized experimental parameters revealed that the NCs with narrowly distributed ~3 nm AgNPs (NC<sub>MWF64</sub>) could be manufactured continuously in the MWFS when the final concentration of PA6, AgNO<sub>3</sub>, and NaBH<sub>4</sub> was set to 2 mg/mL,  $12.5 \times 10^{-5}$  mmol/mL, and  $1.5 \times 10^{-3}$  mmol/mL, respectively, at the FR of 3:1.

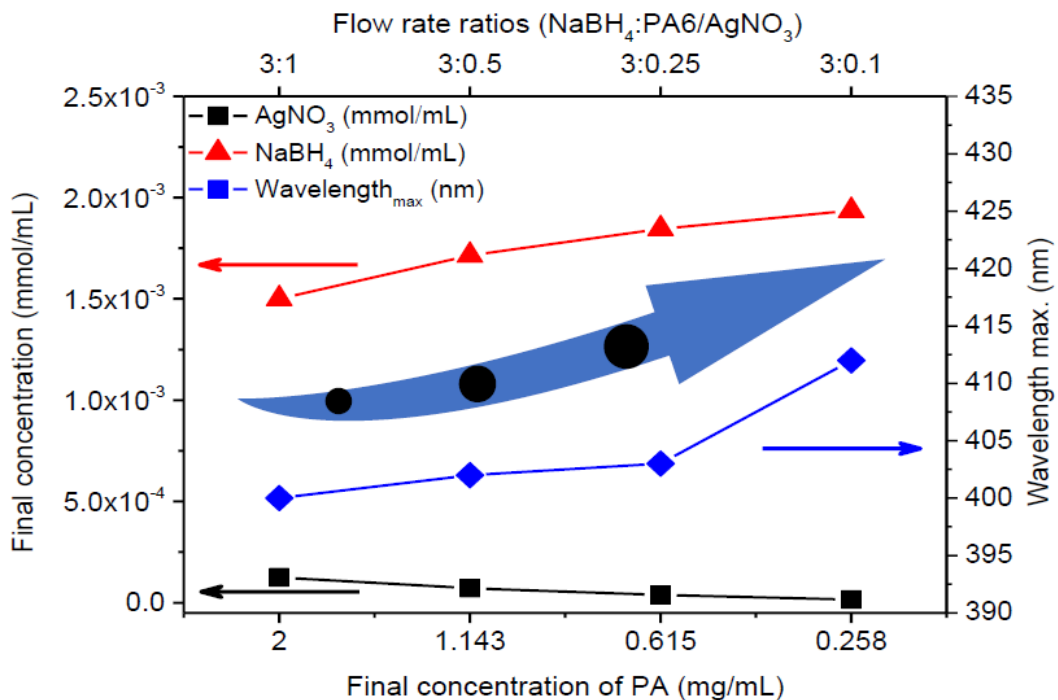


**Figure 3-16:** Reagent (PA6, AgNO<sub>3</sub>, and NaBH<sub>4</sub>) concentration-dependent change in the  $\lambda_{\text{max}}$  values of the prepared NCs at 40 W and varying FR ratios (3:1, 3:0.5, 3:0.25, and 3:0.1) The arrow shows the change in the particle size.

NC<sub>MWF64</sub> and NC<sub>MWF32</sub> were further characterized by HRTEM to evaluate the effect of PA6 concentration on the size and distribution of AgNPs. TEM analysis of NC<sub>MWF64</sub> revealed that the produced spherical AgNPs were distributed homogeneously in the PA6 matrix (**Figure 3-17a-b**). The mean particle size of AgNPs (Number of counted AgNPs=370) in NC<sub>MWF64</sub> was  $2.59 \pm 0.64$  nm, and the results were in close agreement with the data obtained by the DLS analysis ( $\sim 3$  nm) (**Figure 3-17a, inset**). The HRTEM image of the AgNPs showed the lattice fringes of 0.23, 0.20, and, 0.15 nm, attributed to the lattice planes of [111], [200], and [220], respectively (**Figure 3-17c**). TEM image of NC<sub>MWF32</sub> prepared using low PA6 concentration displayed bigger AgNPs with a mean particle size of  $8.19 \pm 3.85$  nm, further stressing the effect of polymer concentration under the same MW flow conditions (**Figure 3-18**).

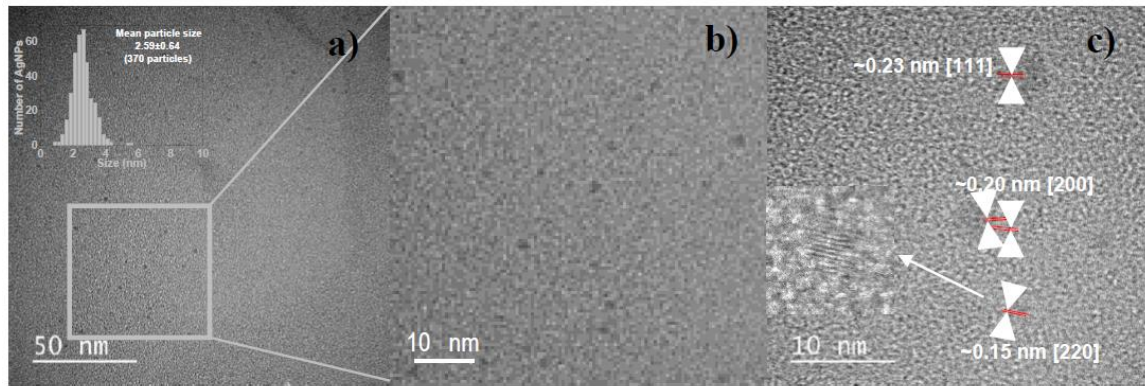


**Figure 3-17:** a) TEM image of the AgNPs in NC<sub>MWF64</sub>. Inset shows the mean particle size distribution of the AgNPs. b) The enlarged TEM image of the AgNPs. c) HRTEM image of the spherical AgNPs in NC<sub>MWF64</sub>. Two parallel red lines show the lattice fringes of AgNPs. Inset shows the expanded image of AgNP having [220] lattice plane.

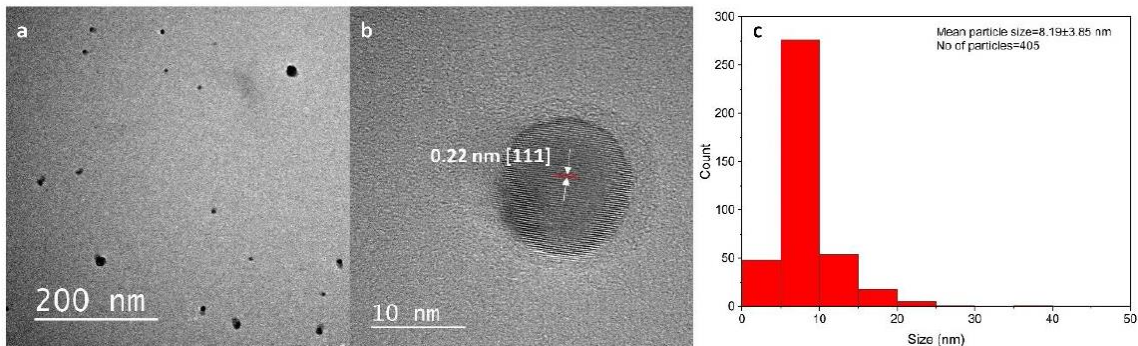


**Figure 3-18:** a) TEM image of the prepared NC<sub>MWF32</sub>. a) HRTEM image of AgNPs embedded in the matrix of PA6. Red parallel lines exhibit the lattice fringe of AgNPs. The measured distance of 0.22 nm corresponds to [111] lattice plane c) The particle size distribution related to produced AgNPs.

### 3.3.4 The microwave-fluidic (MWF) system versus the conventional heating fluidic (CHF) system

Except for the heating source, experimental conditions were kept constant while preparing the NC<sub>MWF64</sub> in the CHFS. Instead of MW heating, a conventional oil bath was used as the heating source. The synthesis was performed at 50 and 55 °C. The prepared NC was isolated and labeled as the NC<sub>CHF1</sub> and NC<sub>CHF2</sub> for 50 °C and 55 °C, respectively. The UV-vis spectra of the NC<sub>CHF</sub> displayed a broad absorption band at *ca.* 460 with an FWHM of 178 nm (**Figure 3-19**) compared to NC<sub>MWF</sub>, indicative of large particle formation. In accordance with the DLS results (**Figure 3-10e**), the NC<sub>CHF2</sub> (**Figure 3-20**) TEM analysis showed the particles in the range of 35 to 100 nm in size compared to ~3 nm NPs for NC<sub>MWF64</sub> (see **Figure 3-17a**). These results

indicated that MW irradiation provided a homogeneous and uniform energy supply and controlled the nucleation of NPs.

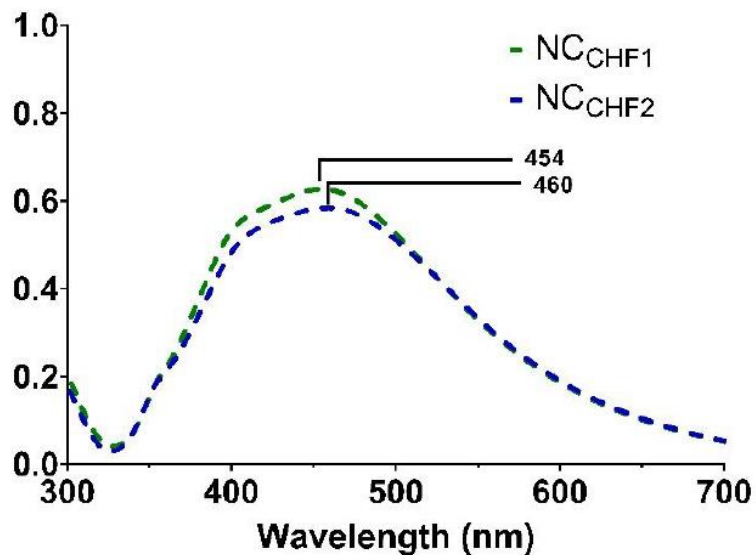


**Figure 3-19:** UV-Vis spectra of the prepared NCs using the NaBH<sub>4</sub>:PA6/AgNO<sub>3</sub> FR ratios of 3:1 in the CHFS at 50 °C (NC<sub>CHF1</sub>) and 55 °C (NC<sub>CHF2</sub>).

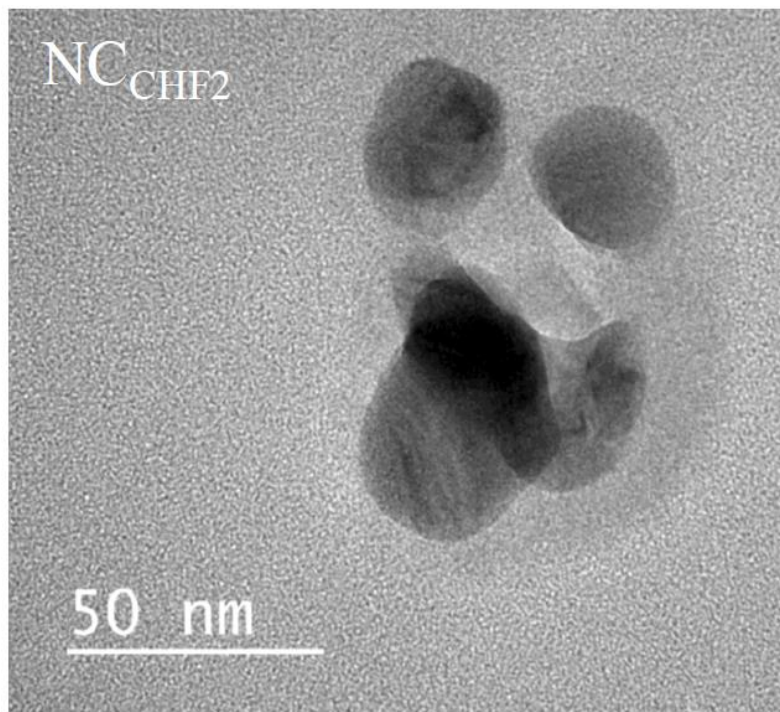


**Figure 3-20:** TEM image of the AgNPs in NC<sub>CHF2</sub>.

The crystallinity and phase purity of the prepared bulk NCs were studied by powder XRD. The XRD patterns are given in **Figure 3-21a**. As-received PA6 displayed two sharp Bragg reflections positioned at 20.48° [200] and 23.98° [002], characteristic of  $\alpha$ -phase PA6

(monoclinic crystal)<sup>115</sup>. The peaks were in agreement with JCPDS Card Number 022-0700. After composite preparation, there was a dominating diffraction peak at 21.66° [020], 21.88° [020], and 21.39° [020] in the analyzed NC<sub>MWF64</sub>, NC<sub>MWF60</sub>, and NC<sub>CHF2</sub>, respectively, which are characteristic of  $\gamma$ -phase PA6 (pseudo-hexagonal crystal)<sup>115</sup>. The diffraction peak at ~11.09° [001] was also associated with  $\gamma$ -phase PA6. On the other hand, the  $\gamma$ -phase formation, attributed to adequate hydrogen bonding in a parallel chain arrangement<sup>116</sup>, was more noticeable in NC<sub>MWF64</sub>, probably due to the small size of AgNPs. In addition, there was still an  $\alpha$ -phase in the prepared NCs.

The presence of metallic Ag is characterized by four unique diffraction peaks positioned at *ca.* 39°, 43°, 65°, and 77°<sup>117,118</sup>. These peaks are related to the face-centered cubic structures of Ag (JCPDS Card Number 87-0597). The XRD pattern of NC<sub>MWF64</sub> showed broad and weak Bragg reflections at 43.59°, 64.81°, and 77.39°, attributed to [200], [220], and [311] lattice planes, suggesting the presence of small crystallites<sup>119</sup>. The peak corresponding to the [111] lattice plane was not distinguished due to the overlapping PA6 peaks. Furthermore, there was no oxidized Ag peak, indicating adequate stabilization/protection by PA6 chains. Therefore, higher antimicrobial activities may be envisaged from the non-oxidized AgNPs. In addition, slightly more intense diffraction peaks were observed for NC<sub>MWF60</sub> at 44.54 [200], 64.78 [220], and 77.73° [311]. In contrast, the XRD pattern of NC<sub>CHF2</sub> displayed a strong signal at 43.53° [200] and two less intense but sharp peaks at 63.81° [220] and 76.97° [311], indicating large AgNPs.

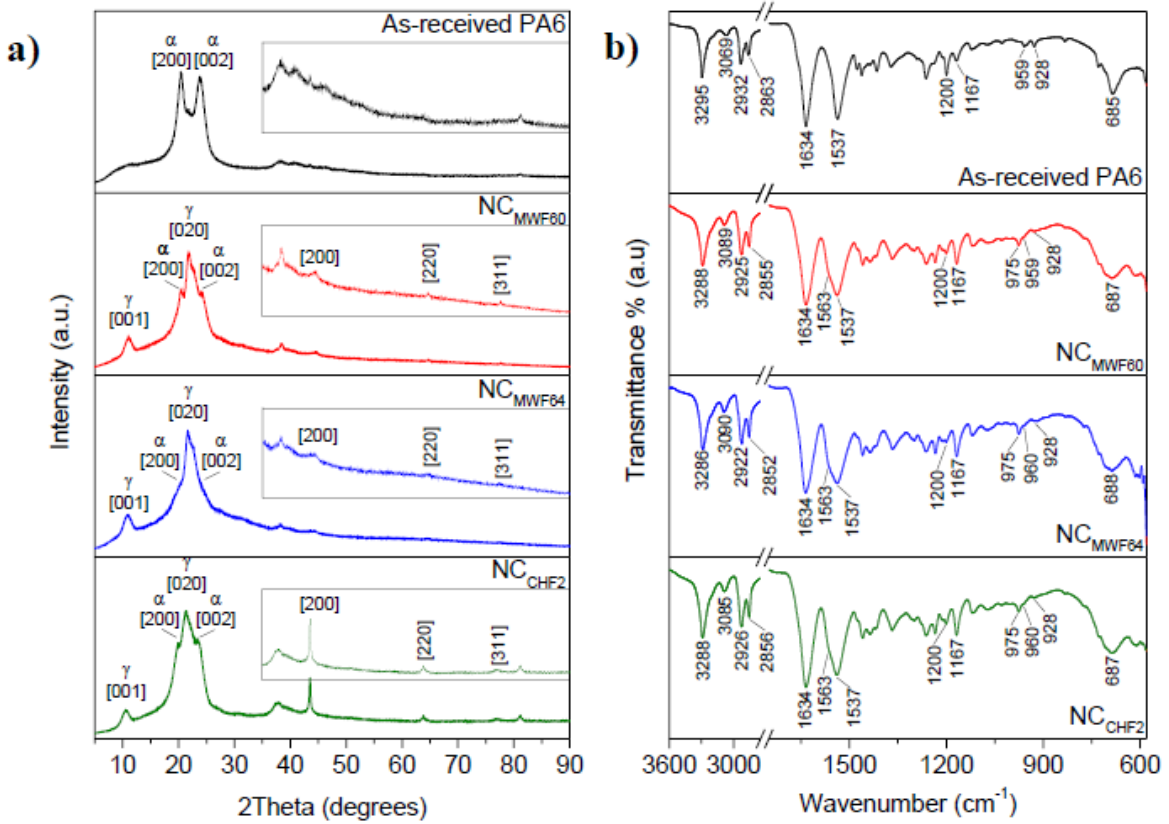


**Figure 3-21:** a) XRD patterns and b) FTIR spectra of the as-received PA6, NC<sub>MWF60</sub>, NC<sub>MWF64</sub>, and NC<sub>CHF2</sub>

FTIR was employed to assess the change in the IR active modes in the PA6 backbone (**Figure 3-21b)** after AgNP incorporation. FTIR spectrum of the as-received PA6 displayed characteristic bending vibration of the amide carbonyl (-N-C=O) at around  $1634\text{ cm}^{-1}$ <sup>120</sup>. The peaks located at  $3295$  and  $1537\text{ cm}^{-1}$  were assigned to the stretching and bending vibration of the hydrogen bonds (H-N-), and the ones at  $2932\text{ cm}^{-1}$  and  $2863\text{ cm}^{-1}$  were for to C-H bond<sup>115,120</sup>. In addition, there was a medium band at *ca.*  $3069\text{ cm}^{-1}$ , related to the intramolecular bond between amide and carbonyl groups ( $-\text{CONH}_2$ )<sup>120</sup>. After AgNP formation in the PA6 matrix, the peaks at  $3295$ ,  $2932$ , and  $2863$  observed in PA6 shifted to the low energy region by  $\sim 7\text{ cm}^{-1}$ . In contrast, there was a positional shift in the peak at  $3069\text{ cm}^{-1}$  to a higher wavenumber ( $\sim 3089\text{ cm}^{-1}$ ). No change was observed in the peak positions at  $1634$  and  $1537\text{ cm}^{-1}$ ; however, a shoulder appeared at  $1563\text{ cm}^{-1}$ . A significant decrease in the intensity of the bands positioned at  $685$  and  $1200\text{ cm}^{-1}$  was recorded in the presence of AgNPs. In contrast, there was an increase in the peak's intensity at *ca.*  $1167\text{ cm}^{-1}$  after AgNP formation. Furthermore, a new peak formation was observed at  $975\text{ cm}^{-1}$  while the weak band at  $928\text{ cm}^{-1}$ , which corresponded to an  $\alpha$ -crystalline PA6 phase, was suppressing. The observed suppression was in agreement with the presence of  $\alpha$ -phase PA6 confirmed by XRD analysis

<sup>115,120</sup>. On the other hand, there was no apparent size-dependent change in the FTIR spectra of NC<sub>MWF64</sub>, NC<sub>CHF2</sub>, and NC<sub>MWF60</sub>, except a slightly less intense peak at 1200 cm<sup>-1</sup> in the spectrum of NC<sub>MWF64</sub>.

Given the significant AgNP size difference in the prepared composites of NC<sub>CHF2</sub> (particle size ~50nm) and NC<sub>MWF64</sub> (particle size ~3 nm), the antibacterial activities are expected to correlate with the size of AgNPs <sup>121</sup>. In addition, the amount of AgNPs in the prepared NCs is critical while evaluating the antibacterial effectiveness. The ICP-OES analysis of NC<sub>MWF64</sub> and NC<sub>CHF2</sub> showed the presence of 0.63 and 0.66% (w/w) AgNPs, respectively.

The antibacterial activity of the as-received PA6, NC<sub>CHF2</sub>, and NC<sub>MWF64</sub> films prepared on glass slides were evaluated against *Escherichia coli* (Gram-negative), *Staphylococcus aureus* (Gram-positive), and *Pseudomonas aeruginosa* (Gram-negative). Comparable film thicknesses were ensured using an ellipsometer showing 118.38, 122.67, and 118.92 nm for the as-received PA6, NC<sub>CHF2</sub>, and NC<sub>MWF64</sub>. A glance at **Table 3-3** reveals that the number of viable bacteria decreased considerably after being incubated for 24 h, especially in the case of the NC<sub>MWF64</sub> film exhibiting an activity above 98%.

**Table 3-3:** Antibacterial rate of PA6, NC<sub>CHF2</sub>, and NC<sub>MWF64</sub> films against *Escherichia coli*, *Pseudomonas aeruginosa*, and *Staphylococcus aureus*

	<i>Escherichia coli</i> (Gram-negative)	<i>Staphylococcus aureus</i> (Gram-positive)	<i>Pseudomonas aeruginosa</i> (Gram-negative)
PA6 coated glass	~47.70%	~7.00%	~1.00%
NC <sub>CHF2</sub> coated glass	~80.50%	~83.70%	~76.40%
NC <sub>MWF64</sub> coated glass	~98.11%	~98.91%	~98.03%

Despite the growth of *Escherichia coli*, *Staphylococcus aureus*, and *Pseudomonas aeruginosa* on both NC films, a remarkable reduction in CFU of bacteria was noticed for NC<sub>MWF64</sub>, indicating that the small AgNPs exhibit greater antibacterial effect (**Figure 3-22**). The observed size dependency was in close agreement with a recent study discussing the AgNP size effect on the inhibition of fungi and bacteria <sup>121</sup>.

A plausible reason for the more effective antibacterial rate (%) of NC<sub>MWF64</sub> can be related to the enhanced attraction between the small Ag ion and the negatively charged cytomembrane, which is due to coulomb force leading to the attachment of the bacterium on the surface of the film. Ag ion penetration into the bacterial cell hinders cell synthase activity and subsequently that of the respiratory and transfer systems of the cell. As a result, the division feature of the cell stops, and the cell dies <sup>122</sup>. With a similar mechanism, Ag ions are released from NCs which damage various parts of the bacteria such as the cell wall, and lead to bacterial death <sup>123</sup>, and the release rate is probably higher for NC<sub>MWF64</sub> containing small NPs. In addition, the crystallinity of PA6 might affect the release rate of Ag ions <sup>124</sup>. Considering that the  $\gamma$  phase PA6 dominates in NC<sub>MWF64</sub>, the  $\gamma$ -crystalline structure facilitates Ag ion release.

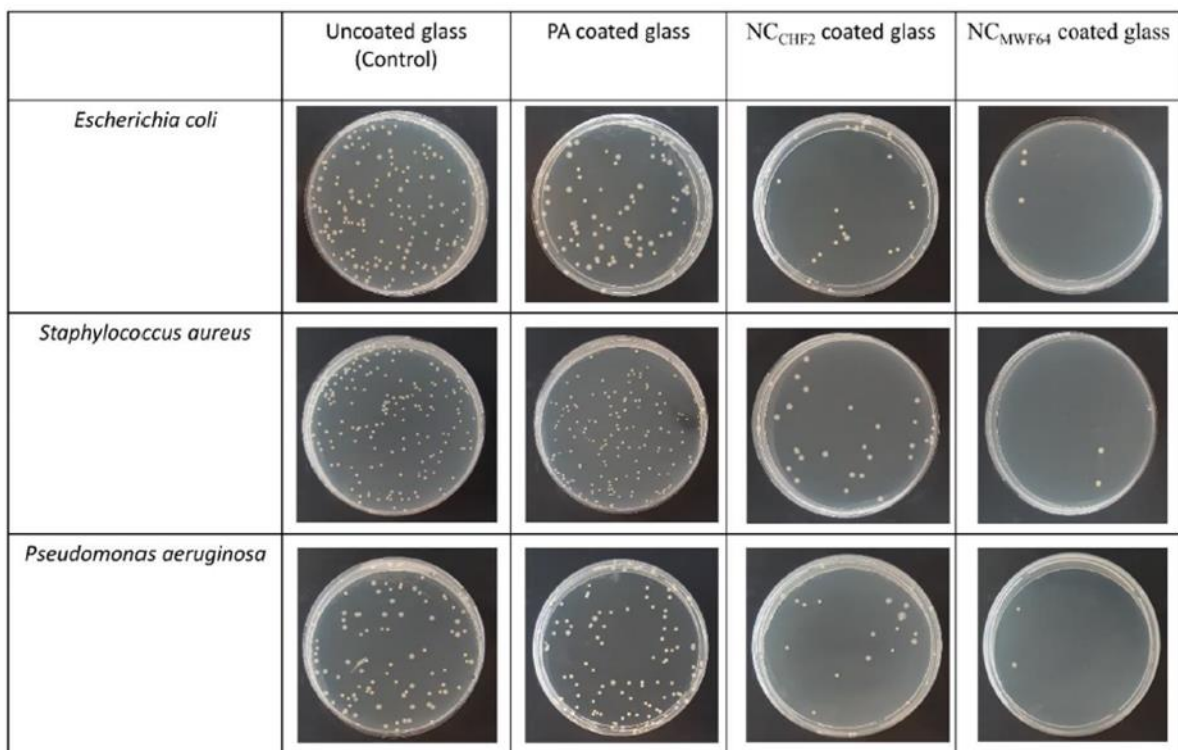


**Figure 3-22:** The CFU of *Escherichia coli*, *Staphylococcus aureus*, and *Pseudomonas aeruginosa* after being exposed to the uncoated glass and the films of the PA6, NC<sub>CHF2</sub>, and NC<sub>MWF64</sub>.

Furthermore, the reduction in the Gram-positive bacterium, *Staphylococcus aureus*, was more significant than the other two bacteria suggesting higher antibacterial efficiency of NC films on *Staphylococcus aureus* (**Figure 3-22**), which agrees with previous studies <sup>125</sup>. The observed activity is probably due to its thick peptidoglycan layer, which contributes to the attraction of Ag ions on the bacterium and consequently leads to bacterial death. *Staphylococcus aureus* is more sensitive to the release of Ag ions than *Escherichia coli* and *Pseudomonas aeruginosa* <sup>126</sup>. Nevertheless, the as-received PA6 film seems not to have any antibacterial efficiency on

any type of bacteria. Given the small size of the AgNPs in NC<sub>MWF64</sub>, the antimicrobial activity tests of the composite films (~120 nm in thickness) performed using *Escherichia coli*, *Staphylococcus aureus*, and *Pseudomonas aeruginosa* showed superior activity over the NC<sub>CHF2</sub> bearing larger AgNPs.

SEM further analyzed the morphology of the solvent-cast NC films to evaluate the distribution of AgNPs (**Figure 3-23**). The SEM image of the NC<sub>MWF64</sub> film displayed some localized AgNP aggregates smaller than ~30 nm (**Figure 3-23a**); in contrast, there were large particulates (~30–100 nm) on the surface of the NC<sub>CHF2</sub> film (**Figure 3-23c**). EDX mapping analysis on the selected area of NC films indicated that the Ag-based signals were more evenly distributed on the film of NC<sub>MWF64</sub> (**Figure 3-23b** and inset therein) than the NC<sub>CHF2</sub> film (**Figure 3-23d** and inset therein), accompanying the superior antimicrobial activity. A spot analysis performed on the EDX map using the Ag-based pink-colored signals showed approximately 1488 pink spots for the selected area of the NC<sub>MWF64</sub> film (**Figure 3-24**). However, the number of pink spots on the EDX map of the NC<sub>CHF2</sub> film was around 1077 (**Figure 3-24**). The results agreed with the small size of AgNPs and their distribution in NC<sub>MWF64</sub>. Finally, considering that the amount of Ag measured by ICP-OES was comparable in both NCs, the EDX mapping further suggested the presence of small AgNPs in NC<sub>MWF64</sub>.

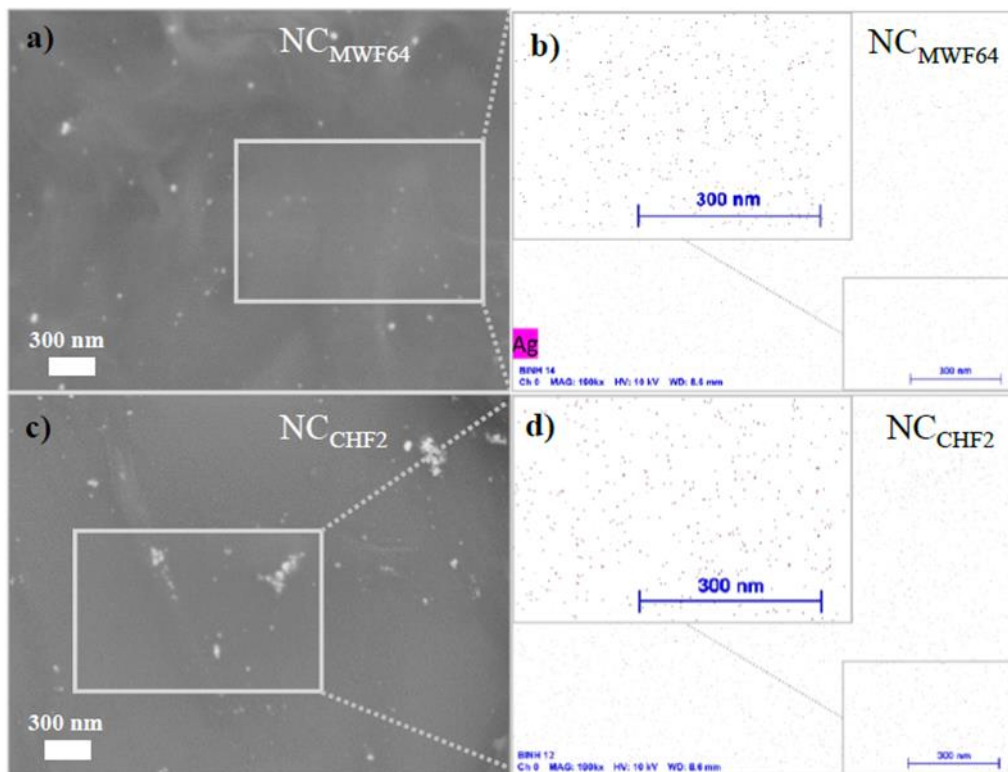


**Figure 3-23:** SEM images (a and c) and EXD mapping (b and d) of the NC<sub>MWF64</sub> and NC<sub>CHF2</sub> films, respectively.

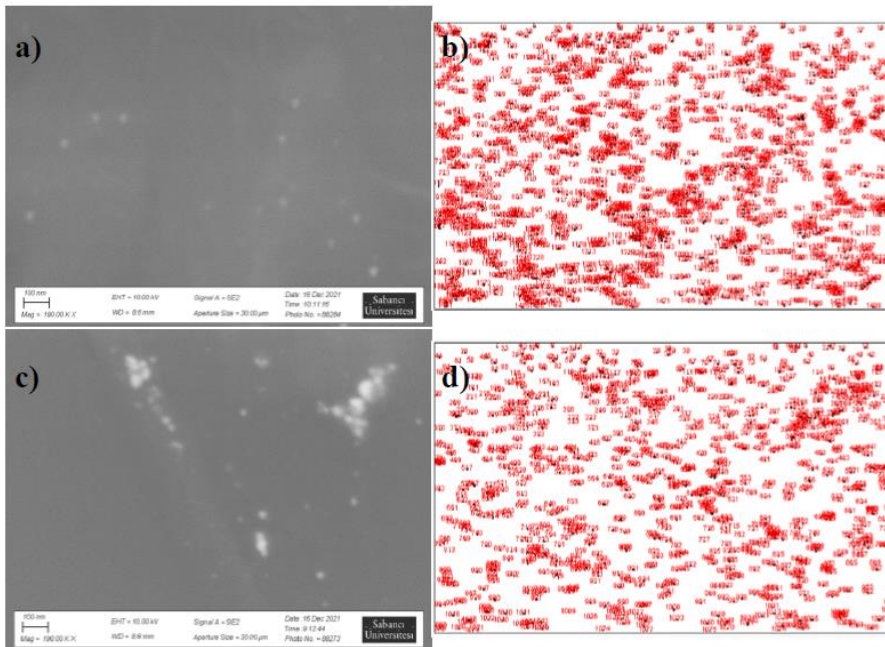


**Figure 3-24:** SEM images (a and c) and EDX mapping analysis (b and d) of the prepared NC<sub>MWF64</sub> and NC<sub>CHF2</sub> films, respectively. The spot analysis was performed using ImageJ software. The threshold used was 6-255 for both images.

### 3.4 Conclusion

The MWFS was, for the first time, introduced as an efficient method to prepare polymer matrix NCs continuously. As a result, nylon-6 NCs with evenly distributed AgNPs ( $\sim 2.59 \pm 0.64$  nm) were prepared in  $\sim 2$  min below  $55^\circ\text{C}$  using FA as a green solvent. In contrast, the CHFS produced  $\sim 50$  nm AgNPs under comparable experimental conditions. Furthermore, the AgNP size was tuned effectively by changing the reaction parameters, including the MWPs, the FR ratios, and the reagent concentrations. As a result, the size of AgNPs became smaller when the concentration of PA6 was increased gradually. Small AgNPs with a narrow size distribution (FWHM  $\sim 60$  for NC<sub>MWF64</sub>) were obtained at a high MWP (40 W) but large AgNPs with a broad size distribution (FWHM  $\sim 80$  for NC<sub>MWF52</sub>) at a low MWP (10 W). The polymer crystallinity was related to the AgNP size, and the  $\gamma$ -phase PA6 (pseudo-hexagonal crystal) was dominant in the presence of small NPs as against the large counterparts. Given the small size of AgNPs in NC<sub>MWF64</sub> (particle size  $\sim 3$  nm) compared to that in NC<sub>CHF2</sub> (particle size  $\sim 50$  nm), the antibacterial activity of the NC<sub>MWF64</sub> film towards Gram-negative and Gram-positive bacteria was superior. More precisely, the activity tests performed using *Escherichia coli* (Gram-negative), *Staphylococcus aureus* (Gram-positive), and *Pseudomonas aeruginosa*

(Gram-negative) revealed that the antibacterial rate of NC<sub>MWF64</sub> was approximately 98.40, 98.91, and 98.93%, respectively. The activity tests proved the impact of the small AgNPs in the NC and appeared as a possible particle size estimation tool. Overall results confirmed the superiority of the MWFS and defined it as a new energy-efficient green and sustainable manufacturing approach for the continuous preparation of polymer matrix NCs. Equally significantly, the MWFS can be scaled up and used to prepare the other polymer- or solid-matrix NCs.

## **Chapter 4: MICROWAVE-PROMOTED CONTINUOUS FLOW SYNTHESIS OF NYLON11 / CELLULOSE ACETATE-COPPER-BASED NANOCOMPOSITES**

### **4.1 Introduction**

The advancement in NCs has taken them to the center of attention thanks to the pros they have while being compared to other materials <sup>127–130</sup>. Some of these advantages are higher mechanical strength and thermal stability <sup>131–134</sup>. Effective incorporation of polymer with NPs leads to polymeric NCs which benefit from outstanding features such as lightweight and processability under the light of nanobiotechnology <sup>135–137</sup>. The defects in NCs would be considerably reduced as a result of the even distribution of NPs in the polymer matrix which paves the way for the improvement of NCs features <sup>135</sup>. As an example, the small size of NPs leads to an increase in surface area to volume ratio. As a result, the quantum effect on NCs will be increased <sup>138</sup>.

Among biopolymers, nylon 11 is a bioplastic that is provided by the polymerization of 11-aminoundecanoic acid. It is widely used in metal coating, and textile <sup>34</sup>. But it has some disadvantages such as low solubility in organic solvents. Considering this fact, CA can be a suitable alternative to PA11. CA constitute a remarkable group of natural polymers. The reaction between cellulose pulp and acetic anhydride results in CA polymer. They are extensively used in various fields such as textile, and drug delivery owing to their excellent biodegradability, low cost, and non-toxicity. However, their poor mechanical features lead to the reduced service life of this polymer. To overcome this, CA is well-complemented by copper-based NPs <sup>32,35,36</sup>. Various experiments have been designed and performed to enhance the features of CA polymer and improve the efficiency of CA NCs in heavy metals removal <sup>139</sup>, sensors <sup>140</sup>, and solar cells <sup>141</sup>. While the antimicrobial efficacy and biocide effect of Cu against microbes and algae has been well-known since ancient times, it offers much higher efficacy in the form of NPs due to their much higher surface-area-to-volume ratio compared to the bulk Cu. It should be noted that one of the problems that can be encountered during the production procedure of CuNPs is Cu oxidation which is due to the high sensitivity of the copper to the air <sup>32</sup>.

During the past few years, several techniques have been investigated for Cu-O<sub>x</sub>NPs syntheses such as co-precipitation <sup>142</sup>, sol-gel <sup>143</sup>, and hydrothermal <sup>144</sup>. As an example, Farman et al.

synthesized CuO NMs using the hydrothermal technique. Cu NMs were uniformly dispersed in CA polymer <sup>144</sup>. In another study, Muhammad et al used a low-temperature technique for developing CA/CuO NCs <sup>145</sup>. In one study, Ocimum sanctum leaf extract was used by Sadanand et al as RA for the immobilization of silver and Cu NPs in cellulose matrix <sup>146</sup>. Also, Muthulak et al. synthesized CA NCs with CuNPs using Terminalia cattappa leaf extract <sup>147</sup>. Although several techniques were tried by various research groups for the synthesis of Cu-O<sub>x</sub>NPs in the CA matrix, continuous synthesis of Cu-O<sub>x</sub>NPs in the CA matrix is still a challenge. all experiments were performed on a lab scale, and they are not scalable. Also, the NPs achieved in most of them are mostly copper oxide derivatives.

In the present study, we investigated the probability of synthesis of 1- PA11 NCs with Cu-O<sub>x</sub>NPs and 2- CA NCs with Cu-O<sub>x</sub>NPs in both batch system and MWFS using RAs such as NaBH<sub>4</sub>, and L-ascorbic acid. Then we successfully synthesized CuNP in a CA matrix via MWFS. Sodium L-ascorbic acid was used as a RA for green and scalable synthesis. The prepared cellulose-based NC films have been characterized by UV-vis, DLS, FTIR, and XRD.

## 4.2 Materials and Methods

### 4.2.1 Materials

Copper (II) nitrate trihydrate (Cu(NO<sub>3</sub>)<sub>2</sub>.3H<sub>2</sub>O, MW:241.60 g/mol, Sigma-Aldrich), copper (II) sulfate pentahydrate (CuSO<sub>4</sub> · 5H<sub>2</sub>O, MW: 249.69 g/mol, Sigma-Aldrich), copper (II) chloride anhydrous (CuCl<sub>2</sub>, MW: 134.45 g/mol, Sigma-Aldrich), copper (II) acetate (Cu(CH<sub>3</sub>COO)<sub>2</sub>, MW: 181.63 g/mol, Sigma-Aldrich), sodium borohydride (NaBH<sub>4</sub>, >99%, Fluka), L-ascorbic acid (MW:176.12 g/mol, Sigma-Aldrich), nylon 11 (PA11) ((C<sub>6</sub>H<sub>11</sub>NO)<sub>n</sub>, >99%), cellulose acetate (CA, MW:183.30 g/mol, Sigma-Aldrich), cellulose acetate propionate (CA\_Pr, Sigma-Aldrich), cellulose acetate butyrate (CA\_Butyrate, Sigma-Aldrich) were used as received. Formic acid (FA, 98-100%, Fisher Chemical), Dimethyl sulfoxide (DMSO, ≥99.7%, Sigma-Aldrich), and *N,N*-dimethylformamide (DMF, >99.8%, Merck) were used as the solvents.

### 4.2.2 Methods

#### The MWFS

The developed MWFS is fabricated from various constituents: 1. A single-mode MW system (Discover, CEM Microwave Technology Ltd.) as an energy source, 2. the fluidic reactor (with the volume of 6.5 mL) coiled by Teflon tubing (diameter: 1/8 inches), 3. A temperature display unit (OMEGA, HH801B) with a compact transition joint probe (OMEGA, WNW0187979) to

monitor the fluid temperature, 4. 20 psi pressure regulator (IDEX Health and Science) to monitor the fluid temperature. 5. infusion pump (KD Scientific) for simultaneous injection of precursors to the system, 6. Two glass containers for separate collection of the product and waste.

### **Preparation of the Polymeric NC**

The preparation of Cu-O<sub>x</sub>NPs and their composites with two different polymers including PA11 and CA were investigated for the synthesis of Cu-based NPs in polymeric matrices.

#### **Preparation of the Cu-O<sub>x</sub> NP/PA11 NC**

In the first step, the solubility of polymer (PA11) in the potential solvents such as DMF and FA was tested. Since PA11 can be highly solved in FA even at RT and FA does not show a reducing effect on Cu precursors, this solvent was selected for use in the following experiments. Among Cu salts, only copper (II) nitrate trihydrate was found to be highly soluble in FA. As a first set of experiments, freshly prepared 5 ml of copper (II) nitrate trihydrate (0.017 gr in 100 ml) was mixed with 5 ml of L-Ascorbic (0.017 gr in 100 ml) and added immediately to the single tube. Then, MI for this batch system (Temperature: 95 °C) started immediately for the synthesis of copper-based NMs. Other volume ratios (copper (II) nitrate trihydrate volume (ml)/ L-Ascorbic volume (ml)) which were tested are 5/10 and 2/10 in this set of experiments. The time that samples were exposed to MW irradiation was 15 minutes. The final product solutions were used for UV-vis analysis. However, no formation of copper-based NMs was observed in the first experiment set. The MWFS was also utilized with two syringes (one of them contains copper (II) nitrate trihydrate, 0.017 gr in 100 ml FA, and the other syringe has L-Ascorbic, 0.017 gr in 100 ml FA) at an FR ratio of 1:1 (L-Ascorbic (ml/min): copper (II) nitrate trihydrate (ml/min)) under various MWPs from 30 to 100 W. However, no particles were synthesized in this experiment set, too. As a result, an additional RA is needed to be added to the system. Since PA11 cannot be solved in DMF at RT and excessive addition of DMF will result in an undesirable change in final product features due to precipitation of PA11, the maximum limit for the addition of DMF should be defined which is recorded as 600 µl to be added to 0.16 gr PA11 in 10 ml of FA (stock solution).

In the second set of experiments, in a MW-assisted batch system, 0.002 gr of copper (II) nitrate trihydrate in 10 ml of stock solution and 0.04 gr of L-ascorbic acid in DMF were mixed. Different DMF volumes (400 and, 600 µl) and MW exposure times (15, and 30 minutes) were tested. The freshly prepared Cu-O<sub>x</sub>/PA11 NC solutions were used for UV-vis analysis. In the

above-mentioned sets of experiments, the possibility of Cu-O<sub>x</sub>NPs synthesis was tested using copper (II) nitrate trihydrate and L-ascorbic acid as a precursor and RA respectively in a MW-batch system with or without DMF as a second RA.

In the third set of experiments, two precursors; copper (II) chloride and copper (II) sulfate pentahydrate which were not soluble in FA could be used thanks to the addition of DMF to the assay. Regarding copper (II) chloride, in the batch system, 10 ml of L-ascorbic acid (0.017 mg/ml) in stock solution (0.16 gr PA11 in 10 ml of FA) was mixed with different amounts of copper (II) chloride in DMF (0.013 mg/ml) which were 10, 300, and 600 µl under MW irradiation for 15 minutes at a constant temperature of 100 °C with high stirring. Also, after setting the volume of copper (II) chloride in DMF (0.013 mg/ml) at 600 µl, the L-ascorbic acid concentration and the MW exposure time were increased up to 0.034 mg/ml, and 45 minutes respectively, and preparation of Cu-O<sub>x</sub> NCs were investigated. The Cu-O<sub>x</sub>/PA11 NCs solutions synthesized in this step were used for UV-vis analysis. Due to the low solubility of PA in solvents, experiments with copper (II) sulfate pentahydrate were conducted without the use of PA. Thus, 10 ml of copper (II) sulfate pentahydrate in DMF (15 mg/ml) was mixed with 4 ml of NaBH<sub>4</sub> in DMF (4 mg/ml) in the batch system and became exposed to MW irradiation of 100 W for 30 minutes. The prepared NCs solutions in this part were also analyzed by UV-vis analysis. Due to the formation of CuNPs in this part, the flow system was also tested for copper (II) sulfate pentahydrate. The FRs 1 and 0.25 ml/min were used for the simultaneous injection of 10 ml of copper (II) sulfate pentahydrate in DMF (15 mg/ml) and 4 ml of NaBH<sub>4</sub> in DMF (4 mg/ml) using two separated syringes to the reactor which is exposed to MW irradiation of 100 W. Also, the concentration of both copper (II) sulfate pentahydrate and NaBH<sub>4</sub> in DMF was reduced by one-eighth and one-sixteenth of the initial concentration with varying MW powers of 50, 20, and 10 W. However, in all experimental conditions for the flow system, blockage or precipitation happened.

### **Preparation of the Cu-O<sub>x</sub> NP/CA NC**

Noteworthy is the fact that the solubility of the polymer in the synthesis of polymeric NCs is of great importance and increasing the amount of polymer in NCs improves the product in terms of mechanical, electric, and optical properties while being compared with individual constituents. As a result, CA with high solubility in different solvents (while being compared with PA11) was chosen as an alternative to PA11. After measuring the solubility (mg/ml) of three CAs such as CA, CA\_Pr, and CA\_Butyrate in four solvents: Acetone, DMF, Ethanol, and DMSO, CA has the highest solubility in DMF as an organic solvent.

Following this, in the first set of experiments, the synthesis of Cu-O<sub>x</sub>NPs using copper (II) sulfate pentahydrate and L-ascorbic acid in DMF as a precursor and RA in the batch system was evaluated using a heating source of the heater. In two separate assays, 1) 5 ml of 0.2 M L-ascorbic acid was mixed with 12 ml of 0.1 M copper (II) sulfate pentahydrate in DMF on the heater for 30 min. 2) 5 ml of 0.2 M L-ascorbic acid and 3 ml of 1 M NaBH<sub>4</sub> were added to 12 ml of 0.1 M copper (II) sulfate pentahydrate in DMF and placed on the heater for 2 hours. The UV-Vis analysis was performed for both samples. Due to low percentages of CuNPs and the high reducing efficiency of NaBH<sub>4</sub> another set of experiments was designed.

In the second set of experiments, copper (II) sulfate pentahydrate (0.03 M) was mixed with L-ascorbic acid (0.06 M) in DMF in a single vial at volumes of (10ml/10ml) (without any polymer) for 15 min at 1) RT and 2) 100 °C reached by using a single-mode MW. The samples were analyzed by UV-Vis. After the determination of CuO, CuO<sub>2</sub>, and CuNP formation, the polymer can be included in the following experiment set.

In the third set, 10 ml of 0.03 M solutions of copper (II) sulfate pentahydrate, 10 ml of 0.06 M solution of L-ascorbic acid, and 6 ml of CA (75 mg/ml) in DMF were mixed in a single vial for 15, and 30 min using MW of fixed temperature (100 °C). The UV-Vis analysis of produced samples was performed. Furthermore, the same conditions were used for the MW-assisted flow system. For this purpose, simultaneous injections of 0.03 M of copper (II) sulfate pentahydrate (premixed with 0.06 M of L-ascorbic acid in DMF) and CA in DMF (55 mg/ml) to the reactor were performed using two separate syringes at FRs of 0.1:0.5 ml/min (for copper (II) sulfate pentahydrate with L-ascorbic acid: CA) at RT and MW power of 70 W.

Additionally, the polymer was excluded from the experiment to investigate the effect of polymer on the synthesis of Cu-O<sub>x</sub>NPs in an MW-assisted fluidic system.

Furthermore, in one separate set of polymer-included experiments, various MW powers of 40, 60, and 80 W were tested to study the effect of MW power on the formation Cu-O<sub>x</sub> NCs in an MW-assisted fluidic system. And UV-Vis measurements were performed for all samples.

In order to remove the unreacted reagents, the Cu-O<sub>x</sub> NP/CA NC which are freshly produced was added to distilled water dropwise under vigorous stirring. Then, filtering was performed for the collection of formed precipitate through a PTFE membrane (0.45 µm, ISOLAB) and finally washed with distilled water. After drying in an oven at 40 °C overnight, various analysis was performed on the CuNP/CA NC in solid form.

### 4.3 Results and Discussion

The continuous preparation of Cu-O<sub>x</sub> NP/Polymer NCs was investigated using the MWFS described in **Figure 4-1**. As can be seen in this figure, the system consists of MW as an energy source (2.45 GHz), a fluidic reactor coiled with tubings (~6.5 mL), two syringes for injection of precursors, a thermocouple temperature probe, a pressurized N<sub>2</sub> gas tank equipped by the regulator (20 psi), two separate bottles for waste, and product.

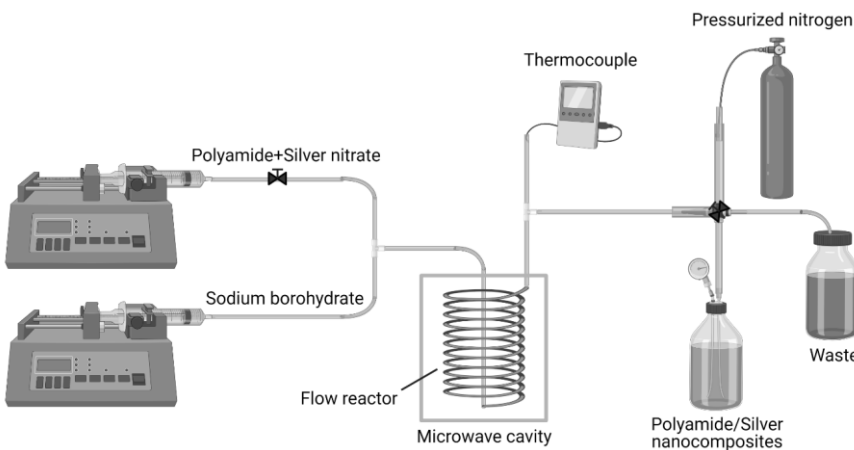


**Figure 4-1:** Graphical illustration of the MWFS for the continuous synthesis of Cu-O<sub>x</sub>NPs in the polymer matrix.

Regarding the preparation of Cu-based NPs and their composites with polymer, the solubility of the polymer in the utilized solvent for the formation of polymer-based NCs is of great importance.

#### 4.3.1 Preparation of the Cu-O<sub>x</sub> NP/PA11 NC

Firstly, PA11 was utilized for the preparation of Cu-O<sub>x</sub>NPs and their composites. Because each derivative of PA is only soluble in FA, the solubility of all available Cu salts including copper (II) chloride anhydrous, copper (II) nitrate trihydrate, and copper(II) acetate in FA solvent were tested. None of the copper salts were found to be soluble in FA, except copper (II) nitrate trihydrate. It should be noted that for solving Cu salts in FA, two methods were tried. The first solving at RT was unsuccessful. The second method was heat assisted sonication bath (70 °C and 20 minutes) which was only effective for copper (II) nitrate trihydrate. Since the solubility of the precursor is one of the important factors in the optimization process of polymeric NCs synthesis, the next step after choosing the Cu salt is its solubility in FA. The highest amount of copper (II) nitrate trihydrate that can be solved in FA is 0.017 gr in 100 ml of FA. As a RA, L-ascorbic acid was utilized for the possible reduction of Cu ions. Then, the synthesis of Cu-

based NMs was investigated using a MW-assisted batch system. Taking the boiling point of FA into consideration, the maximum temperature set for synthesis was 95 °C.

In the first set of experiments, 5 ml of copper (II) nitrate trihydrate (0.017 gr in 100 ml) was mixed with 5 ml of L-Ascorbic (0.017 gr in 100 ml) and put in a single tube. Then, a MW-batch system (Temperature: 95 °C) was tried for the synthesis of Cu-based NMs, and Sample 1 was used as a label for the product of this part. Other volume ratios (copper (II) nitrate trihydrate volume (ml)/ L-Ascorbic volume (ml)) which were tested are 5/10 and 2/10 in this set of experiments and the final products were named sample 2, and sample 3. The time that samples were exposed to MW irradiation was 15 minutes. As can be understood from **Figure 4-2**, no formation of Cu-based NMs was observed in the first experiment set. In order to explore the probability of Cu-based NPs synthesis through a fluidic system, our MWFS was utilized with two syringes (one of them contains copper (II) nitrate trihydrate, 0.017 gr in 100 ml FA, and the other syringe has L-ascorbic acid, 0.017 gr in 100 ml FA).

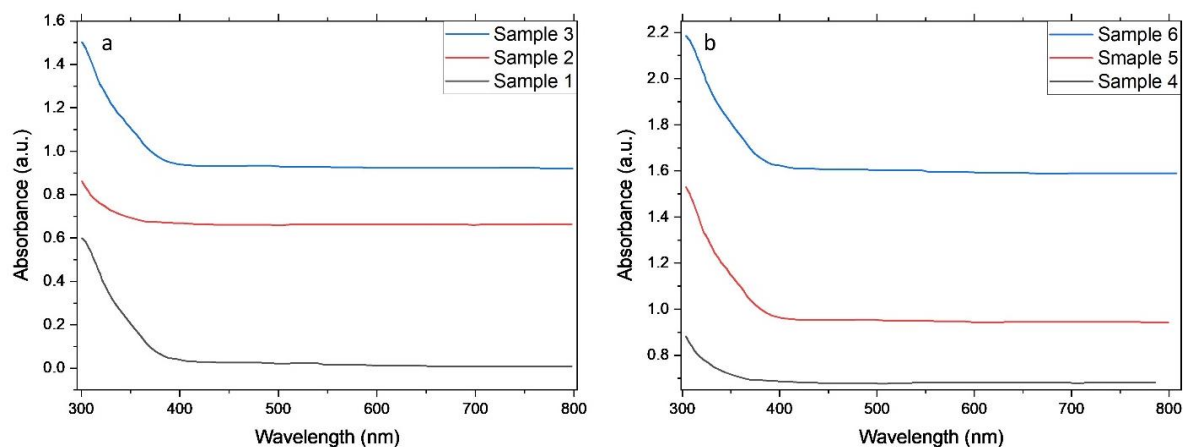


**Figure 4-2:** UV-Vis spectra of samples produced using a) MW-batch and, b) MW-continuous system

Significant parameters such as FRs, MWP, and temperature measured during the MW exposure are tabulated in **Table 4-1**. As can be seen in **Table 4-1**, FA boiling temperature reached and exceeded by increasing the MWP. However, no particles were synthesized in this experiment set and as proof of evidence, UV results are provided in **Figure 4-2**.

**Table 4-1:** FRs and MW were examined for the possible synthesis of Cu-based NPs.

Copper (II) nitrate trihydrate Rate (ml/min)	L-ascorbic Rate (ml/min)	MW Power(W)	Temp (°C)	Sample No
1	1	30	27	Sample 4
1	1	60	39	Sample 5

1	1	100	98	Sample 6
---	---	-----	----	----------

By evaluation of the results obtained by the above-mentioned two experiment sets, it can be concluded that an additional RA is required. As a result, DMF was chosen to be used in the system. In the case of DMF addition, there was a limitation regarding the solubility of PA11 in DMF. PA11 is not soluble in DMF and the addition of DMF to the system may cause undesirable changes in the properties of synthesized NCs. As a result, one additional test is needed to define the maximum DMF amount which can be added to the system which contains PA11. The maximum amount of PA11 in FA was chosen as 0.16 gr in 10 ml of FA. In order to find the maximum amount of DMF, starting from 100  $\mu$ l, the amount of DMF added to 0.16 gr of PA11 in 10 ml of FA (stock solution) was increased and 600  $\mu$ l was recorded as DMF maximum amount.

In the second set of experiments, based on obtained results, 0.002 gr of copper (II) nitrate trihydrate in 10 ml of stock solution was mixed with 0.04 gr of L-ascorbic acid in DMF. The variable parameters were DMF volume (400 and, 600  $\mu$ l) and MW exposure time (15, and 30 minutes). The temperature for MW exposure was set at 95 °C. The volume of DMF and MW time examined for the possible synthesis of Cu-based NPs are tabulated in **Table 4-2**.

**Table 4-2:** The volume of DMF and time of MW exposure for the possible synthesis of Cu-O<sub>x</sub>/PA11 NC.

Volume of DMF( $\mu$ l)	Time (min)	Sample No
600	30	NC <sub>1</sub>
400	30	NC <sub>2</sub>
600	15	NC <sub>3</sub>
400	15	NC <sub>4</sub>

As can be seen in **Figure 4-3a**, the color of the products indicated the formation of CuO NPs. However, analyses such as UV-vis analysis are required to confirm the formation of particles. Due to the noises caused by FA in the UV-vis spectrum for wavelengths less than 300 nm, some post-treatment such as centrifugation of the produced sample and its dispersion in ethanol or

water was done before UV-vis analysis. **Figure 4-3b** Provides the results of UV-Vis analysis for NC<sub>1</sub>, NC<sub>2</sub>, NC<sub>3</sub>, and NC<sub>4</sub> in this experiment set. As provided in this figure, the maximum absorbance for all 4 samples is around 260 nm which has been previously demonstrated to be a characteristic of CuO NPs.

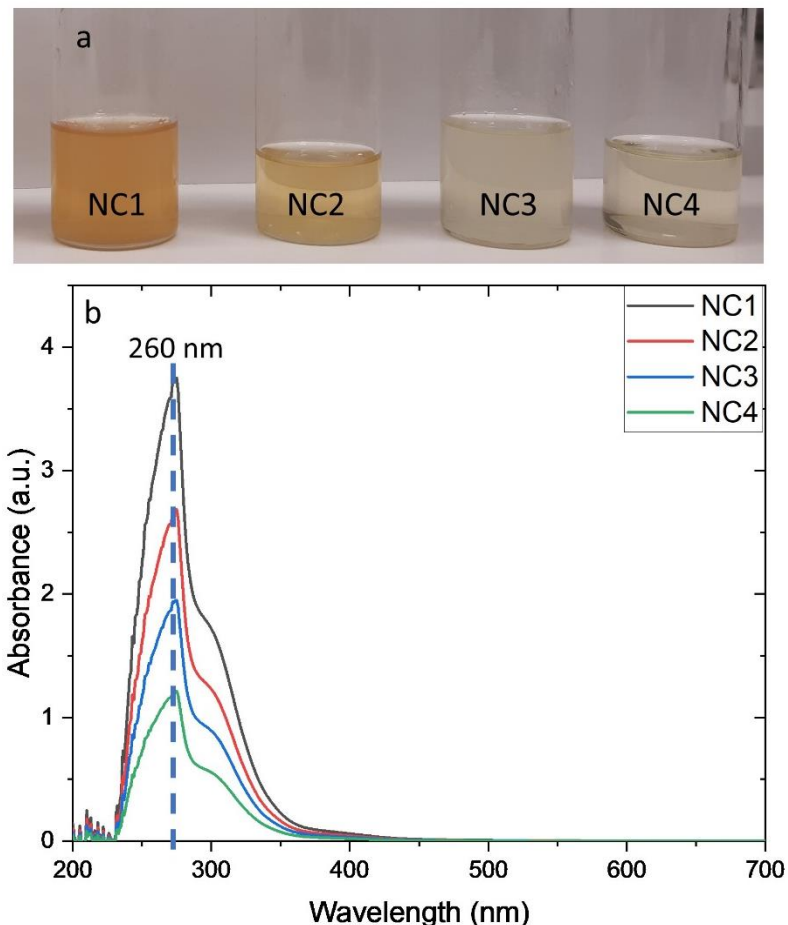


**Figure 4-3:** a) Color change and b) UV-Vis spectra of samples produced using MW-batch system

The aforementioned assays studied the probability of formation of CuO<sub>x</sub>NPs using copper (II) nitrate trihydrate and L-ascorbic acid as a precursor and RA respectively in an MW-assisted batch/fluidic system with or without DMF as a second RA. As a result, only CuO NPs were synthesized.

In the third set of experiments, precursors other than copper (II) nitrate trihydrate were studied to synthesize Cu-O<sub>x</sub>NPs. Both copper (II) chloride and copper (II) sulfate pentahydrate were tested for possible production of Cu-O<sub>x</sub>NPs.

Firstly, copper (II) chloride was dissolved in DMF to have a final concentration of 0.013 mg/ml (Solution A). Besides, the stock solution of PA11 was provided by solving 0.16 gr polymer in

10 ml of FA. Then, L-ascorbic acid was dissolved in stock solution to obtain the final concentration of 0.017 mg/ml (Solution B). In the batch system, 10 ml of solution B was mixed with different amounts of solution A which were 10, 300, and 600  $\mu$ l under MI for 15 minutes at a constant temperature of 100 °C with high stirring which resulted in the formation of CuO NP which was labeled as NC<sub>5</sub>, NC<sub>6</sub>, NC<sub>7</sub> respectively. As can be seen in **Figure 4-4a**, the color of the products indicated the formation of CuO NPs for all three samples. In addition, analysis such as UV-vis analysis is required to confirm the formation of particles. **Figure 4-4b** provides the results of UV-Vis analysis for samples NC<sub>5</sub>, NC<sub>6</sub>, and NC<sub>7</sub> in this experiment set. As provided in this figure, the optical absorbance of produced NPs is around 260 nm which has been previously demonstrated to be a characteristic of CuO NPs <sup>148</sup>. In order to investigate the effect of RT on the translation of CuO NPs to other Cu-based NP, the NC<sub>7</sub> was left at RT for 24 hours. However, the only color of the sample became darker and there was no change in the optical absorbance of the NC<sub>7</sub> sample (**Figure 4-5**). In addition, considering the MI time and concentration of the RA as two effective factors on formed NPs, L-ascorbic acid concentration was increased twice and fixed at 0.034 mg/ml. Also, the time was increased to 45 minutes, and MW times of 15, 30, and 45 min were tried to obtain samples NC<sub>8</sub>, NC<sub>9</sub>, and NC<sub>10</sub>. The volume of solution A for mixing with solution B was fixed at 600  $\mu$ l. But the other parameters remained unchanged. **Table 4-3** summarizes all involved parameters along with sample numbers. **Figure 4-4a** shows the color change from milky to brown over increasing the MW irradiation time. However, the color of the products signifies the formation of CuO NPs for all samples. **Figure 4-4c** depicts the results of UV-Vis analysis for samples NC<sub>8</sub>, NC<sub>9</sub>, and NC<sub>10</sub>. As can be understood from this figure, the optical absorbance of produced NPs is approximately 260 nm which has been previously demonstrated to be a characteristic of CuO NPs <sup>148</sup>. As a result, although most effectual parameters were changed, only CuO NPs were synthesized.

**Table 4-3:** Input concentrations, time, and temperature were examined for the possible synthesis of Cu-O<sub>x</sub> NC

copper (II) chloride in DMF (gr/ml)	Volume of DMF ( $\mu$ l)	L-ascorbic acid in Stock Solution (PA in FA) (gr/ml)	Volume of FA (ml)	Time (min)	Temp (°C)	Sample No
0.013	600	0.034	10	15	100	NC <sub>8</sub>

0.013	600	0.034	10	30	100	NC <sub>9</sub>
0.013	600	0.034	10	45	100	NC <sub>10</sub>

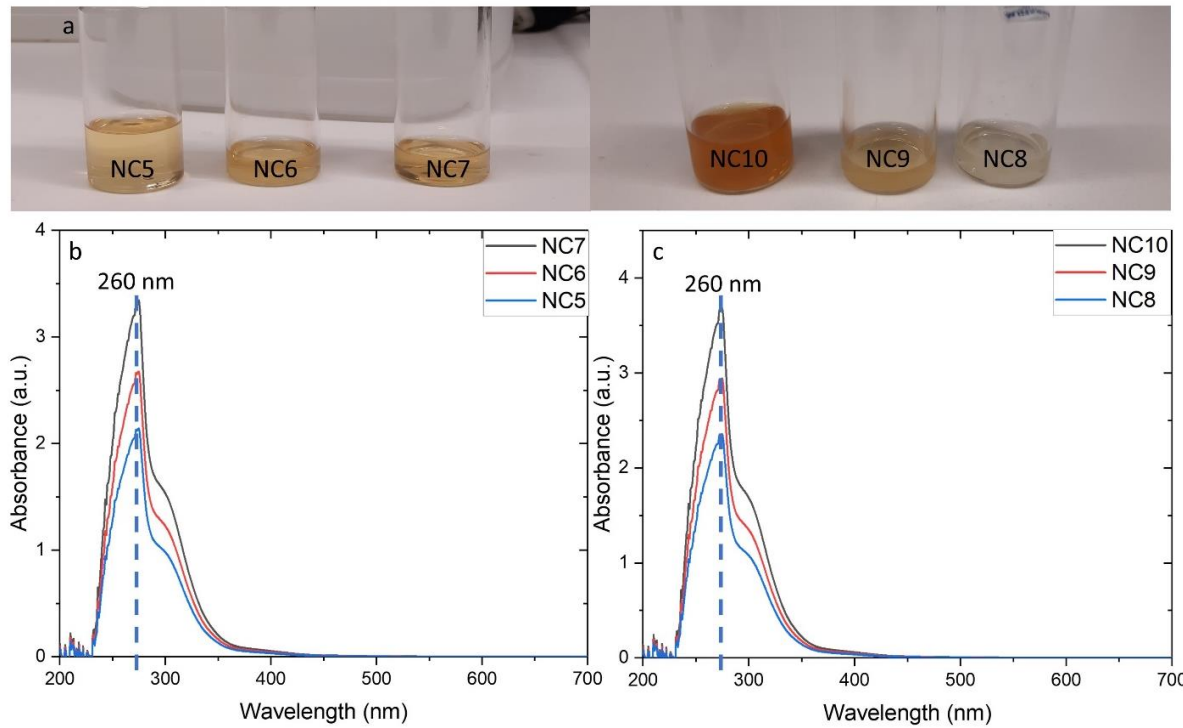


**Figure 4-3:** a) Color change and b) UV-Vis spectra of samples produced using MW-batch system

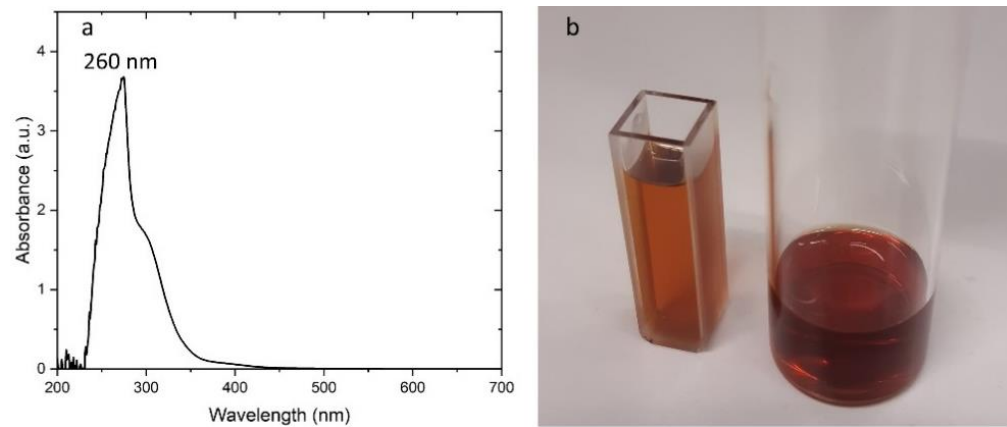


**Figure 4-4:** a) UV-Vis spectra of NC<sub>7</sub> after being left at RT and b) its color change

All the results obtained until this part are showing the formation of CuO NPs. For Cu NPs synthesis, another precursor, copper (II) sulfate pentahydrate was used. Due to issues related to the low solving rate of PA11 in solvents which causes some difficulties in the synthesis procedure, further assays were conducted without polymer and the probability of Cu NPs

formation was examined. For this aim, copper (II) sulfate pentahydrate was dissolved in DMF to have a final concentration of 15 mg/ml and labeled as solution C. In addition, NaBH<sub>4</sub> was solved in DMF to get a final concentration of 4 mg/ml and labeled as solution D (RA). In the batch system, 10 ml of solution C was mixed with 4 ml of solution D and heated under the power of 100 W which reached the temperature of approximately 130 °C for 30 minutes. The mixture turned dark red indicating the formation of CuNPs. **Figures 4-6 a, b, and c** provide the color of copper (II) sulfate pentahydrate in DMF, the color change of synthesized Cu NP, and its UV-Vis spectrum, respectively. As can be seen, there are two peaks in 280 and 585 which signify the formation of CuO NP and Cu NP, respectively <sup>148,149</sup>. Considering the absorbance in these two peaks, the concentration of CuO NP is significantly higher than Cu NP.

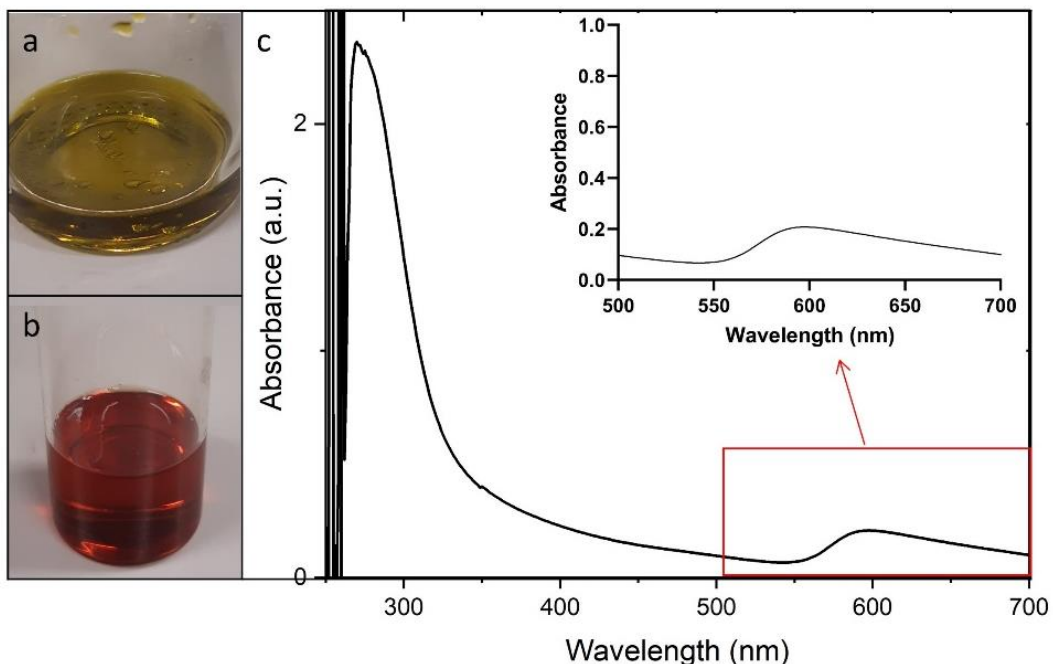


**Figure 4-5:** a) color of copper (II) sulfate pentahydrate in DMF, b) color change of synthesized CuNP, and c) it's UV-Vis spectrum

After the synthesis of CuNP in the batch system, the flow system was tried. In this MW-assisted continuous system, two syringes were used for the simultaneous injection of solutions C and D into the reactor. The FR of solution C and solution D was set at 1 and 0.25 ml/min, respectively, and both solutions were injected into the reactor which is exposed to MW radiation of 100 W. However, due to the rapid nucleation of NPs resulting from the high concentration of NaBH<sub>4</sub> as a RA and high MW power in the microfluidic system, the blockage happened (**Figure 4-7 a, b**) in the reactor, and a new tubing system was required. Then, the concentration of both solution C and the solution was reduced to one-eighth and one-sixteenth

of the initial concentration in separate two experiments at the same MW power of 100 W. Unfortunately, the same blockage happened in both separate experiments but different from the first experiment (flow system in the high concentration of precursor and RA) the blockage was removable with aqua regia and there was no need to change the tubing system. Following this, the MW power was reduced and in separate experiments, 50, 20, and 10 W were tested. In all conditions, precipitates were formed (**Figure 4-7c**). Based on the results, it was concluded that the formation of Cu NPs in the above-mentioned experimental conditions is not achievable with a continuous system due to the high rate of nucleation in a fluidic system. The stabilizing agent can be tested to find out whether the issue of precipitation or blockage would be addressed or not. However, due to the limited solubility of PA11 in solvents, it was almost impossible to add this polymer to the system.



**Figure 4-6:** Images of (a),(b) blockage, happened, (c) precipitation formed.

#### 4.3.2 Preparation of the Cu-O<sub>x</sub> NP/CA NC

As a second polymer, CA was utilized for the preparation of Cu-O<sub>x</sub>NPs in polymer matrices. One of the important factors in the synthesis of polymeric NCs is polymer solubility which provides the final amount of polymer in the produced NC. Increasing the amount of polymer in NC improves the product in terms of mechanical, electric, and optical properties while being compared with individual constituents. For this reason, after choosing CA as a polymer, its solubility in various solvents has been investigated. **Table 4-4** provides the solubility (mg/ml) of three CAs such as CA, CA\_Pr, and CA\_Butyrate in four solvents: Acetone, DMF, Ethanol, and DMSO.

**Table 4-4:** The solubility (mg/ml) of CAs in various solvents.

Solvents	CA	CA_Butyrate	CA_Pr

Acetone	30	35	24.5
DMF	75	50	30
Ethanol	-	-	-
DMSO	15	20	15

As can be seen in **Table 4-4**, CA has the highest solubility in DMF as an organic solvent. Although Ethanol has high efficiency in the reduction of Cu salt to CuNPs, none of the used CAs were soluble in Ethanol. After choosing a polymer, copper (II) sulfate pentahydrate along with NaBH<sub>4</sub> and L-ascorbic acid as potential RAs were tested and the possibility of Cu-O<sub>x</sub> synthesis was investigated in separate experimental batches.

In the first set of experiment, the chemical reduction process of copper (II) sulfate pentahydrate using L-ascorbic acid in DMF were tested in the batch system using a heater as a heating source. To investigate the effect of DMF on copper (II) sulfate pentahydrate as a RA, the UV-Vis analysis was performed for 0.1 M copper (II) sulfate pentahydrate in DMF (sample 7). As can be seen in **Figure 4-8d**, there was no peak indicating that no Cu-O<sub>x</sub> particles were synthesized. The color of the sample in **Figure 4-8a** confirms the UV-Vis analysis result. Then in two different experiments, 1) 5 ml of 0.2 M L-ascorbic acid was added to 12 ml of 0.1 M copper (II) sulfate pentahydrate in DMF and the mixture was heated for 30 min on the heater (sample 8). 2) 5 ml of 0.2 M L-ascorbic acid and 3 ml of 1 M NaBH<sub>4</sub> were added to 12 ml of 0.1 M copper (II) sulfate pentahydrate in DMF and the mixture was heated for 2 hours on the heater (Sample 9). The UV-Vis analysis was performed for both samples 8 and 9 and the results were provided in **Figure 4-8d**. There was only a small peak at approximately 400 nm in sample 8, while only a shoulder was noticed in sample 9. However, in **Figures 4-8b and c**, the color of the samples was green and black which indicates that low percentages of CuNPs were formed. In sample 9, the addition of NaBH<sub>4</sub> led to precipitation due to the high reducing efficiency of NaBH<sub>4</sub>. As a result, another set of experiments is needed to be designed and tried.

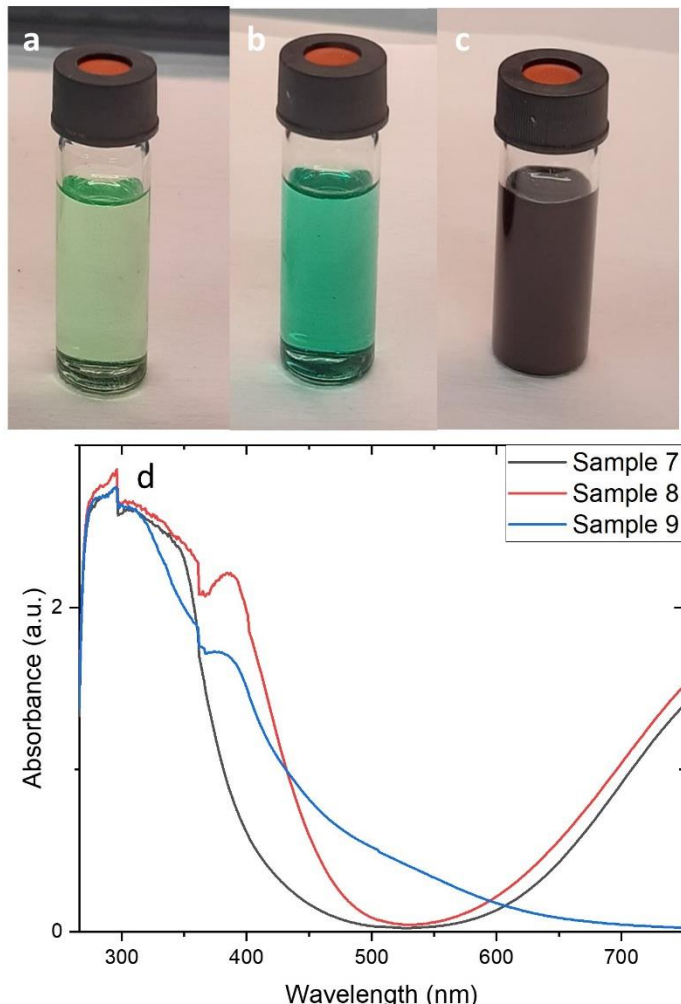


**Figure 4-8:** Color change of a) sample 7, b) sample 8, c) sample 9, and d) their UV-Vis spectra. In the second set of experiments, 10 ml of 0.03 M solutions of copper (II) sulfate pentahydrate in DMF was mixed with 10 ml of 0.06 M solutions of L-ascorbic acid in DMF in a single vial (without any Polymer) at two different temperatures: 1. RT (sample 10) and, 2. fixed temperature of 100 °C (sample 11) for 15 minutes using a single-mode MW system (Discover, CEM Microwave Technology Ltd). As can be seen in **Figure 4-9c**, there was no peak in UV-Vis peak related to sample 10 revealing that no particle was formed. This result can be confirmed by the color of the solution which is provided in **Figure 4-9a**. However, after exposure of the sample to the MW irradiation with a fixed temperature of 100 °C, the color of the solution changed to red which indicates the formation of Cu-O<sub>x</sub>NPs (**Figure 4-9b**). Based on the UV-Vis spectrum obtained in **Figure 4-9c**, peaks at 300, 400, and a shoulder at 560 nm indicate the formation of CuO, CuO<sub>2</sub>, and CuNPs, respectively. In this set of experiments, the polymer was excluded and the potential of this design of experiment for Cu-O<sub>x</sub>NPs formation

was investigated. In the following set, the polymer can be introduced to the reaction batch as a matrix for Cu-O<sub>x</sub>NP formation. Also, different times of MW irradiation can be tested.

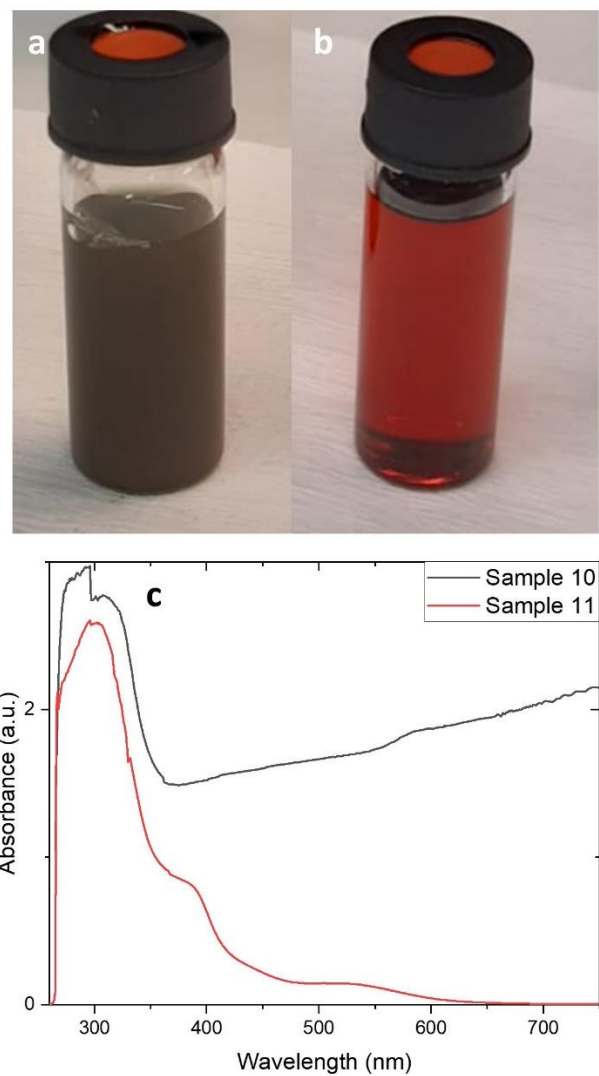


**Figure 4-9:** Color change of a) sample 10, b) sample 11, and d) their UV-Vis spectra

In the third set of experiments, 10 ml of 0.03 M solutions of copper (II) sulfate pentahydrate in DMF was mixed with 10 ml of 0.06 M solution of L-ascorbic acid in DMF and 6 ml of CA (75 mg/ml) in a single vial at a fixed temperature of 100 °C for 15, and 30 min using MW as an energy source which was labeled as NC<sub>11</sub>, and NC<sub>12</sub>, respectively. After exposure of the sample to the MW irradiation with a fixed temperature of 100 °C for 15 min (NC<sub>11</sub>), the color of the solution changed to dark red which indicates the formation of Cu-O<sub>x</sub>NPs (**Figure 4-10a**). Based on the UV-Vis spectrum obtained in **Figure 4-10c**, peaks at 300, 400, and a shoulder at 560 nm indicate the formation of CuO, CuO<sub>2</sub>, and CuNPs, respectively. However, increasing the time of the sample exposure to MW from 15 min to 30 min resulted in a dark yellow sample indicating the formation of copper oxide NPs (**Figure 4-10b**). Also, based on the UV-Vis

spectrum of NC<sub>12</sub>, no CuNPs were formed (**Figure 4-10c**). As a result, 15 minutes of MW irradiation is the best choice for the synthesis of CA/Cu-O<sub>x</sub> polymeric NCs.

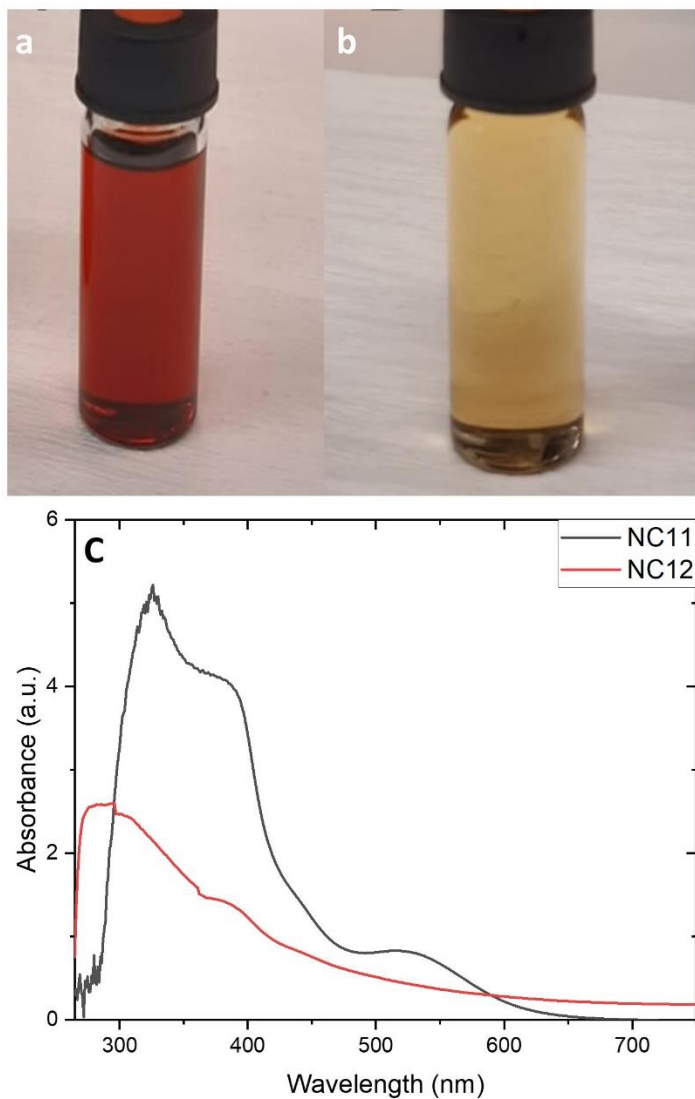


**Figure 4-10 :** Color change of a) NC<sub>11</sub>, b) NC<sub>12</sub>, and d) their UV-Vis spectra

In the fourth set of experiments, the MW-assisted flow system was tested for the synthesis of polymeric NC. In this part, a flow system (the reactor wrapped by tubings) was used instead of a batch system such as vials. In syringe A, 0.03 M of copper (II) sulfate pentahydrate was premixed with 0.06 M of L-ascorbic acid in DMF. In syringe B, CA in DMF (55 mg/ml) was prepared. Then syringe A and B with FRs of 0.1 and 0.5 ml/min, respectively were used as input to our flow system. In the first assay, the precursor was fed to the flow system at RT (NC<sub>13</sub>). In the second assay, the MW power was adjusted to 70 W which gave a temperature of 40 °C (NC<sub>14</sub>). Also, NC<sub>14</sub> was filtered before UV-Vis measurement. As can be seen in **Figure 4-11c**, there was no NP formation in NC<sub>13</sub> which can be confirmed by the color of the

sample in **Figure 4-11a**. But, NC<sub>14</sub> represents the formation of CA/Cu-O<sub>x</sub> polymeric NCs which can be confirmed by sample color in **Figure 4-11b**.

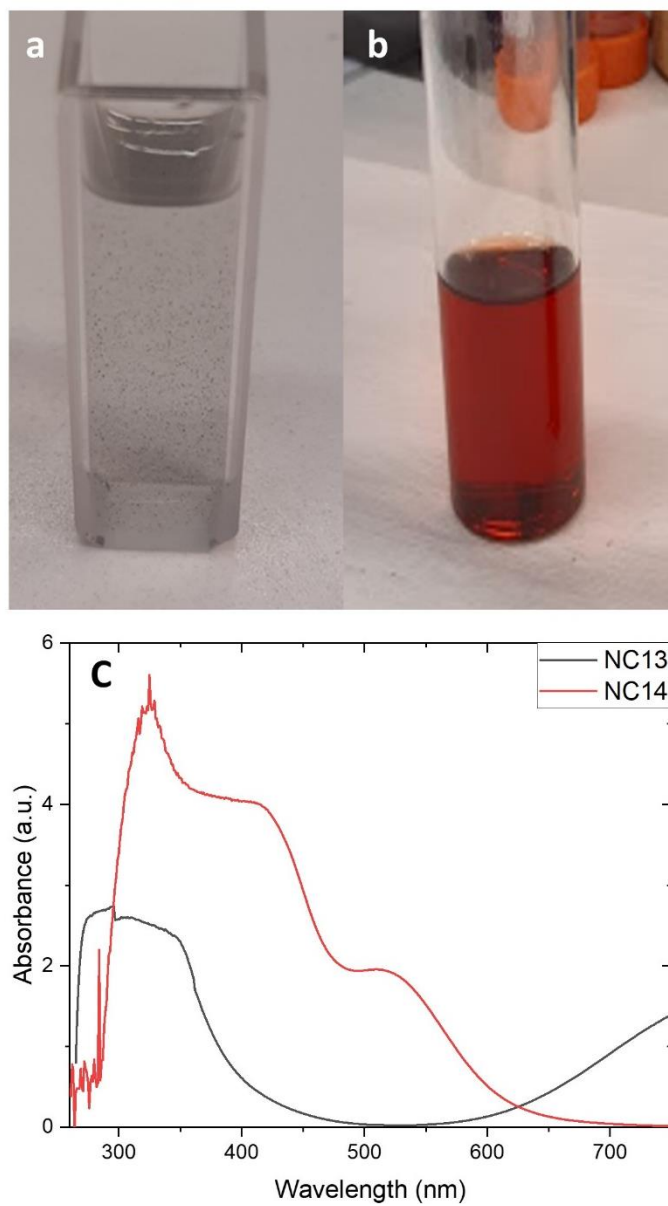


**Figure 4-11 :** Color change of a) NC<sub>13</sub>, b) NC<sub>14</sub>, and d) their UV-Vis spectra

In order to monitor the effect of the polymer on the formation of CA/Cu-O<sub>x</sub> NPs, the experiment was designed using only copper (II) sulfate pentahydrate and L-ascorbic acid without introducing any polymer to the system. In syringe A, 0.03 M of copper (II) sulfate pentahydrate in DMF was prepared. In syringe B, 0.06 M of L-ascorbic acid in DMF was provided. Then syringe A and B with FRs of 0.1 and 0.5 ml/min, respectively were used as input to our flow system. In this assay, the precursor was fed to the flow system using the MW irradiation with power adjusted to 70 W which gave a temperature of 37 °C (NC<sub>15</sub>). Also, NC<sub>15</sub> was filtered before UV-Vis measurement. As can be understood from **Figure 4-12a**, there were peaks at

300 and 400 nm which show the formation of  $\text{Cu}_2\text{O}$  and  $\text{CuO}$ . However, there was no peak related to the formation of Cu NPs. The color of the sample is also dark brown (**Figure 4-12b**). It should be noted that in the case of reducing the FR from 0.1/0.5 (ml/min) for syringe A/syringe B to 0.1/0.2, blockage in the flow system happened.

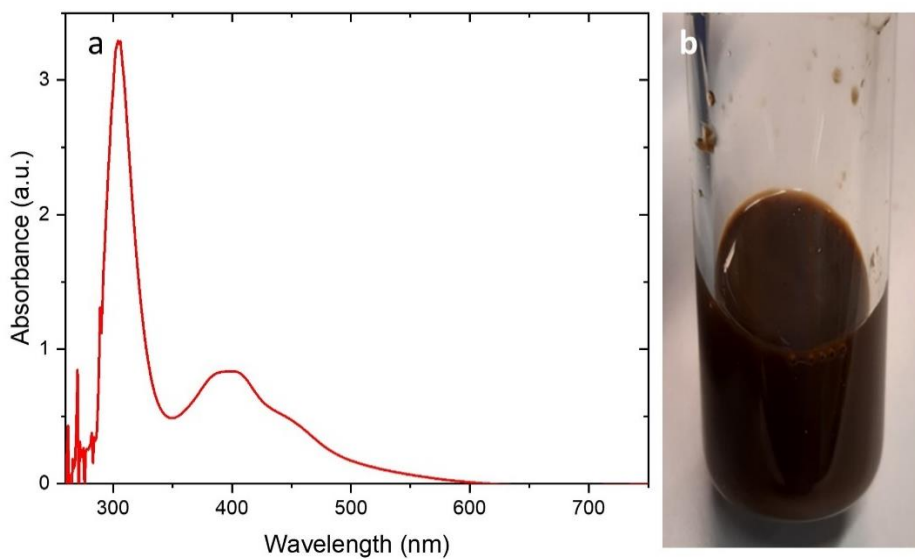


**Figure 4-12:** a) UV-Vis spectra, and b) color of NC<sub>15</sub>

In another set of experiments, in order to investigate the effect of MW power on the formation of CA/Cu-O<sub>x</sub> NPs, the experiment was designed using copper (II) sulfate pentahydrate, L-ascorbic acid, and polymer at various MW powers of 40, 60, and 80 W. As can be seen in **Figure 4-13d**, in samples synthesized using MW power of 40 W (NC<sub>16</sub>), and 60 W (NC<sub>17</sub>), peaks at 300, 400, and a shoulder at 560 nm indicate the formation of  $\text{CuO}$ ,  $\text{CuO}_2$ , and CuNPs, respectively. Thus, the formation of Cu NPs beside copper oxide NPs happened. However, for NC<sub>18</sub>, there were peaks at 300 and 400 nm which show the formation of  $\text{Cu}_2\text{O}$  and  $\text{CuO}$  (**Figure 4-13d**) and as a result, there were no Cu NPs in NC<sub>18</sub> provided using MW power of 80 W. Also, the color of the samples shown in **Figures 4-13a, b, and c** is proof of the results obtained by UV-Vis analysis for NC<sub>16</sub>, NC<sub>17</sub>, and NC<sub>18</sub>, respectively.

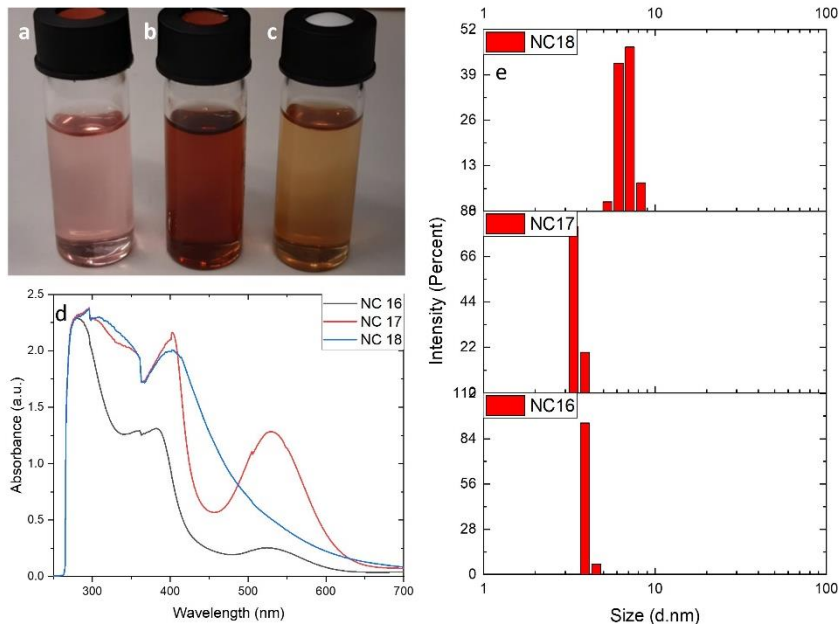


**Figure 4-13:** Color change of a) NC<sub>16</sub>, b) NC<sub>17</sub>, c) NC<sub>18</sub>, d) their UV-Vis spectra, and e) DLS results.

To investigate the hydrodynamic size of the Cu NPs in the utilized polymer matrix, DLS measurement, as a complementary method to the UV-vis, and also an effectual technique for measurement of particle size was performed on freshly prepared NC<sub>16</sub>, NC<sub>17</sub>, and NC<sub>18</sub> (**Figure 4-13e**). The hydrodynamic size of the Cu NPs for all three samples was less than 10 nm which indicates the advantage of the MWFS and the usage of polymers in the system. All synthesized Cu-O<sub>x</sub>NPs which are embedded inside the CA polymer are smaller than 10 nm.

After the interpretation of the results obtained by characterization of the samples, the NC<sub>17</sub> was chosen for further testing and making a film. The sample was drop-cast on the glass and left inside the desiccator for further use.

The crystallinity of the NCs was studied through XRD analysis. The related patterns are given in **Figure 4-14**. The x-ray diffraction (XRD) pattern of as-received CA approved the semi-crystalline structure of it which has two halos at approximately 18, and 20.7, attributed to (101) and (020) planes. It can be noticed that the amorphous peak area of as received CA is meaningfully larger than that of NC<sub>17</sub>. Also, as-received CA displayed three small intensive peaks which are at 2θ: 9, 10, and 13. Therefore, the CA material is comprised of crystalline and amorphous blocks. The peak at 20.7 proposed that CA has mostly amorphous features <sup>150</sup>. Noteworthy is the fact that the intensity of XRD peaks related to the CA decreased in the NC<sub>17</sub>, therefore representing the efficacious integration of CuNPs with CA matrices. The presence of CuO is analyzed by five distinctive peaks located at *ca.* 32, 35, 40, 54, and 58, attributed to

[110], [002], [200], [020], and [202] lattice planes<sup>151</sup>. Regarding Cu, peaks at wavelengths 44, and 50, 75 are related to [111], [200], and [220] suggesting the presence of small crystallites<sup>152</sup>. The peak corresponded to [022], and [220] lattice plane of CuO were not observed due to the overlapping peaks related to the lattice [220] of Cu.

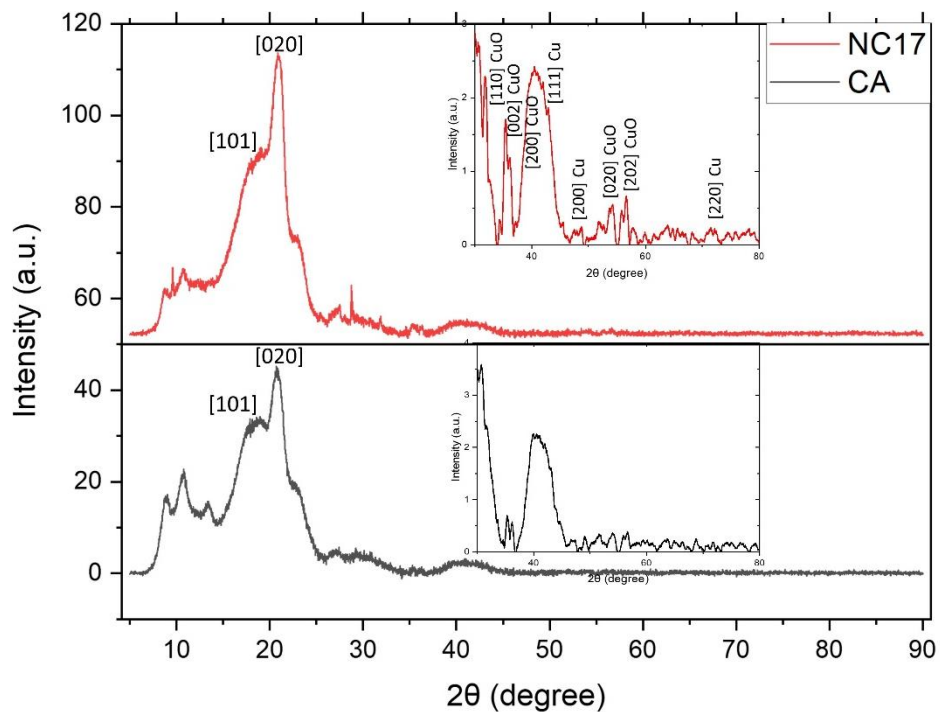


**Figure 4-14:** XRD patterns of the as-received CA, and NC<sub>17</sub>.

The analysis of functional groups of CA and possible alterations in their IR active modes after integration with Cu-O<sub>x</sub>NPs can be evaluated by FTIR (**Figure 4-15**). The incorporation of polymer with synthesized NPs results in alteration in features of a peak such as intensity and wavelength. There is a wide band at *ca.* 3490 cm<sup>-1</sup> related to the stretching of intermolecular hydrogen bonds of hydroxyl groups (-OH)<sup>153</sup>. After the formation of CuO<sub>x</sub>NPs in CA, the peaks at 2926.44 cm<sup>-1</sup> and 1657.23 cm<sup>-1</sup> were observed in CA which is related to the stretching of -CH- of methyl groups (-CH<sub>3</sub>)<sup>154</sup> and the carbonyl group (C=O) stretching vibration<sup>155</sup> shifted to the wavenumber of 2934.64 cm<sup>-1</sup>, and 1663.75 cm<sup>-1</sup> (with lower energy) in FTIR spectrum of NC<sub>17</sub>. In contrast, 1505.68 was shifted to a lower wavenumber (~1500.34 cm<sup>-1</sup>) located in a higher energy region. The overlapping of peaks at a wavenumber of 1385.12 cm<sup>-1</sup> signifies the successful incorporation of CuO<sub>x</sub> ions and CA polymer during the developed synthesis process. Also, another ~2 cm<sup>-1</sup> decrease was noticed at the wavelength of the band located at 1253.39 cm<sup>-1</sup> which corresponded to ‘C-O-C’ anti-symmetric stretching vibrations of ester groups. There was no change in the wavelength of the peak at 1090.69 cm<sup>-1</sup> which represented -C-OH stretching vibration. The integration of -C-O stretching and -CH<sub>2</sub>- rocking

vibrations in CA results in an absorption peak at  $866.64\text{ cm}^{-1}$  which shifted to the region of high energy by  $\sim 2\text{ cm}^{-1}$ .

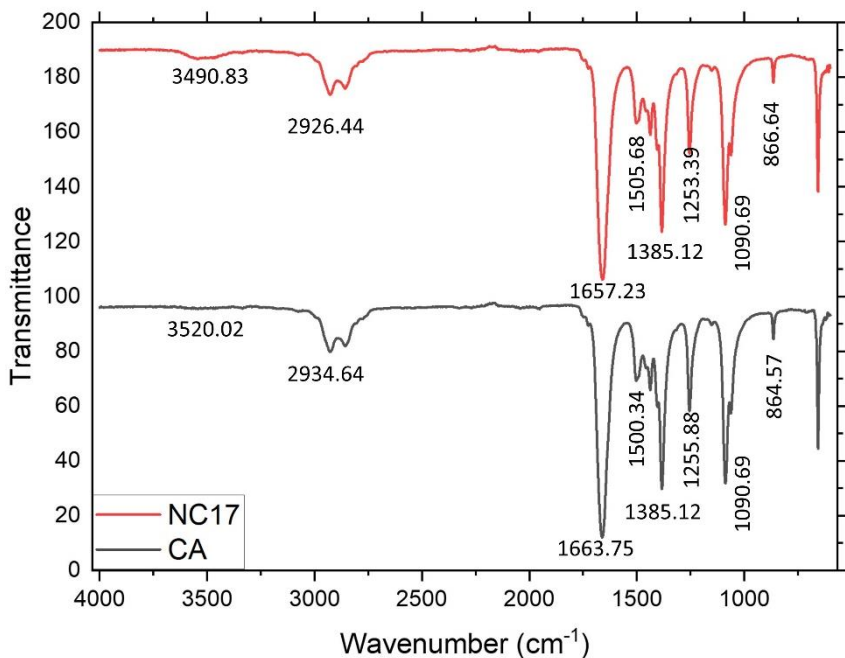


**Figure 4-15:** FTIR spectrum of CA film and  $\text{NC}_{17}$  film.

#### 4.4 Conclusion

Firstly, the synthesis of PA11-CuOx NCs was tried in the MWFS system. We encountered difficulties such as low solubility of PA11 in organic solvents and blockage of the fluidic system due to the high rate of nucleation in a fluidic system caused by  $\text{NaBH}_4$ . As a result, we looked for another biopolymer as an alternative to PA11. After selecting CA as a polymer, CA-Cu NCs with NPs less than 10 nm were continuously synthesized in a DMF as an organic solvent with the only use of L-ascorbic acid as a RA within  $\sim 15$  minutes at a MW power of 60 W using MWFS. A dual syringe was successfully installed for the injection of precursors. The MW power, the concentration of precursor and polymer, and also their FR has the main role to play in changing the size of CuNPs. Due to agglomeration and fast nucleation of NPs, we optimized FR ratios of precursor to the system. The optimum parameters are 0.03 M of copper (II) sulfate pentahydrate (premixed with 0.06 M of L-ascorbic acid in DMF) and CA in DMF (55 mg/ml) with FRs of 0.1 and 0.5 ml/min, respectively. The optimum MW was selected as 60 W with a temperature of  $40\text{ }^\circ\text{C}$ . This optimized assay resulted in uniformly distributed CuNPs with an average particle diameter of less than 10 nm. Increasing the MW power from 40 W to 80 W resulted in bigger NPs. However, in MW-assisted batch synthesis at a low temperature, no particle formed. The proposed MW- promoted continuous flow system can be

deemed an upscalable, reproducible, low-cost, and energy-efficient synthesis route for manufacturing polymeric NCs.

## Chapter 5: CONCLUSION

This thesis focused on the design and synthesis of green NSs and their antimicrobial applications. Chapter 2 described a facile green synthesis of AgNPs, as a possible alternative to other time-taking and energy-ineffective methods, by efficient reduction of Ag ion using *Chlorella vulgaris*, as both reducing and stabilizing agents. Several functional groups that existed in *Chlorella vulgaris* are responsible for the synthesis. Instead of other time-taking and costly energy sources, MI was used as an abundant energy source. Mostly spherical NPs with the size of 1 to 50 nm and (an average=24 nm) were scanned by SEM and TEM analyses. In addition, the considerable inhibition effect of the produced NP against various types of bacteria was signified. In future plans, other green RAs along with *Chlorella vulgaris* can be studied in the formation of AgNPs with higher stability. Since *Chlorella vulgaris* can act as both a reducing and stabilizing agent, the synthesis of other MNPs can also be examined. Also, the autoclave can be assessed as an alternative energy supply to MI to find out its efficiency. In addition to the substantial improvement in nanotechnology, the more innovative vision of nanoscience includes the more pervasive application of NPs in biomedical and pharmaceutical. In chapter 3, the MWFS was, for the first time, developed as an effective technique in the continuous production of polymeric NCs. Thus, PA6 NCs with evenly distributed AgNPs ( $\sim 2.59 \pm 0.64$  nm) were synthesized within  $\sim 2$  min below 55 °C using FA as a green solvent. However, the CHFS synthesized AgNPs with the size of  $\sim 50$  nm under identical experimental conditions. Furthermore, the size of AgNP was successfully optimized by changing the MWPs, the FR ratios, and the reagent concentrations as reaction parameters. Thus, an increase in the concentration of PA6 led to smaller AgNPs. Small AgNPs with a narrow size distribution (FWHM  $\sim 60$  for NC<sub>MWF64</sub>) were obtained at a high MWP (40 W) but large AgNPs with a broad size distribution (FWHM  $\sim 80$  for NC<sub>MWF52</sub>) at a low MWP (10 W). The size of AgNP affects polymer crystallinity, and the  $\gamma$ -phase PA6 (pseudo-hexagonal crystal) was dominant in the presence of small NPs. The antibacterial activity of the NC<sub>MWF64</sub> (particle size  $\sim 3$  nm) film towards bacteria was excellent in comparison with NC<sub>CHF2</sub> (particle size  $\sim 50$  nm). The antibacterial evaluation tests with *Escherichia coli* (Gram-negative), *Staphylococcus aureus* (Gram-positive), and *Pseudomonas aeruginosa* (Gram-negative) showed that the antibacterial rate of NC<sub>MWF64</sub> was approximately 98.40, 98.91, and 98.93%, respectively. In conclusion, the obtained results proved the superiority of the MWFS and defined it as a novel energy-efficient green, and sustainable synthesis method for the continuous formation of polymeric NCs. Also,

the MWFS can be scaled up and utilized for the preparation of the other polymer-matrix NCs. Finally, chapter 4 involved the production of polymeric NCs with CuO<sub>x</sub>NPs. Initially, we investigated the synthesis of CuOx NCs in the PA11 matrix using the MWFS system. However, the low solubility of PA11 in organic solvents was only one of the problems that we encountered while using this polymer. Thus, CA biopolymer was chosen as an alternative to PA11. Then, in our MWFS, we continuously produced CA-Cu NCs with NPs less than 10 nm in a DMF using L-ascorbic acid within ~15 minutes at 40 °C. The MW power, the concentration of precursor, and the polymer were all optimized. The optimum parameters are 0.03 M of copper (II) sulfate pentahydrate (premixed with 0.06 M of L-ascorbic acid in DMF) and CA in DMF (55 mg/ml) with FRs of 0.1 and 0.5 ml/min, respectively. The optimum MW was selected as 60 W. This optimization led to the formation of uniformly distributed CuNPs with an average particle diameter of less than 10 nm in CA polymer. In MW-assisted batch synthesis at a low temperature, no particle formed. The developed MWFS can pave the way for upscalable, reproducible, low-priced, and environmentally friendly manufacturing of polymeric NCs. All these studies confirmed that these green NSs have specific features which make them ideal for antimicrobial applications and also even can be preferred for other applications such as sensing, plasmonic, and coating in the future.

## REFERENCES

1. Manjunath HM, Joshi CG. Characterization, antioxidant and antimicrobial activity of silver nanoparticles synthesized using marine endophytic fungus- *Cladosporium cladosporioides*. *Process Biochem* [Internet] 2019; 82:199–204. Available from: <https://linkinghub.elsevier.com/retrieve/pii/S1359511318316994>
2. Pugazhendhi A, Prabakar D, Jacob JM, Karuppusamy I, Saratale RG. Synthesis and characterization of silver nanoparticles using *Gelidium amansii* and its antimicrobial property against various pathogenic bacteria. *Microb Pathog* [Internet] 2018; 114:41–5. Available from: <https://doi.org/10.1016/j.micpath.2017.11.013>
3. Shukla AK, Iravani S. Metallic nanoparticles: green synthesis and spectroscopic characterization. *Environ Chem Lett* [Internet] 2017; 15:223–31. Available from: <http://link.springer.com/10.1007/s10311-017-0618-2>
4. Saravanan M, Arokiyaraj S, Lakshmi T, Pugazhendhi A. Synthesis of silver nanoparticles from *Phenerochaete chrysosporium* (MTCC-787) and their antibacterial activity against human pathogenic bacteria. *Microb Pathog* [Internet] 2018; 117:68–72. Available from: <https://doi.org/10.1016/j.micpath.2018.02.008>
5. Mandal AK. Silver Nanoparticles as Drug Delivery Vehicle against Infections. *Glob J Nanomedicine* 2017; 3:1–4.
6. Sri V, Pugazhendhi A, Gopalakrishnan K. Biofabrication and characterization of silver nanoparticles using aqueous extract of seaweed *Enteromorpha compressa* and its biomedical properties. *Biotechnol Reports* [Internet] 2017; 14:1–7. Available from: <http://dx.doi.org/10.1016/j.btre.2017.02.001>
7. Safi C, Zebib B, Merah O, Pontalier P-Y, Vaca-Garcia C. Morphology, composition, production, processing and applications of *Chlorella vulgaris*: A review. *Renew Sustain Energy Rev* [Internet] 2014; 35:265–78. Available from: <https://linkinghub.elsevier.com/retrieve/pii/S1364032114002342>
8. Přibyl P, Cepák V, Zachleder V. Production of lipids in 10 strains of *Chlorella* and *Parachlorella*, and enhanced lipid productivity in *Chlorella vulgaris*. *Appl Microbiol Biotechnol* [Internet] 2012; 94:549–61. Available from: <http://link.springer.com/10.1007/s00253-012-3915-5>

9. Rafique M, Sadaf I, Rafique MS, Tahir MB. A review on green synthesis of silver nanoparticles and their applications. *Artif Cells, Nanomedicine Biotechnol* [Internet] 2017; 45:1272–91. Available from: <https://doi.org/10.1080/21691401.2016.1241792>
10. Iravani S. Green synthesis of metal nanoparticles using plants. *Green Chem* [Internet] 2011; 13:2638. Available from: <http://xlink.rsc.org/?DOI=c1gc15386b>
11. Taghizadeh SM, Morowvat MH, Negahdaripour M, Ebrahiminezhad A, Ghasemi Y. Biosynthesis of Metals and Metal Oxide Nanoparticles Through Microalgal Nanobiotechnology: Quality Control Aspects. *Bionanoscience* 2021; 11:209–26.
12. Długosz O, Banach M. Continuous synthesis of metal and metal oxide nanoparticles in microwave reactor. *Colloids Surfaces A Physicochem Eng Asp* [Internet] 2020; 606:125453. Available from: <https://doi.org/10.1016/j.colsurfa.2020.125453>
13. Jelinek R. *Nanoparticles*. Walter de Gruyter GmbH & Co KG; 2015.
14. Xia Y, Xiong Y, Lim B, Skrabalak SE. Shape-Controlled Synthesis of Metal Nanocrystals: Simple Chemistry Meets Complex Physics? *Angew Chemie Int Ed* [Internet] 2009; 48:60–103. Available from:  
<https://onlinelibrary.wiley.com/doi/10.1002/anie.200802248>
15. Zare EN, Zheng X, Makvandi P, Gheybi H, Sartorius R, Yiu CKY, Adeli M, Wu A, Zarabi A, Varma RS, et al. Nonspherical Metal-Based Nanoarchitectures: Synthesis and Impact of Size, Shape, and Composition on Their Biological Activity. *Small* [Internet] 2021; 17:2007073. Available from:  
<https://onlinelibrary.wiley.com/doi/10.1002/smll.202007073>
16. Sarkar S, Guibal E, Quignard F, SenGupta AK. Polymer-supported metals and metal oxide nanoparticles: synthesis, characterization, and applications. *J Nanoparticle Res* [Internet] 2012; 14:715. Available from: <http://link.springer.com/10.1007/s11051-011-0715-2>
17. Tylkowski B, Trojanowska A, Nowak M, Marcinia L, Jastrzab R. Applications of silver nanoparticles stabilized and/or immobilized by polymer matrixes. *Phys Sci Rev* [Internet] 2017; 2. Available from:  
<https://www.degruyter.com/document/doi/10.1515/psr-2017-0024/html>
18. Rozilah A, Jaafar CNA, Sapuan SM, Zainol I, Ilyas RA. The Effects of Silver

- Nanoparticles Compositions on the Mechanical, Physiochemical, Antibacterial, and Morphology Properties of Sugar Palm Starch Biocomposites for Antibacterial Coating. *Polymers* (Basel) [Internet] 2020; 12:2605. Available from: <https://www.mdpi.com/2073-4360/12/11/2605>
19. Raza S, Ansari A, Siddiqui NN, Ibrahim F, Abro MI, Aman A. Biosynthesis of silver nanoparticles for the fabrication of non cytotoxic and antibacterial metallic polymer based nanocomposite system. *Sci Rep* [Internet] 2021; 11:10500. Available from: <https://www.nature.com/articles/s41598-021-90016-w>
20. Nair AS, Binoy NP, Ramakrishna S, Kurup TRR, Chan LW, Goh CH, Islam MR, Utschig T, Pradeep T. Organic-Soluble Antimicrobial Silver Nanoparticle–Polymer Composites in Gram Scale by One-Pot Synthesis. *ACS Appl Mater Interfaces* [Internet] 2009; 1:2413–9. Available from: <https://pubs.acs.org/doi/10.1021/am9005034>
21. Palza H. Antimicrobial Polymers with Metal Nanoparticles. *Int J Mol Sci* [Internet] 2015; 16:2099–116. Available from: <http://www.mdpi.com/1422-0067/16/1/2099>
22. Kumar R, Münstedt H. Silver ion release from antimicrobial polyamide/silver composites. *Biomaterials* [Internet] 2005; 26:2081–8. Available from: <https://linkinghub.elsevier.com/retrieve/pii/S014296120400506X>
23. E. Stodolak, A. Fraczek-Szczypta and M. Blazewicz. Polymer-Base Nanocomposite For Medical Application. *Composites* 2010; 10:323–328.
24. Guo L, Yuan W, Lu Z, Li CM. Polymer/nanosilver composite coatings for antibacterial applications. *Colloids Surfaces A Physicochem Eng Asp* [Internet] 2013; 439:69–83. Available from: <https://linkinghub.elsevier.com/retrieve/pii/S092777571200893X>
25. Kausar A. Polyurethane nanocomposite coatings: state of the art and perspectives. *Polym Int* [Internet] 2018; 67:1470–7. Available from: <https://onlinelibrary.wiley.com/doi/10.1002/pi.5616>
26. Savelyev Y, Gonchar A, Movchan B, Gornostay A, Vozianov S, Rudenko A, Rozhnova R, Travinskaya T. Antibacterial polyurethane materials with silver and copper nanoparticles. *Mater Today Proc* [Internet] 2017; 4:87–94. Available from: <https://linkinghub.elsevier.com/retrieve/pii/S2214785317301967>

27. Yağmur HK, Kaya İ. Synthesis and characterization of poly(urethane)/silver composites via in situ polymerization. *Polym Compos* [Internet] 2021; 42:2704–16. Available from: <https://onlinelibrary.wiley.com/doi/10.1002/pc.26006>
28. Zahran M, Marei AH. Innovative natural polymer metal nanocomposites and their antimicrobial activity. *Int J Biol Macromol* [Internet] 2019; 136:586–96. Available from: <https://linkinghub.elsevier.com/retrieve/pii/S0141813019311432>
29. Xu P, Han X, Zhang B, Du Y, Wang H-L. Multifunctional polymer–metal nanocomposites via direct chemical reduction by conjugated polymers. *Chem Soc Rev* [Internet] 2014; 43:1349–60. Available from: <http://xlink.rsc.org/?DOI=C3CS60380F>
30. Zare Y, Shabani I. Polymer/metal nanocomposites for biomedical applications. *Mater Sci Eng C* [Internet] 2016; 60:195–203. Available from: <https://linkinghub.elsevier.com/retrieve/pii/S0928493115305543>
31. Faupel F, Zaporotchenko V, Strunskus T, Elbahri M. Metal-Polymer Nanocomposites for Functional Applications. *Adv Eng Mater* [Internet] 2010; 12:1177–90. Available from: <https://onlinelibrary.wiley.com/doi/10.1002/adem.201000231>
32. Abou-Yousef H, Saber E, Abdel-Aziz MS, Kamel S. Efficient alternative of antimicrobial nanocomposites based on cellulose acetate/Cu-NPs. *Soft Mater* [Internet] 2018; 16:141–50. Available from: <https://www.tandfonline.com/doi/full/10.1080/1539445X.2018.1457540>
33. Saleem Q, Torabfam M, Fidan T, Kurt H, Yüce M, Clarke N, Bayazit MK. Microwave-Promoted Continuous Flow Systems in Nanoparticle Synthesis - A Perspective. *ACS Sustain Chem Eng* 2021; 9:9988–10015.
34. Herzog B, Kohan MI, Mestemacher SA, Pagilagan RU, Redmond K. Polyamides [Internet]. In: Ullmann's Encyclopedia of Industrial Chemistry. Weinheim, Germany: Wiley-VCH Verlag GmbH & Co. KGaA; 2013. Available from: [https://onlinelibrary.wiley.com/doi/10.1002/14356007.a21\\_179.pub3](https://onlinelibrary.wiley.com/doi/10.1002/14356007.a21_179.pub3)
35. Rimdusit S, Jingjid S, Damrongsakkul S, Tiptipakorn S, Takeichi T. Biodegradability and property characterizations of Methyl Cellulose: Effect of nanocompositing and chemical crosslinking. *Carbohydr Polym* [Internet] 2008; 72:444–55. Available from: <https://linkinghub.elsevier.com/retrieve/pii/S0144861707004869>

36. Park H-M, Misra M, Drzal LT, Mohanty AK. “Green” Nanocomposites from Cellulose Acetate Bioplastic and Clay: Effect of Eco-Friendly Triethyl Citrate Plasticizer. *Biomacromolecules* [Internet] 2004; 5:2281–8. Available from: <https://pubs.acs.org/doi/10.1021/bm049690f>
37. Salah I, Parkin IP, Allan E. Copper as an antimicrobial agent: recent advances. *RSC Adv* [Internet] 2021; 11:18179–86. Available from: <http://xlink.rsc.org/?DOI=D1RA02149D>
38. Syafiuddin A, Salmiati, Salim MR, Beng Hong Kueh A, Hadibarata T, Nur H. A Review of Silver Nanoparticles: Research Trends, Global Consumption, Synthesis, Properties, and Future Challenges. *J Chinese Chem Soc* [Internet] 2017; 64:732–56. Available from: <http://doi.wiley.com/10.1002/jccs.201700067>
39. Sreekanth T, Debbie CC. Metal Nanoparticles: Synthesis and Applications in Pharmaceutical Sciences. 2018.
40. Shankar T, Karthiga P, Swarnalatha K, Rajkumar K. Green synthesis of silver nanoparticles using Capsicum frutescens and its intensified activity against *E. coli*. *Resour Technol* [Internet] 2017; 3:303–8. Available from: <http://linkinghub.elsevier.com/retrieve/pii/S2405653716301373>
41. Abdel-Raouf N, Al-Enazi NM, Ibraheem IBM, Alharbi RM, Alkhulaifi MM. Biosynthesis of silver nanoparticles by using of the marine brown alga *Padina pavonia* and their characterization. *Saudi J Biol Sci* [Internet] 2019; 26:1207–15. Available from: <https://doi.org/10.1016/j.sjbs.2018.01.007>
42. Ahmed S, Annu, Ikram S, Yudha S. Biosynthesis of gold nanoparticles: A green approach. *J Photochem Photobiol B Biol* [Internet] 2016; 161:141–53. Available from: <http://dx.doi.org/10.1016/j.jphotobiol.2016.04.034>
43. Al-Bahrani R, Raman J, Lakshmanan H, Hassan AA, Sabaratnam V. Green synthesis of silver nanoparticles using tree oyster mushroom *Pleurotus ostreatus* and its inhibitory activity against pathogenic bacteria. *Mater Lett* [Internet] 2017; 186:21–5. Available from: <http://dx.doi.org/10.1016/j.matlet.2016.09.069>
44. Costa Silva LP, Pinto Oliveira J, Keijok WJ, da Silva AR, Aguiar AR, Guimarães MCC, Ferraz CM, Araújo JV, Tobias FL, Braga FR. Extracellular biosynthesis of silver nanoparticles using the cell-free filtrate of nematophagous fungus *Duddingtonia*

- flagrans. *Int J Nanomedicine* [Internet] 2017; Volume 12:6373–81. Available from: <https://www.dovepress.com/extracellular-biosynthesis-of-silver-nanoparticles-using-the-cell-free-peer-reviewed-article-IJN>
45. Kim D, Saratale RG, Shinde S, Syed A, Ameen F, Ghodake G. Green synthesis of silver nanoparticles using *Laminaria japonica* extract: Characterization and seedling growth assessment. *J Clean Prod* [Internet] 2018; 172:2910–8. Available from: <https://doi.org/10.1016/j.jclepro.2017.11.123>
46. Neethu S, Midhun SJ, Radhakrishnan EK, Jyothis M. Green synthesized silver nanoparticles by marine endophytic fungus *Penicillium polonicum* and its antibacterial efficacy against biofilm forming, multidrug-resistant *Acinetobacter baumanii*. *Microb Pathog* [Internet] 2018; 116:263–72. Available from: <https://doi.org/10.1016/j.micpath.2018.01.033>
47. Mohanta Y, Nayak D, Biswas K, Singdevsachan S, Abd\_Allah E, Hashem A, Alqarawi A, Yadav D, Mohanta T. Silver Nanoparticles Synthesized Using Wild Mushroom Show Potential Antimicrobial Activities against Food Borne Pathogens. *Molecules* [Internet] 2018; 23:655. Available from: <http://www.mdpi.com/1420-3049/23/3/655>
48. Hoseinnejad M, Jafari SM, Katouzian I. Inorganic and metal nanoparticles and their antimicrobial activity in food packaging applications. *Crit Rev Microbiol* [Internet] 2018; 44:161–81. Available from: <https://doi.org/10.1080/1040841X.2017.1332001>
49. Alsammarraie FK, Wang W, Zhou P, Mustapha A, Lin M. Green synthesis of silver nanoparticles using turmeric extracts and investigation of their antibacterial activities. *Colloids Surfaces B Biointerfaces* [Internet] 2018; 171:398–405. Available from: <https://doi.org/10.1016/j.colsurfb.2018.07.059>
50. Veisi H, Azizi S, Mohammadi P. Green synthesis of the silver nanoparticles mediated by *Thymbra spicata* extract and its application as a heterogeneous and recyclable nanocatalyst for catalytic reduction of a variety of dyes in water. *J Clean Prod* [Internet] 2018; 170:1536–43. Available from: <https://doi.org/10.1016/j.jclepro.2017.09.265>
51. Raja S, Ramesh V, Thivaharan V. Green biosynthesis of silver nanoparticles using *Calliandra haematocephala* leaf extract, their antibacterial activity and hydrogen

- peroxide sensing capability. *Arab J Chem* [Internet] 2017; 10:253–61. Available from: <http://dx.doi.org/10.1016/j.arabjc.2015.06.023>
52. de Aragão AP, de Oliveira TM, Quelemes PV, Perfeito MLG, Araújo MC, Santiago J de AS, Cardoso VS, Quaresma P, de Souza de Almeida Leite JR, da Silva DA. Green synthesis of silver nanoparticles using the seaweed *Gracilaria birdiae* and their antibacterial activity. *Arab J Chem* 2016; :4182–8.
53. Bagherzade G, Tavakoli MM, Namaei MH. Green synthesis of silver nanoparticles using aqueous extract of saffron (*Crocus sativus L.*) wastages and its antibacterial activity against six bacteria. *Asian Pac J Trop Biomed* [Internet] 2017; 7:227–33. Available from: <http://dx.doi.org/10.1016/j.apjtb.2016.12.014>
54. Arokiyaraj S, Vincent S, Saravanan M, Lee Y, Oh YK, Kim KH. Green synthesis of silver nanoparticles using *Rheum palmatum* root extract and their antibacterial activity against *Staphylococcus aureus* and *Pseudomonas aeruginosa*. *Artif Cells, Nanomedicine Biotechnol* 2017; 45:372–9.
55. Kasithevar M, Saravanan M, Prakash P, Kumar H, Ovais M, Barabadi H, Shinwari ZK. Green synthesis of silver nanoparticles using *Alysicarpus monilifer* leaf extract and its antibacterial activity against MRSA and CoNS isolates in HIV patients . *J Interdiscip Nanomedicine* 2017; 2:131–41.
56. Francis S, Joseph S, Koshy EP, Mathew B. Microwave assisted green synthesis of silver nanoparticles using leaf extract of *elephantopus scaber* and its environmental and biological applications. *Artif Cells, Nanomedicine, Biotechnol* [Internet] 2018; 46:795–804. Available from: <https://www.tandfonline.com/doi/full/10.1080/21691401.2017.1345921>
57. Rao B, Tang RC. Green synthesis of silver nanoparticles with antibacterial activities using aqueous *Eriobotrya japonica* leaf extract. *Adv Nat Sci Nanosci Nanotechnol* 2017; 8.
58. Akther T, Mathipi V, Kumar NS, Davoodbasha M, Srinivasan H. Fungal-mediated synthesis of pharmaceutically active silver nanoparticles and anticancer property against A549 cells through apoptosis. *Environ Sci Pollut Res* 2019; 26:13649–57.
59. Ghiuță I, Cristea D, Croitoru C, Kost J, Wenkert R, Vyrides I, Anayiotos A, Munteanu D. Characterization and antimicrobial activity of silver nanoparticles, biosynthesized

- using *Bacillus* species. *Appl Surf Sci* [Internet] 2018; 438:66–73. Available from: <https://linkinghub.elsevier.com/retrieve/pii/S0169433217328118>
60. Saravanan M, Barik SK, MubarakAli D, Prakash P, Pugazhendhi A. Synthesis of silver nanoparticles from *Bacillus brevis* (NCIM 2533) and their antibacterial activity against pathogenic bacteria. *Microb Pathog* [Internet] 2018; 116:221–6. Available from: <https://doi.org/10.1016/j.micpath.2018.01.038>
61. Składanowski M, Wypij M, Laskowski D, Golińska P, Dahm H, Rai M. Silver and gold nanoparticles synthesized from *Streptomyces* sp. isolated from acid forest soil with special reference to its antibacterial activity against pathogens. *J Clust Sci* 2017; 28:59–79.
62. AbdelRahim K, Mahmoud SY, Ali AM, Almaary KS, Mustafa AE-ZMA, Husseiny SM. Extracellular biosynthesis of silver nanoparticles using *Rhizopus stolonifer*. *Saudi J Biol Sci* [Internet] 2017; 24:208–16. Available from: <http://dx.doi.org/10.1016/j.sjbs.2016.02.025>
63. Wang C, Kim YJ, Singh P, Mathiyalagan R, Jin Y, Yang DC. Green synthesis of silver nanoparticles by *Bacillus methylotrophicus*, and their antimicrobial activity. *Artif Cells, Nanomedicine Biotechnol* 2016; 44:1127–32.
64. Jo JH, Singh P, Kim YJ, Wang C, Mathiyalagan R, Jin CG, Yang DC. *Pseudomonas deceptioensis* DC5-mediated synthesis of extracellular silver nanoparticles. *Artif Cells, Nanomedicine Biotechnol* 2016; 44:1576–81.
65. Singh P, Kim YJ, Wang C, Mathiyalagan R, Yang DC. *Weissella oryzae* DC6-facilitated green synthesis of silver nanoparticles and their antimicrobial potential. *Artif Cells, Nanomedicine Biotechnol* 2016; 44:1569–75.
66. Wang L, He D, Gao S, Wang D, Xue B, Yokoyama K. Biosynthesis of silver nanoparticles by the fungus *Arthroderma fulvum* and its antifungal activity against genera of *Candida*, *Aspergillus* and *Fusarium*. *Int J Nanomedicine* [Internet] 2016; :1899. Available from: <https://www.dovepress.com/biosynthesis-of-silver-nanoparticles-by-the-fungus-arthroderma-fulvum--peer-reviewed-article-IJN>
67. Singh P, Kim YJ, Singh H, Mathiyalagan R, Wang C, Yang DC. Biosynthesis of Anisotropic Silver Nanoparticles by *Bhargavaea indica* and Their Synergistic Effect with Antibiotics against Pathogenic Microorganisms. *J Nanomater* [Internet] 2015;

2015:1–10. Available from: <http://www.hindawi.com/journals/jnm/2015/234741/>

68. Elbeshehy EKF, Elazzazy AM, Aggelis G. Silver nanoparticles synthesis mediated by new isolates of *Bacillus* spp., nanoparticle characterization and their activity against Bean Yellow Mosaic Virus and human pathogens. *Front Microbiol* [Internet] 2015; 6:1–13. Available from:  
[http://www.frontiersin.org/Antimicrobials%2C\\_Resistance\\_and\\_Chemotherapy/10.3389/fmicb.2015.00453/abstract](http://www.frontiersin.org/Antimicrobials%2C_Resistance_and_Chemotherapy/10.3389/fmicb.2015.00453/abstract)
69. Soni N, Prakash S. Antimicrobial and mosquitocidal activity of microbial synthesized silver nanoparticles. *Parasitol Res* 2015; 114:1023–30.
70. Waghmare SR, Mulla MN, Marathe SR, Sonawane KD. Ecofriendly production of silver nanoparticles using *Candida utilis* and its mechanistic action against pathogenic microorganisms. *3 Biotech* [Internet] 2015; 5:33–8. Available from:  
<http://link.springer.com/10.1007/s13205-014-0196-y>
71. Kathiraven T, Sundaramanickam A, Shanmugam N, Balasubramanian T. Green synthesis of silver nanoparticles using marine algae *Caulerpa racemosa* and their antibacterial activity against some human pathogens. *Appl Nanosci* [Internet] 2015; 5:499–504. Available from: <http://link.springer.com/10.1007/s13204-014-0341-2>
72. Mahajan A, Arya A, Chundawat TS. Green synthesis of silver nanoparticles using green alga (*Chlorella vulgaris*) and its application for synthesis of quinolines derivatives. *Synth Commun* [Internet] 2019; 49:1926–37. Available from:  
<https://doi.org/10.1080/00397911.2019.1610776>
73. Torabfam M, Jafarizadeh MH. Microwave-enhanced silver nanoparticle synthesis using chitosan biopolymer: Optimization of the process conditions and evaluation of their characteristics. *Green Process Synth* 2018; 7:530–7.
74. Hussain I, Singh NB, Singh A, Singh H, Singh SC. Green synthesis of nanoparticles and its potential application. *Biotechnol Lett* [Internet] 2016; 38:545–60. Available from: <http://link.springer.com/10.1007/s10529-015-2026-7>
75. Parveen M, Ahmad F, Malla AM, Azaz S. Microwave-assisted green synthesis of silver nanoparticles from *Fraxinus excelsior* leaf extract and its antioxidant assay. *Appl Nanosci* [Internet] 2016; 6:267–76. Available from: <http://dx.doi.org/10.1007/s13204-015-0433-7>

76. El-naggar ME, Shaheen TI, Fouda MMG, Hebeish AA. Eco-friendly microwave-assisted green and rapid synthesis of well-stabilized gold and core – shell silver – gold nanoparticles. *Carbohydr Polym* [Internet] 2016; 136:1128–36. Available from: <http://dx.doi.org/10.1016/j.carbpol.2015.10.003>
77. Palchik O, Zhu J, Gedanken A. Microwave assisted preparation of binary oxide nanoparticles. *J Mater Chem* [Internet] 2000; 10:1251–4. Available from: <http://xlink.rsc.org/?DOI=a908795h>
78. Dilek (Yalcin) Duygu. Fourier transform infrared (FTIR) spectroscopy for identification of Chlorella vulgaris Beijerinck 1890 and Scenedesmus obliquus (Turpin) Kützing 1833. *AFRICAN J Biotechnol* [Internet] 2012; 11:3817–24. Available from: <http://www.academicjournals.org/ajb/abstracts/abs2012/23Feb/Duygu et al.htm>
79. Slavin YN, Asnis J, Häfeli UO, Bach H. Metal nanoparticles: Understanding the mechanisms behind antibacterial activity. *J Nanobiotechnology* 2017; 15:1–20.
80. Horikoshi S, Serpone N. Role of microwaves in heterogeneous catalytic systems. *Catal Sci Technol* [Internet] 2014; 4:1197. Available from: <http://xlink.rsc.org/?DOI=c3cy00753g>
81. Chikan V, McLaurin E. Rapid Nanoparticle Synthesis by Magnetic and Microwave Heating. *Nanomaterials* [Internet] 2016; 6:85. Available from: <http://www.mdpi.com/2079-4991/6/5/85>
82. Dahal N, García S, Zhou J, Humphrey SM. Beneficial Effects of Microwave-Assisted Heating versus Conventional Heating in Noble Metal Nanoparticle Synthesis. *ACS Nano* [Internet] 2012; 6:9433–46. Available from: <https://pubs.acs.org/doi/10.1021/nn3038918>
83. Studart AR, Amstad E, Gauckler LJ. Colloidal Stabilization of Nanoparticles in Concentrated Suspensions. *Langmuir* [Internet] 2007; 23:1081–90. Available from: <https://pubs.acs.org/doi/10.1021/la062042s>
84. Kang H, Buchman JT, Rodriguez RS, Ring HL, He J, Bantz KC, Haynes CL. Stabilization of Silver and Gold Nanoparticles: Preservation and Improvement of Plasmonic Functionalities. *Chem Rev* [Internet] 2019; 119:664–99. Available from: <https://pubs.acs.org/doi/10.1021/acs.chemrev.8b00341>

85. Rudman KK, Hosseini S, Chatterjee K, Johnson B, Skrabalak SE. Sonoelectrosynthesis of monodisperse metal nanoparticles. *Nanoscale* [Internet] 2022; 14:6471–9. Available from: <http://xlink.rsc.org/?DOI=D2NR00167E>
86. Balazs AC, Emrick T, Russell TP. Nanoparticle Polymer Composites: Where Two Small Worlds Meet. *Science* (80- ) [Internet] 2006; 314:1107–10. Available from: <https://www.science.org/doi/10.1126/science.1130557>
87. Mackay ME, Tuteja A, Duxbury PM, Hawker CJ, Van Horn B, Guan Z, Chen G, Krishnan RS. General Strategies for Nanoparticle Dispersion. *Science* (80- ) [Internet] 2006; 311:1740–3. Available from: <https://www.science.org/doi/10.1126/science.1122225>
88. Javadi A, Zhao J, Cao C, Pozuelo M, Yang Y, Hwang I, Lin TC, Li X. Stretching Micro Metal Particles into Uniformly Dispersed and Sized Nanoparticles in Polymer. *Sci Rep* [Internet] 2017; 7:7098. Available from: <https://www.nature.com/articles/s41598-017-07788-3>
89. Kamal A, Ashmawy M, S S, Algazzar AM, Elsheikh AH. Fabrication techniques of polymeric nanocomposites: A comprehensive review. *Proc Inst Mech Eng Part C J Mech Eng Sci* [Internet] 2022; 236:4843–61. Available from: <http://journals.sagepub.com/doi/10.1177/09544062211055662>
90. Qin S, Qiu S, Cui M, Dai Z, Zhao H, Wang L. Synthesis and properties of polyimide nanocomposite containing dopamine-modified graphene oxide. *High Perform Polym* [Internet] 2019; 31:331–40. Available from: <http://journals.sagepub.com/doi/10.1177/0954008318768857>
91. Costa NJS, Rossi LM. Synthesis of supported metal nanoparticle catalysts using ligand assisted methods. *Nanoscale* [Internet] 2012; 4:5826. Available from: <http://xlink.rsc.org/?DOI=c2nr31165h>
92. Zhang R, Moon K, Lin W, Agar JC, Wong C-P. A simple, low-cost approach to prepare flexible highly conductive polymer composites by in situ reduction of silver carboxylate for flexible electronic applications. *Compos Sci Technol* [Internet] 2011; 71:528–34. Available from: <https://linkinghub.elsevier.com/retrieve/pii/S0266353811000297>
93. Guerrini L, Alvarez-Puebla R, Pazos-Perez N. Surface Modifications of Nanoparticles

- for Stability in Biological Fluids. *Materials* (Basel) [Internet] 2018; 11:1154. Available from: <http://www.mdpi.com/1996-1944/11/7/1154>
94. Ching Lau C, Kemal Bayazit M, Reardon PJT, Tang J. Microwave Intensified Synthesis: Batch and Flow Chemistry. *Chem Rec* [Internet] 2019; 19:172–87. Available from: <https://onlinelibrary.wiley.com/doi/10.1002/tcr.201800121>
95. Długosz O, Banach M. Inorganic nanoparticle synthesis in flow reactors – applications and future directions. *React Chem Eng* [Internet] 2020; 5:1619–41. Available from: <http://xlink.rsc.org/?DOI=D0RE00188K>
96. Bayazit MK, Cao E, Gavriilidis A, Tang J. A microwave promoted continuous flow approach to self-assembled hierarchical hematite superstructures. *Green Chem* [Internet] 2016; 18:3057–65. Available from: <http://xlink.rsc.org/?DOI=C5GC02245B>
97. Hallot G, Cagan V, Laurent S, Gomez C, Port M. A Greener Chemistry Process Using Microwaves in Continuous Flow to Synthesize Metallic Bismuth Nanoparticles. *ACS Sustain Chem Eng* [Internet] 2021; 9:9177–87. Available from: <https://pubs.acs.org/doi/10.1021/acssuschemeng.1c00396>
98. Zhu J-F, Zhu Y-J. Microwave-Assisted One-Step Synthesis of Polyacrylamide–Metal (M = Ag, Pt, Cu) Nanocomposites in Ethylene Glycol. *J Phys Chem B* [Internet] 2006; 110:8593–7. Available from: <https://pubs.acs.org/doi/10.1021/jp060488b>
99. Parida D, Simonetti P, Frison R, Bülbül E, Altenried S, Arroyo Y, Balogh-Michels Z, Caseri W, Ren Q, Hufenus R, et al. Polymer-assisted in-situ thermal reduction of silver precursors: A solventless route for silver nanoparticles-polymer composites. *Chem Eng J* [Internet] 2020; 389:123983. Available from: <https://linkinghub.elsevier.com/retrieve/pii/S1385894719333984>
100. Tangudom P, Wimolmala E, Prapagdee B, Sombatsompop N. Mechanical properties and antibacterial performance of PMMA toughened with acrylic rubber containing 2-hydroxypropyl-3-piperazinyl-quinoline carboxylic acid methacrylate (HPQM) and HPQM absorbed on TiO<sub>2</sub> particles. *Polym Test* [Internet] 2019; 79:106023. Available from: <https://linkinghub.elsevier.com/retrieve/pii/S0142941819310207>
101. Song KC, Lee SM, Park TS, Lee BS. Preparation of colloidal silver nanoparticles by chemical reduction method. *Korean J Chem Eng* [Internet] 2009; 26:153–5. Available from: <http://link.springer.com/10.1007/s11814-009-0024-y>

102. Besenhard MO, Baber R, LaGrow AP, Mazzei L, Thanh NTK, Gavriilidis A. New insight into the effect of mass transfer on the synthesis of silver and gold nanoparticles. *CrystEngComm* [Internet] 2018; 20:7082–93. Available from: <http://xlink.rsc.org/?DOI=C8CE01014E>
103. Zielińska A, Skwarek E, Zaleska A, Gazda M, Hupka J. Preparation of silver nanoparticles with controlled particle size. *Procedia Chem* [Internet] 2009; 1:1560–6. Available from: <https://linkinghub.elsevier.com/retrieve/pii/S1876619609003933>
104. Bhattacharjee S. Controlled Release. 2016.
105. T. L. Bergman ASL and FPI. Fundamentals of Heat and Mass Transfer. 2011.
106. Bayazit MK, Yue J, Cao E, Gavriilidis A, Tang J. Controllable Synthesis of Gold Nanoparticles in Aqueous Solution by Microwave Assisted Flow Chemistry. *ACS Sustain Chem Eng* 2016; 4:6435–42.
107. Murdock RC, Braydich-Stolle L, Schrand AM, Schlager JJ, Hussain SM. Characterization of Nanomaterial Dispersion in Solution Prior to In Vitro Exposure Using Dynamic Light Scattering Technique. *Toxicol Sci* [Internet] 2008; 101:239–53. Available from: <https://academic.oup.com/toxsci/article-lookup/doi/10.1093/toxsci/kfm240>
108. Bhattacharjee S. DLS and zeta potential – What they are and what they are not? *J Control Release* [Internet] 2016; 235:337–51. Available from: <https://linkinghub.elsevier.com/retrieve/pii/S0168365916303832>
109. Horikoshi S, Sumi T, Serpone N. A hybrid microreactor/microwave high-pressure flow system of a novel concept design and its application to the synthesis of silver nanoparticles. *Chem Eng Process Process Intensif* [Internet] 2013; 73:59–66. Available from: <https://linkinghub.elsevier.com/retrieve/pii/S0255270113001839>
110. Manno R, Sebastian V, Mallada R, Santamaria J. 110th Anniversary: Nucleation of Ag Nanoparticles in Helical Microfluidic Reactor. Comparison between Microwave and Conventional Heating. *Ind Eng Chem Res* [Internet] 2019; 58:12702–11. Available from: <https://pubs.acs.org/doi/10.1021/acs.iecr.9b01460>
111. Madkour M, Bumajdad A, Al-Sagheer F. To what extent do polymeric stabilizers affect nanoparticles characteristics? *Adv Colloid Interface Sci* [Internet] 2019; 270:38–

53. Available from: <https://linkinghub.elsevier.com/retrieve/pii/S0001868619300302>
112. Shimmin RG, Schoch AB, Braun P V. Polymer Size and Concentration Effects on the Size of Gold Nanoparticles Capped by Polymeric Thiols. *Langmuir* [Internet] 2004; 20:5613–20. Available from: <https://pubs.acs.org/doi/10.1021/la036365p>
113. Torabfam M, Jafarizadeh-Malmiri H. Microwave-enhanced silver nanoparticle synthesis using chitosan biopolymer: optimization of the process conditions and evaluation of their characteristics. *Green Process Synth* [Internet] 2018; 7:530–7. Available from: <https://www.degruyter.com/document/doi/10.1515/gps-2017-0139/html>
114. Wang M, Li H, Li Y, Mo F, Li Z, Chai R, Wang H. Dispersibility and Size Control of Silver Nanoparticles with Anti-Algal Potential Based on Coupling Effects of Polyvinylpyrrolidone and Sodium Tripolyphosphate. *Nanomaterials* [Internet] 2020; 10:1042. Available from: <https://www.mdpi.com/2079-4991/10/6/1042>
115. Farias-Aguilar JC, Ramírez-Moreno MJ, Téllez-Jurado L, Balmori-Ramírez H. Low pressure and low temperature synthesis of polyamide-6 (PA6) using Na O as catalyst. *Mater Lett* [Internet] 2014; 136:388–92. Available from: <https://linkinghub.elsevier.com/retrieve/pii/S0167577X14015390>
116. Xu Q, Li X, Chen F, Zhang Z. Improving the Mechanical Properties of Polyamide 6-Nanosilica Nanocomposites by Combining Masterbatch Technique with in situ Polymerization. *J Braz Chem Soc* [Internet] 2014; Available from: <http://www.gnresearch.org/doi/10.5935/0103-5053.20140099>
117. Hsueh Y-H, Lin K-S, Ke W-J, Hsieh C-T, Chiang C-L, Tzou D-Y, Liu S-T. The Antimicrobial Properties of Silver Nanoparticles in *Bacillus subtilis* Are Mediated by Released Ag+ Ions. *PLoS One* [Internet] 2015; 10:e0144306. Available from: <https://dx.plos.org/10.1371/journal.pone.0144306>
118. Anandalakshmi K, Venugopal J, Ramasamy V. Characterization of silver nanoparticles by green synthesis method using Pedalium murex leaf extract and their antibacterial activity. *Appl Nanosci* [Internet] 2016; 6:399–408. Available from: <http://link.springer.com/10.1007/s13204-015-0449-z>
119. Wani IA, Ganguly A, Ahmed J, Ahmad T. Silver nanoparticles: Ultrasonic wave assisted synthesis, optical characterization and surface area studies. *Mater Lett*

- [Internet] 2011; 65:520–2. Available from:  
<https://linkinghub.elsevier.com/retrieve/pii/S0167577X1000964X>
120. Porubská M, Szöllős O, Kóňová A, Janigová I, Jašková M, Jomová K, Chodák I. FTIR spectroscopy study of polyamide-6 irradiated by electron and proton beams. *Polym Degrad Stab* [Internet] 2012; 97:523–31. Available from:  
<https://linkinghub.elsevier.com/retrieve/pii/S0141391012000365>
121. Osonga FJ, Akgul A, Yazgan I, Akgul A, Eshun GB, Sakhaei L, Sadik OA. Size and Shape-Dependent Antimicrobial Activities of Silver and Gold Nanoparticles: A Model Study as Potential Fungicides. *Molecules* [Internet] 2020; 25:2682. Available from:  
<https://www.mdpi.com/1420-3049/25/11/2682>
122. Lin Z, Yunyun L, Bin C, Yu C. Synthesis of antibacterial polyurethane film and its properties. *Polish J Chem Technol* [Internet] 2020; 22:50–5. Available from:  
<https://www.sciendo.com/article/10.2478/pjct-2020-0016>
123. Li W-R, Xie X-B, Shi Q-S, Zeng H-Y, OU-Yang Y-S, Chen Y-B. Antibacterial activity and mechanism of silver nanoparticles on *Escherichia coli*. *Appl Microbiol Biotechnol* [Internet] 2010; 85:1115–22. Available from:  
<http://link.springer.com/10.1007/s00253-009-2159-5>
124. Radheshkumar C, Münstedt H. Antimicrobial polymers from polypropylene/silver composites—Ag<sup>+</sup> release measured by anode stripping voltammetry. *React Funct Polym* [Internet] 2006; 66:780–8. Available from:  
<https://linkinghub.elsevier.com/retrieve/pii/S1381514805002865>
125. Jo Y, Garcia C V., Ko S, Lee W, Shin GH, Choi JC, Park S-J, Kim JT. Characterization and antibacterial properties of nanosilver-applied polyethylene and polypropylene composite films for food packaging applications. *Food Biosci* [Internet] 2018; 23:83–90. Available from:  
<https://linkinghub.elsevier.com/retrieve/pii/S2212429217304200>
126. Jokar M, Abdul Rahman R, Ibrahim NA, Abdullah LC, Tan CP. Melt Production and Antimicrobial Efficiency of Low-Density Polyethylene (LDPE)-Silver Nanocomposite Film. *Food Bioprocess Technol* [Internet] 2012; 5:719–28. Available from:  
<http://link.springer.com/10.1007/s11947-010-0329-1>
127. Salavati-Niasari M. Polymeric Nanocomposite Materials. *Adv Divers Ind Appl*

Nanocomposites [Internet] 2011; :Ch. 22. Available from:  
<https://doi.org/10.5772/15657>

128. THOSTENSON E, LI C, CHOU T. Nanocomposites in context. Compos Sci Technol [Internet] 2005; 65:491–516. Available from:  
<https://linkinghub.elsevier.com/retrieve/pii/S0266353804003008>
129. Selvin TP, Ranimol S, Bandyopadhyay S ST. Polymer nanocomposites: Preparation properties and applications. Int Conf Polym Mater Halle/Saale 2007; :49–56.
130. Bondeson D. Biopolymer-based nanocomposites: Processing and properties. Trondheim: Norwegian University of Science and Technology; 2007.
131. Kamal T, Ul-Islam M, Khan SB, Asiri AM. Adsorption and photocatalyst assisted dye removal and bactericidal performance of ZnO/chitosan coating layer. Int J Biol Macromol [Internet] 2015; 81:584–90. Available from:  
<https://linkinghub.elsevier.com/retrieve/pii/S0141813015006078>
132. Khan SB, Lee J-W, Marwani HM, Akhtar K, Asiri AM, Seo J, Khan AAP, Han H. Polybenzimidazole hybrid membranes as a selective adsorbent of mercury. Compos Part B Eng [Internet] 2014; 56:392–6. Available from:  
<https://linkinghub.elsevier.com/retrieve/pii/S1359836813004642>
133. Kim D, Jang M, Seo J, Nam K-H, Han H, Khan SB. UV-cured poly(urethane acrylate) composite films containing surface-modified tetrapod ZnO whiskers. Compos Sci Technol [Internet] 2013; 75:84–92. Available from:  
<https://linkinghub.elsevier.com/retrieve/pii/S0266353812004149>
134. Lee Y, Kim D, Seo J, Han H, Khan SB. Preparation and characterization of poly(propylene carbonate)/exfoliated graphite nanocomposite films with improved thermal stability, mechanical properties and barrier properties. Polym Int [Internet] 2013; 62:1386–94. Available from:  
<https://onlinelibrary.wiley.com/doi/10.1002/pi.4434>
135. Ciprari D, Jacob K, Tannenbaum R. Characterization of Polymer Nanocomposite Interphase and Its Impact on Mechanical Properties. Macromolecules [Internet] 2006; 39:6565–73. Available from: <https://pubs.acs.org/doi/10.1021/ma0602270>
136. Hussain F, Hojjati M, Okamoto M, Gorga RE. Review article: Polymer-matrix

nanocomposites, processing, manufacturing, and application: An overview. *J Compos Mater* 2006; 40:1511–75.

137. Mayer ABR. Polymer Nanocomposites with Metal Dispersions [Internet]. In: Encyclopedia of Materials: Science and Technology. Elsevier; 2001. page 7449–55. Available from: <https://linkinghub.elsevier.com/retrieve/pii/B0080431526013309>
138. N. Bifari E, Bahadar Khan S, A. Alamry K, M. Asiri A, Akhtar K. Cellulose Acetate Based Nanocomposites for Biomedical Applications: A Review. *Curr Pharm Des* 2016; 22:3007–19.
139. Gholami A, Moghadassi AR, Hosseini SM, Shabani S, Gholami F. Preparation and characterization of polyvinyl chloride based nanocomposite nanofiltration-membrane modified by iron oxide nanoparticles for lead removal from water. *J Ind Eng Chem* [Internet] 2014; 20:1517–22. Available from: <https://linkinghub.elsevier.com/retrieve/pii/S1226086X13003523>
140. Hendrick E, Frey M, Herz E, Wiesner U. Cellulose acetate fibers with fluorescing nanoparticles for anti-counterfeiting and pH-sensing applications. *J Eng Fiber Fabr* 2010; 5:21–30.
141. Cortina H, Martínez-Alonso C, Castillo-Ortega M, Hu H. Cellulose acetate fibers covered by CdS nanoparticles for hybrid solar cell applications. *Mater Sci Eng B* [Internet] 2012; 177:1491–6. Available from: <https://linkinghub.elsevier.com/retrieve/pii/S0921510712000967>
142. Ghiyasiyan-Arani M, Masjedi-Arani M, Ghanbari D, Bagheri S, Salavati-Niasari M. Novel chemical synthesis and characterization of copper pyrovanadate nanoparticles and its influence on the flame retardancy of polymeric nanocomposites. *Sci Rep* 2016; 6:1–9.
143. Wojciechowska P, Foltynowicz Z, Nowicki M. Cellulose acetate butyrate nanocomposites synthesized via sol-gel method. *Polimery/Polymers* 2013; 58:543–9.
144. Khan FU, Asimullah, Khan SB, Kamal T, Asiri AM, Khan IU, Akhtar K. Novel combination of zero-valent Cu and Ag nanoparticles @ cellulose acetate nanocomposite for the reduction of 4-nitro phenol. *Int J Biol Macromol* [Internet] 2017; 102:868–77. Available from: <https://linkinghub.elsevier.com/retrieve/pii/S0141813016329415>

145. Chani MTS, Karimov KS, Khan SB, Asiri AM. Fabrication and investigation of cellulose acetate-copper oxide nano-composite based humidity sensors. *Sensors Actuators, A Phys* [Internet] 2016; 246:58–65. Available from: <http://dx.doi.org/10.1016/j.sna.2016.05.016>
146. Sadanand V, Rajini N, Satyanarayana B, Rajulu AV. Preparation and properties of cellulose/silver nanoparticle composites with in situ -generated silver nanoparticles using Ocimum sanctum leaf extract. *Int J Polym Anal Charact* [Internet] 2016; 21:408–16. Available from: <http://www.tandfonline.com/doi/full/10.1080/1023666X.2016.1161100>
147. Muthulakshmi L, Varada Rajalu A, Kaliaraj GS, Siengchin S, Parameswaranpillai J, Saraswathi R. Preparation of cellulose/copper nanoparticles bionanocomposite films using a bioflocculant polymer as reducing agent for antibacterial and anticorrosion applications. *Compos Part B Eng* [Internet] 2019; 175:107177. Available from: <https://doi.org/10.1016/j.compositesb.2019.107177>
148. Sukumar S, Rudrasenan A, Padmanabhan Nambiar D. Green-Synthesized Rice-Shaped Copper Oxide Nanoparticles Using Caesalpinia bonduculla Seed Extract and Their Applications. *ACS Omega* [Internet] 2020; 5:1040–51. Available from: <https://pubs.acs.org/doi/10.1021/acsomega.9b02857>
149. El-Saadony MT, Abd El-Hack ME, Taha AE, Fouda MMG, Ajarem JS, N. Maodaa S, Allam AA, Elshaer N. Ecofriendly Synthesis and Insecticidal Application of Copper Nanoparticles against the Storage Pest *Tribolium castaneum*. *Nanomaterials* [Internet] 2020; 10:587. Available from: <https://www.mdpi.com/2079-4991/10/3/587>
150. Prakash J, Venkataprasanna KS, Bharath G, Banat F, Nirajan R, Venkatasubbu GD. In-vitro evaluation of electrospun cellulose acetate nanofiber containing Graphene oxide/TiO<sub>2</sub>/Curcumin for wound healing application. *Colloids Surfaces A Physicochem Eng Asp* [Internet] 2021; 627:127166. Available from: <https://linkinghub.elsevier.com/retrieve/pii/S0927775721010359>
151. Suresh S, Karthikeyan S, Jayamoorthy K. FTIR and multivariate analysis to study the effect of bulk and nano copper oxide on peanut plant leaves. *J Sci Adv Mater Devices* [Internet] 2016; 1:343–50. Available from: <https://linkinghub.elsevier.com/retrieve/pii/S2468217916301125>

152. Raja M, Subha J, Ali FB, Ryu SH. Synthesis of Copper Nanoparticles by Electroreduction Process. *Mater Manuf Process* [Internet] 2008; 23:782–5. Available from: <http://www.tandfonline.com/doi/abs/10.1080/10426910802382080>
153. Lambert JB, Shurvell HF, Cooks RG. *Introduction to Organic Spectroscopy*. Macmillan Publishing Company; 1987.
154. Selvakumar M, Bhat DK. LiClO<sub>4</sub> doped cellulose acetate as biodegradable polymer electrolyte for supercapacitors. *J Appl Polym Sci* [Internet] 2008; 110:594–602. Available from: <https://onlinelibrary.wiley.com/doi/10.1002/app.28671>
155. Sudiarti T, Wahyuningrum D, Bundjali B, Made Arcana I. Mechanical strength and ionic conductivity of polymer electrolyte membranes prepared from cellulose acetate-lithium perchlorate. *IOP Conf Ser Mater Sci Eng* [Internet] 2017; 223:012052. Available from: <https://iopscience.iop.org/article/10.1088/1757-899X/223/1/012052>